MODELING THE HYDRODYNAMICS IN TIDAL NETWORKS

Omslag: Bewerking van Landsat foto's van de Yangtze delta, China (voorzijde) en de Ems rivier, Nederland (achterzijde, *USGS, http://landsat.usgs.gov*)

PhD thesis, Utrecht University, the Netherlands (2015).
Printed by Ridderprint BV
ISBN: 978-94-6299-259-7

Modeling the hydrodynamics in tidal networks

Modelleren van de hydrodynamica in getijde netwerken
(met een samenvatting in het Nederlands)

Proefschrift

ter verkrijging van de graad van doctor aan de Universiteit Utrecht op gezag van de rector magnificus, prof.dr. G.J. van der Zwaan, ingevolge het besluit van het college voor promoties in het openbaar te verdedigen op maandag 25 januari 2016 des middags te 2.30 uur

door

Niels Christiaan Alebregtse

geboren op 15 mei 1988 te Delfzijl

Promotor: Prof.dr. H.E. de Swart

Dit proefschrift werd mogelijk gemaakt met financiële steun van de Nederlandse Organisatie voor Wetenschappelijk Onderzoek (NWO) en de Chinese Organisatie voor Wetenschappelijk Onderzoek (NSFC).

Contents

Chapter 1

Introduction

This thesis discusses the hydrodynamics in coastal areas consisting of semi-enclosed bodies of water, that contain multiple channels. Such bodies of water are commonly present at river mouths, such as the Rhine-Meuse delta, and the Yangtze estuary. They fulfill many economical functions (e.g. transportation of goods and people, fishery and provision of fresh water), as well as ecological functions (e.g. providing breeding and feeding grounds for fish and birds). The fulfillment of these functions varies due to changes in the hydrodynamical and morphological conditions. Such changes are partly due to inherent (short-term) variability, and partly related to human interventions, sea level rise, seasonal variability, etc. There is a strong need from society to maintain both the economical and ecological functions of an estuary, which often have conflicting criteria. As a result, understanding and quantifying the effects of hydrodynamical and morphological changes on these functions and how potential complications can be mitigated are important goals for the scientific community. In this thesis, the aim is to gain insight in how the changing conditions influence the dominant hydrodynamical processes in bodies of water that contain multiple channels.
First, descriptions of the study areas are given. Second, commonly observed negative changes in these coastal areas will be outlined, giving a motivation for the study. Third, an overview is provided of the important processes that occur in the study areas. Fourth, gaps in the present knowledge will be converted into objectives of this thesis. Fifth, the research approach will be discussed briefly. Finally, the thesis will be outlined further and the contents of the different chapters will be presented.

1.1 Study areas

Along many coastlines in the world, rivers discharge fresh water into the ocean. Semi-enclosed bodies of water in which fresh water meets the salt water coming

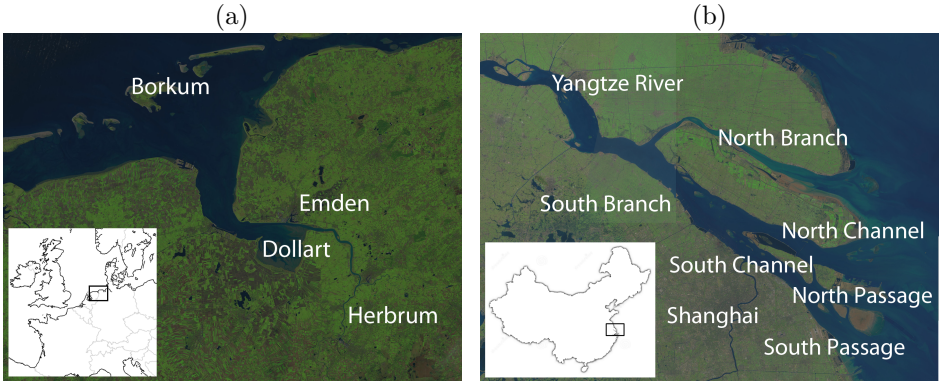

Figure 1.1: Panel a: Landsat images of the Ems estuary. The inset shows the location of the estuary in Europe. Panel b: Landsat images of the Yangtze estuary. The inset shows the location of the estuary in China (*USGS, http://landsat.usgs.gov*).

in with the tide are called estuaries (Pritchard, 1967). Estuaries are confined by the open boundary with the ocean and the so-called tidal limit, the point at which the effects of the tide are extinguished. Estuaries appear in many different forms, with large variations in length, depth, and width, as well as different hydrodynamical conditions, such as different tidal range and river discharge (cf. Dyer, 1986; Valle-Levinson, 2010). The balance between the tidal mixing and the river flow determines the level of salinity stratification in an estuary. If the mixing of the tides prevails, the water column becomes well mixed, while stronger river flow can lead to partially mixed or even stratified conditions (Guha & Lawrence, 2013; Geyer & MacCready, 2014). Additionally, estuaries often exhibit intertidal areas, which are surfaces that are only submerged during part of the tidal cycle. The extent of these areas vastly differs per estuary (cf. Dronkers, 1986). Moreover, the amount of channels comprising an estuary varies between estuaries. In this thesis, the focus will be on the Ems estuary at the Dutch–German border and the Yangtze estuary near Shanghai China. Landsat images of these estuaries are presented in Fig. 1.1(a) and (b), respectively (*USGS, http://landsat.usgs.gov*). These estuaries are widely different in geometry and hydrodynamic conditions, yet face similar (and typical) estuarine challenges. They will be introduced in the next two subsections.

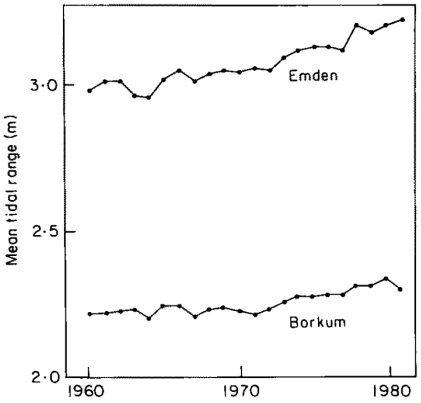

Figure 1.2: Tidal range at two locations in the Ems estuary as a function of time. Borkum is located at the seaward boundary of the estuary, while Emden is located near the Dollart basin halfway along the estuary. Figure from de Jonge (1992).

1.1.1 Ems estuary

Characteristics

The Ems estuary has an approximate length of 100 km from the barrier islands at the North Sea to the weir at Herbrum, which is the tidal limit (see Fig. 1.1a). The estuary has large intertidal areas near the barrier islands up to the Dollart basin, the latter is separated from the main fairway by the Geise-Leit dam. Channel depth varies between 10 and 20 m up to the Dollart basin. Further upstream the amount of tidal flats is reduced by channelization of the fairway and the depth is maintained at approximately 8 m for shipping purposes (Talke *et al.*, 2009*b*). The width of the estuary decreases from about 8 km at the North Sea boundary to about 100 m at the weir. Tides coming from the North Sea are predominantly semi-diurnal with a typical tidal range around 2.3 m at Borkum (Schuttelaars *et al.*, 2013). Finally, the yearly averaged freshwater discharge is approximately 100 m^3s^{-1}, with annual variations of 50 m^3s^{-1}. The Ems estuary is classified as a well-mixed estuary (de Jonge, 1992; Talke *et al.*, 2009*a*).

Recent developments & problems

Over the past decades, the main fairway of the Ems estuary has been deepened several times to maintain access to various harbors along the estuary (de Jonge *et al.*, 2014). This led to an increase in tidal range over time, which is shown in Fig. 1.2. Increased tidal range and tidal currents enhance the risk of flooding and dike breaching, which poses serious socio-economic risks. Moreover, increased

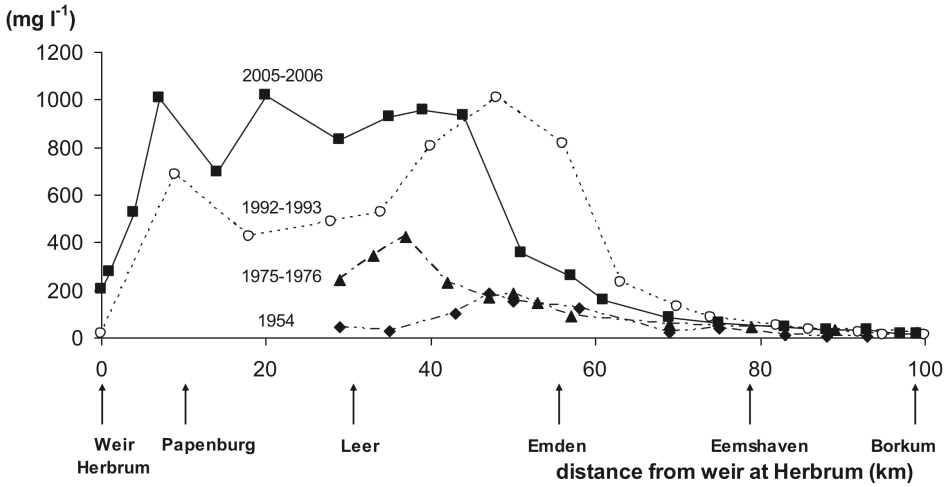

Figure 1.3: Suspended particulate matter (SPM) in the Ems estuary as a function of position in the estuary for different years. Here, the river is at the left and the sea at the right. Figure from de Jonge *et al.* (2014).

tidal range results in lower low water levels reducing navigability during part of the tidal cycle. Additionally, peak sediment concentrations have increased and also extend further landward (Fig. 1.3), leading to anoxic conditions and straining ecology (de Jonge, 2000; Talke *et al.*, 2009*a*). Above a threshold concentration, sediment flocs together to form fluid mud, which causes an additional amplification of the tide due to decreased frictional damping (Winterwerp & Wang, 2013).

1.1.2 Yangtze estuary

Characteristics

The Yangtze estuary has a length of about 600 km, measured from its seaward outlets to the tidal limit. Beyond the tidal limit, the Yangtze river continues. The estuary features three large-scale channel bifurcations, resulting in a system of seven channels of which four are connected to the sea (see Fig. 1.1b). The different channels from North to South are the Yangtze River, North Branch, South Branch, North Channel, South Channel, North Passage and South Passage. Intertidal areas are found throughout the estuary, with extensive tidal flats near the mouth of the outlets. The depth of all the channels is about 10 m, except in the North Branch, where the depth is around 5 m (Zhang *et al.*, 2012). The combined width of the outlets at the ocean is approximately 80 km. The total width decreases upstream to about 2 km near the tidal limit. Tides from the

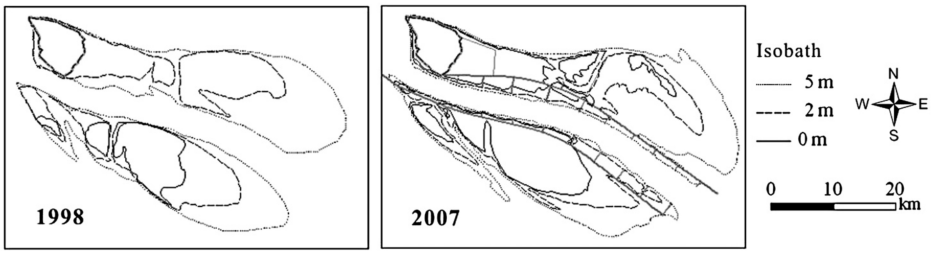

Figure 1.4: Bathymetric maps of the North Passage (the second outlet from the South in the Yangtze Estuary) from 1998 and 2007. In 2007, the engineering works are visible as solid lines with groins and jetties extending into the fairway. The Hengsha shoal lies north of North Passage. Figure after Jiang *et al.* (2012).

East China Sea have a semi-diurnal to diurnal character with an average semi-diurnal and diunal tidal range at the seaward boundary of about 2.7 m and 1.2 m, respectively (He *et al.*, 2001; Guo *et al.*, 2015). Finally, freshwater discharge in the Yangtze estuary has an annual average value of 28.300 m^3s^{-1}, which reaches peak values of 40.000 m^3s^{-1} in wet season and minima of 10.000 m^3s^{-1} in dry season (Chen *et al.*, 2001; Jiang *et al.*, 2012). On average the Yangtze estuary is classified as a partially mixed estuary. However, due to strong variability in river discharge it ranges from stratified to well-mixed.

Recent developments & problems

The presence of the city and harbor of Shanghai has necessitated many alterations to the Yangtze estuary. Land reclamations are widespread throughout the estuary, with notable projects in the North Branch and on the Hengsha shoal (see Fig. 1.4). Between 1998 and 2010, engineering works were carried out in the North Passage. The engineering works consisted of a deepening of the main fairway to 12 m depth and the construction of two training walls with groins and jetties up to the mean high water line to provide a navigation channel for ships (see Fig. 1.4). As a result, local tidal velocities increased, which subsequently increased the turbidity and caused many bathymetric changes (e.g. strong siltation in the navigation channel, see Yang *et al.*, 2006, and Jiang *et al.*, 2012, 2013). Furthermore, the ebb water diversion ratio between North and South Passage (i.e. the ratio of ebb directed water transport in North Passage to the combined ebb transport in North and South Passage) decreased, as indicated in Fig. 1.5 (Gao *et al.*, 2009).
Additionally, the Qingcaosha Reservoir was constructed in the North Channel aiming to provide 50% of the freshwater demand from Shanghai (Li *et al.*, 2014). Its functioning is at stake during events when salinity intrudes through the North

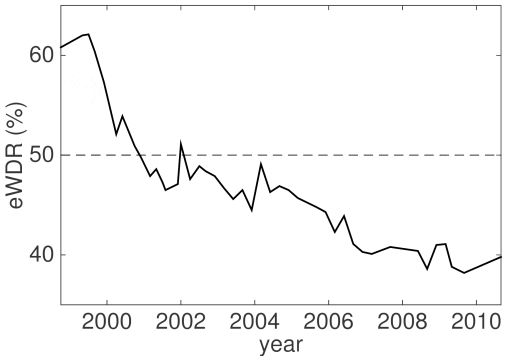

Figure 1.5: Ratio of the ebb directed water transport in the North Passage to the sum of the transports in the North and South Passage combined as a function of time. Figure after Gao *et al.* (2009) and Jiang *et al.* (2013).

Branch into the South Branch, as well as during lateral salt intrusion in the North Channel (Li *et al.*, 2012, 2014).

1.2 Motivation

The recent developments and problems in the Ems and Yangtze as described in the previous sections, are not unique to these estuaries. Increasing tidal range is widely observed in estuaries (e.g. Flick *et al.*, 2003; Winterwerp *et al.*, 2013; Vellinga *et al.*, 2014). Furthermore, changes in the net (i.e. tidally averaged) water transport through different channels in a tidal network, as exemplified by the Yangtze estuary, also occur in other estuarine networks (as discussed by Buschman *et al.*, 2009, and Sassi *et al.*, 2011). This has implications for salinity intrusion and contaminant flushing, which are in turn important for fresh water supply and the health of the ecosystem.

To understand, quantify, and mitigate the observed changes in the hydrodynamics of estuaries as described above, a fundamental analysis of the water motion in these environments is needed. Thus, it is important to investigate the processes that influence tidal range, viz. tidal amplification, friction, and tidal distortion, as this allows to address problems of navigability, flood risk and related problems. Moreover, studying subtidal motion and the interaction between the river and the tide is important to assess flushing of pollutants and fresh water supply. Therefore, the current state of knowledge on these topics will be discussed and gaps in the knowledge will be identified. These will then be used to set the specific aims of this thesis.

1.3 Present knowledge

1.3.1 Tidal motion

Tidal motion originates predominantly from the open ocean, where it is generated by the moon and sun through tidal forces (gravity and centripetal force, Platzman, 1971). The tidal motion in estuaries occurs mainly due to forcing by co-oscillation. Inside the estuary, the tidal signal is deformed from the open ocean signal. This deformation encompasses amplification of the tide, damping by turbulent energy dissipation, and distortion of the tidal signal (Parker, 1991).
Tidal amplification in estuaries has two causes. The first is convergence of the channel cross-section (Friedrichs & Aubrey, 1994; Lanzoni & Seminara, 1998; Toffolon *et al.*, 2006). The second, tidal resonance, results from reflection of the tidal wave at the head of the estuary (Friedrichs, 2010). Tidal resonance is influenced by the length of the estuary, the local water depth, the extent of the intertidal area, the roughness of the bed, and the amount of cross-sectional convergence.
Damping acts to reduce the tidal amplitude as a result of turbulent dissipation of energy. One of the main sources of turbulence is the shear stress at the bed (Burchard, 2002). Generally, the bed shear stress is parameterized using a quadratic expression in the velocity of the currents (Young, 1813; Ferrel, 1874).
Distortion of the tidal signal result from non-linear interactions between tidal components (Parker, 1991). These interactions result in tidal components, which have frequencies equal to the sum and difference of the interacting components. Examples of non-linear interactions are the divergence of Stokes transport, the quadratic bed shear stress and advection of momentum (see Parker, 1991, for a description of these processes). In estuaries that are short compared to the tidal wavelength, these interactions are responsible for creating flood dominant currents, i.e. tidal velocity profiles with higher landward velocities than seaward velocities (Speer & Aubrey, 1985). The presence of intertidal areas leads to additional tidal deformation (Boon & Byrne, 1981; Speer & Aubrey, 1985; Friedrichs & Aubrey, 1994). For estuaries that are short compared to the tidal wavelength, the intertidal areas favor ebb dominant currents (Speer & Aubrey, 1985), while for long estuaries intertidal areas increase the flood dominance (Ridderinkhof *et al.*, 2014). However, studies on tidal flats only consider the effect of the storage of mass on the tidal flats, while Dronkers (1964) and Speer (1984) showed that water flooding the tidal flats carries along-channel momentum, which is quickly lost there. This momentum sink has not been studied in detail. Additionally, all previous work only considered linearly sloping flats, while equilibrium tidal flat profiles in nature range from concave to convex (Friedrichs & Aubrey, 1996; Friedrichs, 2011).

1.3.2 River discharge

River discharge results from terrestrial runoff. This runoff generally has a seasonal cycle, among others caused by changes in precipitation and melt water supply. However, changes during a tidal cycle are mostly small compared to the tidal velocity and river discharge is therefore often considered constant over a tidal cycle. River-tide interactions occur through the same interactions as those that cause the tidal distortion. River discharge influences the tidal wave propagation by causing additional drag (Godin, 1991, 1999; Buschman *et al.*, 2009; Cai *et al.*, 2014), while it was also observed that higher discharge results in increased tidal distortion (Guo *et al.*, 2015).
The additional drag results from the quadratic bottom stress formulation. However, describing the river-tide interaction through the quadratic bottom stress explicitly is difficult. Many attempts have been made to linearize this formulation. A notable success is the linearization procedure of Lorentz (1922), which is based on equal energy dissipation between the linearized and quadratic expression. The disadvantage of his approach was that the tidal distortion caused by friction was not obtained. Zimmerman (1982, 1992) revisited the linearization procedure of Lorentz (1922), by considering the energy dissipation argument as a renormalization procedure. Using this technique, he obtained an expression for the tidal distortion of a single tidal component. However, this approach did not account for the interaction between different tidal components or for river-tide interactions. Dronkers (1964) applied two other techniques for the linearization, viz. a Fourier decomposition and a Chebyshev expansion. The latter has been revisited by Godin (1991, 1999), who greatly simplified the expression. These approaches revealed how the interaction of different harmonic components result in tidal distortion. However, the expressions from Dronkers (1964) and Godin (1999) have been mostly applied to subtidal motion, i.e. water motion on a timescale longer than a tidal period, instead of on intertidal motion.

1.3.3 Tidal networks

Tidal propagation in a network of channels is a long subject of research, which was first touched upon by Lorentz (1926). More recently, Hill & Souza (2006) revisited this topic. However, they worked under the assumption of linear tides, without any tidal distortion accounted for. Additionally, neither of these studies considers river discharge. Knowledge on tidal propagation in tidal networks can be applied to reduce tidal range, as was suggested by Donner *et al.* (2012). They suggested to construct secondary channels alongside the main channel of an estuary, but did not investigate through which mechanism these secondary channels influence the tidal range.
Of additional interest in tidal networks is the river induced transport in different

channels of the network. When a tidal network experiences a significant influence from fresh water discharge, it is referred to as an estuarine network. Many researchers have investigated how the river discharge splits at fluvial bifurcations (e.g. Bolla-Pittaluga *et al.*, 2003; Kleinhans *et al.*, 2008). However, the field of net water transport division in tidally influenced environments is a relatively young one. Pioneering work was performed by Buschman *et al.* (2010), who performed a study on net water transport division at an idealized bifurcation point under influence of tides. They found that tidal processes enhance net water transport in the channel with the highest river discharge, and consequently reduce it in the other channel. Sassi *et al.* (2011) applied this theory to a real estuarine network (the Mahakam delta, Indonesia) and found that tides can also reduce the asymmetry in river discharge division, through a process called differential water set-up.
The work of Buschman *et al.* (2010) and Sassi *et al.* (2011) highlighted the importance of tides in determining the net water transport division in estuarine networks. However, they both applied a numerical model to their systems, and did not identify which non-linear interactions (both between tidal components and between the river and the tide) are responsible for the observed patterns of net water division.
Finally, in many tidal networks tidal flats act as a barrier between two channels during part of the tidal cycle. Moreover, human structures, such as the Geise-Leit Dam in the Ems estuary and the training walls in the North Passage of the Yangtze estuary, alter the character of this interaction. However, fundamental studies investigating the effect of the exchange of water over the tidal flats on the tidal flow and tidal distortion are lacking. Hamilton (1990) used a formulation for overtopping in a numerical model applied to the Columbia river. He suggested that overtopping allows the transport of water through one channel at the expense of another. However, he did not present model results where the overtopping was omitted to confirm this claim.

1.4 Research questions

In the previous sections, several remaining challenges have been identified from the literature. These are:

1. Despite the broad knowledge on how tidal range has increased in many estuaries, the challenge remains to find measures that reduce tidal range. One possible solution is the construction of secondary channels alongside estuaries as was suggested by Donner *et al.* (2012). However, the exact nature and extent of their effect is unknown.

2. Many studies on river-tide interactions have focused on subtidal motion and the division of net water transport at bifuractions. It has not been estab-

lished which mechanisms are the most important in influencing this division. Moreover, it remains unknown through which mechanisms the river-tide interactions affect intertidal motion.

3. Early studies on tidal flats identified two mechanisms for tidal distortion related to intertidal areas. Only the mass storage on tidal flats has been studied in depth since, while the sink of momentum has been neglected. Additionally, the effect of the exchange of mass and momentum through overtopping between two channels that are separated by a tidal flat on the tidal distortion has not been investigated to date.

These observations have led to the following research questions

1. Through which mechanism do secondary channels dampen or amplify the tide in a main channel? And how does the damping or amplification quantitatively depend on the characteristics (position, geometry, etc.) of the secondary channel in the main channel?

2. What impact does a secondary channel have on the non-linear characteristics of the tide in the main channel, viz. the tidal range, the duration between high water and low water, the flood-to-ebb ratio and the duration between peak flood and peak ebb currents? How will the changes in tidal currents affect the net transport of coarse and fine sediment?

3. How do river-tide interactions and residual tidal currents quantitatively affect tides, as well as the net water transport in an estuarine network? What changes occur in the tides and in the net water transport for different amounts of river discharge and/or different geometrical configurations?

4. What influence does the dissipation of momentum on tidal flats have on the non-linear characteristics of the tidal velocity (as specified in question 2) in the channel? Similarly, what is the effect of the exchange of mass and momentum through overtopping between two channels that are separated by a tidal flat on non-linear tidal velocity in the channels? What are the implications for the net transport of coarse and fine sediment in these channels due to these processes?

1.5 Research approach

The aim of this thesis is to obtain fundamental insight about the effect of changing hydrodynamical and morphological conditions on estuarine hydrodynamics. Therefore idealized models will be utilized. The models are all cross-sectionally

averaged, as this captures most of the relevant processes that determine tidal deformation (i.e. amplification and damping) and net water transport. The governing equations are solved both (semi-)analytically, as well as numerically. Analytical models are used because the idealized nature of these models allows an in-depth investigation of the dominant estuarine processes through sensitivity analyses. Moreover, the effect of each non-linear interaction can be identified through a mathematical solution of the interactions under investigation. This allows the full response of the estuary to be explained as the sum of the different contributions. However, these models have to be developed with the use of some assumptions. Numerical models have the advantage of more accurately accounting for non-linear interactions, but make it more difficult to distinguish the contribution of the separate non-linear interactions. By combining the two approaches, the merits of both model types can complement each other.

1.6 Thesis outline

In this thesis, the research questions posed in section 1.4 are addressed. The first research question is addressed in chapter 2 using an analytical model, which describes the difference in linear tidal wave propagation between a semi-enclosed basin with a single channel and a semi-enclosed basin comprising a main channel and a secondary channel at an arbitrary position. The second research question is answered in chapter 3 with the use of a non-linear numerical model for the cross-sectionally averaged water motion. It is applied to the same geometry as used in chapter 2. Also, a comparison between the numerical and analytical model results is presented. The third research question is addressed in chapter 4. An analytical model is presented that identifies the river-tide interaction mechanisms and quantifies their importance with respect to each other. It is applied to the Yangtze estuary and its output is compared with a numerical model, as well as available data. The final research question is treated in chapter 5, where a numerical model is applied to investigate the changes in tidal velocities caused by the dissipation of momentum on the tidal flats and the exchange of mass and momentum through overtopping between channels connected by a tidal flat, as well as the non-linear velocity characteristics. The results of the numerical model for the momentum sink are explained with the use of an analytical solution for this mechanism, which is derived in that same chapter. In chapter 6, the main conclusions of the different chapters are summarized and suggestions for further research are provided.

Chapter 2

Resonance characteristics of tides in branching channels

2.1 Introduction

Tidal embayments and estuaries are often subject to human interventions. Knowledge of the influence of such interventions on tidal hydrodynamics is important for safety regulations and ecological values in these areas. Therefore, theoretical model studies have been performed to assess the response of tidal characteristics in an embayment, amongst others to changes in its length (Prandle & Rahman, 1980; Schuttelaars & de Swart, 2000; Rainey, 2009; Schuttelaars *et al.*, 2013), and depth (Chernetsky *et al.*, 2010).

Changes of tidal characteristics in embayments may also be induced by the presence of harbours or secondary channels along their sides. Construction of secondary channels is currently considered by coastal managers to reduce negative effects of previous interventions, such as increased tidal range (Donner *et al.*, 2012). So far, studies on harbours have mostly limited themselves to research on free modes (Defant, 1961), and resonance characteristics of the harbours (cf. Miles, 1971; de Jong & Battjes, 2004). How secondary channels influence the water motion in their surrounding areas is less well known. This phenomenon, related to radiation damping, has been investigated in coastal dynamics a.o. by Buchwald (1971); Garrett (1975); Zimmerman (1992) and Mei *et al.* (2005). These studies assumed that the forcing wave, which is present in the absence of a secondary channel, occurred in a semi-unbounded domain.

The problem introduced here has an analogy in acoustics, where uniform pipes

This chapter is based on:
Alebregtse, N. C., de Swart, H. E. & Schuttelaars, H. M. 2013 Resonance characteristics of tides in branching channels. *Journal of Fluid Mechanics* **728** (R3).

are considered with side branches, which can act as acoustic filters (cf. Lighthill, 1978; Kinsler *et al.*, 2000). There, the side branches are closed on one end, but both ends of the main pipe are open, thus preventing any reflection of the radiated waves.

The novel aspect of this work is that changes of tidal wave characteristics will be determined in a main channel, which is closed at one end, due to the presence of a secondary channel including friction. Specifically, the effect of secondary channel characteristics (location, length, depth, shape) on the amplification of incoming waves in the main channel will be assessed. Here, amplification is defined as the ratio of the sea surface height amplitude in the presence and absence of the secondary channel. To that end, section 2.2 will describe the model set-up. Results will be presented in section 2.3, which will be discussed in section 2.4. Finally, conclusions are presented in section 2.5.

2.2 Model and Methods

A model is considered that solves the hydrodynamics in a channel network. The network consists of a main channel with length l_b^*, and a secondary channel located at a distance x_{sc}^* from the open boundary. The main channel is split into two parts; channel 1 is located seaward of the secondary channel and channel 2 landward. The secondary channel is represented by channel 3. The width, depth and friction of the channels in the network are constant throughout the channel, but can vary among them (see figure 2.1).

The one-dimensional, linearised shallow water equations describe the water motion in the network. These are the along-channel momentum balance and the continuity equation,

$$\frac{\partial u_j^*}{\partial t^*} = -g^* \frac{\partial \eta_j^*}{\partial x_j^*} - \frac{\lambda_j^* u_j^*}{h_j^*} \ , \tag{2.1}$$

$$\frac{\partial \eta_j^*}{\partial t^*} = -h_j^* \frac{\partial u_j^*}{\partial x_j^*} \ . \tag{2.2}$$

Here, the symbol $\cdot^*$ indicates a dimensional quantity, j is the channel index, u_j^* (x_j^*) the velocity (coordinate) along the main axis of each channel, η_j^* the sea surface elevation, t^* the time, g^* the acceleration due to gravity, λ_j^* the dimensional linear friction coefficient, and h_j* the depth. Finally, w_j^* is the width of channel j, which will appear when applying mass continuity at the vertex point.

Six boundary conditions have to be prescribed to equations (2.1) and (2.2), two for each branch of the network. The general approach to obtain the condition at the open boundary $x^* = 0$ is to derive the Green's function for the outer domain $x^* < 0$ (cf. Garrett, 1975). Here, a simpler condition is imposed, which is done for

analytical tractability. This condition consists of a sea surface amplitude forcing by an incoming tidal wave with angular frequency $\sigma^* = 2\pi/T^*$, where T^* is the tidal period (typically, T^* is 12 hours and 25 minutes for the M_2 tide). It is assumed that the incoming wave remains unchanged under changing conditions in the network. The changes of the incoming wave, e.g. due to (partial) reflection of the outgoing wave outside the domain, are assumed negligible. The present approach differs from prescribing a fixed amplitude at the open boundary, which is observed in co-oscillating basins, in that the latter model keeps the sum of the incoming and reflected wave fixed. The landward boundaries of the main channel and of the secondary channel are closed. Finally, matching conditions connect the channels at the vertex point. These are continuity of sea surface elevation (twice) and conservation of mass.
Equations (2.1) and (2.2) are made dimensionless, by introducing

$$u_j^* = U^*\ u_j\ , \qquad x_j^* = l_b^*\ x_j\ , \qquad w_j^* = w_1^* w_j\ ,$$
$$\eta_j^* = N^*\ \eta_j\ , \qquad t^* = t/\sigma^*\ , \qquad h_j^* = h_1^* h_j\ .$$

Here, $U^* = N^* l_b^* \sigma^*/h_1^*$ is a typical velocity scale (following from continuity) and N^* is the amplitude of the incoming wave. Applying these scales to the dimensional equations results in

$$\frac{\partial u_j}{\partial t} = -\frac{1}{\mu^2}\frac{\partial \eta_j}{\partial x_j} - \frac{\lambda_j u_j}{h_j}\ , \tag{2.3}$$

$$\frac{\partial \eta_j}{\partial t} = -h_j \frac{\partial u_j}{\partial x_j}\ , \tag{2.4}$$

where $\mu = 2\pi l_b^*/l_t^*$ is, apart from a factor 2π, the ratio of the length of the main channel and the tidal wave length ($l_t^* = \sqrt{g^* h_1^*} T^*$) and $\lambda_j = \lambda_j^*/(h_1^* \sigma^*)$ the dimensionless linear friction coefficient.
Equations (2.3) and (2.4) can be combined into wave equations for the free surface in every channel. Their solutions are of the form

$$(\eta_j(x,t), u_j(x,t)) = (\hat{\eta}_j(x), \hat{u}_j(x)) e^{-\mathrm{i}t} + \text{c.c.},$$

where $\hat{\cdot}$ indicates a complex amplitude and c.c. denotes a complex conjugate. The resulting equations for the complex sea surface amplitudes $\hat{\eta}_j$ read

$$\frac{d^2\hat{\eta}_j}{dx_j^2} + \frac{\mu^2}{h_j}(1 + \mathrm{i}\frac{\lambda_j}{h_j})\ \hat{\eta}_j = 0\ , \tag{2.5}$$

which have solutions of the form

$$\hat{\eta}_j = A_{j,1} e^{\mathrm{i}\kappa_j x_j} + A_{j,2} e^{-\mathrm{i}\kappa_j x_j}\ , \qquad j = 1,2,3, \tag{2.6}$$

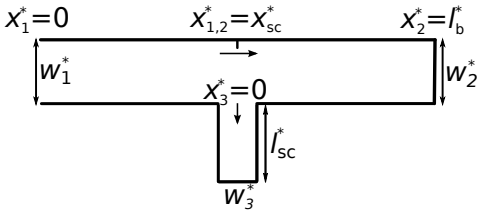

Figure 2.1: Model domain consisting of a main channel with length l_b^* and a secondary channel with length l_{sc}^* at distance x_{sc}^* from the open boundary. The open boundary is at $x_1^* = 0$, where an incoming wave is prescribed. The channel widths are w_j^* $(j = 1, 2, 3)$ and x_j^* is the along-axial coordinate

with $\kappa_j = (\mu/h_j)\sqrt{h_j + \mathrm{i}\lambda_j}$ the complex wave number. The first term on the right hand side denotes the spatial part of a wave propagating in the $+x$-direction (incoming), whereas the second term denotes the spatial part of a wave propagating in the $-x$-direction (outgoing).
The boundary conditions to equation (2.6) are mathematically given as

$$A_{1,1} = 1 \qquad \text{at } x_1 = 0\ , \tag{2.7}$$

$$\hat{u}_2 = 0 \qquad \text{at } x_2 = 1\ , \tag{2.8}$$

$$\hat{u}_3 = 0 \qquad \text{at } x_3 = \tilde{l}\ , \tag{2.9}$$

$$\hat{\eta}_1 = \hat{\eta}_2 \qquad \text{at } x_1 = x_2 = x_{sc}\ , \tag{2.10}$$

$$\hat{\eta}_1 = \hat{\eta}_3 \qquad \text{at } x_1 = x_{sc},\ x_3 = 0\ , \tag{2.11}$$

$$\hat{u}_1 = w_2 h_2 \hat{u}_2 + w_3 h_3 \hat{u}_3 \qquad \text{at } x_1 = x_2 = x_{sc},\ x_3 = 0\ , \tag{2.12}$$

where $\tilde{l} = l_{sc*}/l_{b*}$ is the dimensionless length of the secondary channel.

2.3 Results

2.3.1 Model solutions

For the remainder of the analysis, it will be assumed that the width and depth of the main channel are the same in channel 1 and 2. This results in equal wave numbers in both areas, thereby simplifying the analysis. The solutions of sys-

tem (2.5)-(2.12) are

$$\begin{cases} \hat{\eta}_1(x_1) = \dfrac{2e^{\mathrm{i}\kappa_1 x_{sc}}}{(1-\mathrm{i}\alpha)}\Big[\cos(\kappa_1(x_1-x_{sc})) + \alpha\sin(\kappa_1(x_1-x_{sc}))\Big] \\ \qquad \text{for } 0 \le x_1 \le x_{sc} \ , \end{cases} \tag{2.13}$$

$$\begin{cases} \hat{\eta}_2(x_2) = \dfrac{2e^{\mathrm{i}\kappa_1 x_{sc}}}{(1-\mathrm{i}\alpha)}\dfrac{\cos(\kappa_1(1-x_2))}{\cos(\kappa_1(1-x_{sc}))} \\ \qquad \text{for } x_{sc} \le x_2 \le 1 \ , \end{cases} \tag{2.14}$$

$$\begin{cases} \hat{\eta}_3(x_3) = \dfrac{2e^{\mathrm{i}\kappa_1 x_{sc}}}{(1-\mathrm{i}\alpha)}\dfrac{\cos(\kappa_3(\tilde{l}-x_3))}{\cos(\kappa_3\tilde{l})} \\ \qquad \text{for } 0 \le x_3 \le \tilde{l} \ , \end{cases} \tag{2.15}$$

where

$$\alpha = \tan(\kappa_1(1-x_{sc})) + w_3\frac{\kappa_1}{\kappa_3}\tan(\kappa_3\tilde{l}) \ . \tag{2.16}$$

Now, the complex amplitude ratio, CAR $\equiv A_{\mathrm{R}}e^{\mathrm{i}\delta}$, of the wave is computed as the ratio of the wave amplitude in the presence and absence of the secondary channel. The latter situation, identical to a single channel, is computed by using equations (2.13)–(2.16) with $\tilde{l} = 0$. Note that this implies separate solutions of the complex amplitude ratio for stretch 1 and 2 of the main channel, indicated as $\mathrm{CAR}^{(1)}$ and $\mathrm{CAR}^{(2)}$. These results are

$$\begin{aligned} \mathrm{CAR}^{(1)} &= \frac{e^{\mathrm{i}\kappa_1(x_{sc}-1)}}{(1-\mathrm{i}\alpha)}\left[\frac{\cos(\kappa_1(x_1-x_{sc})) + \alpha\sin(\kappa_1(x_1-x_{sc}))}{\cos(\kappa_1(x_1-1))}\right] \ , \\ &\equiv A_{\mathrm{R}}^{(1)}e^{\mathrm{i}\delta^{(1)}} \ , \end{aligned} \tag{2.17}$$

$$\begin{aligned} \mathrm{CAR}^{(2)} &= \frac{e^{\mathrm{i}\kappa_1(x_{sc}-1)}}{(1-\mathrm{i}\alpha)}\frac{1}{\cos(\kappa_1(x_{sc}-1))} \ , \\ &\equiv A_{\mathrm{R}}^{(2)}e^{\mathrm{i}\delta^{(2)}} \ . \end{aligned} \tag{2.18}$$

Note that $\mathrm{CAR}^{(2)}$ is independent of x_2, which will be explained in section 2.4. Equations (2.16), (2.17) and (2.18) reveal that tidal amplification is controlled by three parameters, i.e. x_{sc}, κ_1, and

$$S_f = \frac{w_3}{\kappa_3}\tan(\kappa_3\tilde{l}) \ . \tag{2.19}$$

Parameter S_f, which appears in parameter α, will be called the secondary channel factor and contains all information on dimensions of the secondary channel.

2.3.2 Default system

As a default system, a network is defined, having all parameter values equal to 1, with the exception of μ, which is π, and $\mu\tilde{l}$, which is 0.1. These parameters

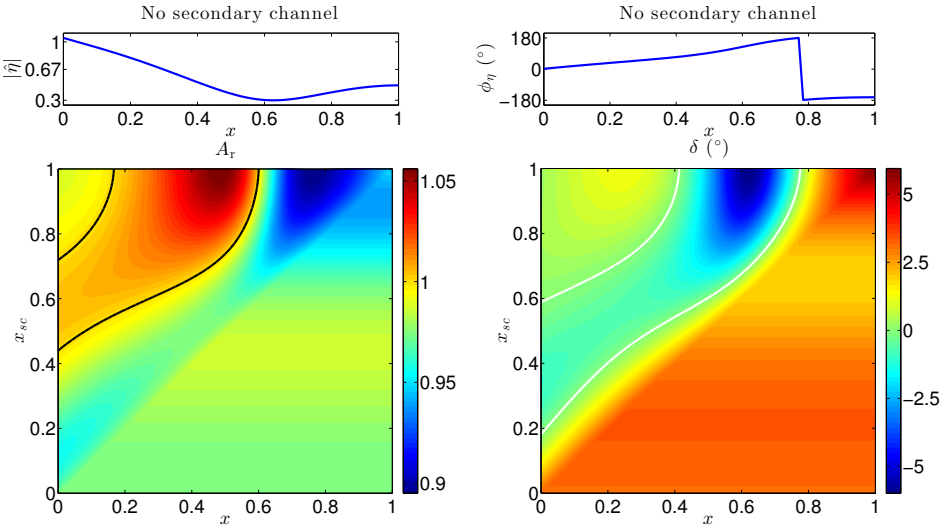

Figure 2.2: Sea surface height characteristics in the main channel for the default case. The left upper panel shows the amplitude in the absence of a secondary channel as a function of distance x to the open boundary. The left lower panel shows the amplitude ratio A_R as a function of x and location x_{sc} of the secondary channel. The right upper panel shows the phase of the sea surface height, ϕ_η, in absence of the secondary channel. The right lower panel shows a colour plot of the phase difference, δ, between the free surface with and without secondary channel.

represent estuaries of intermediate dimensions, such as Chesapeake Bay on the east coast of the United States. Zhong *et al.* (2008) showed that tides in the Chesapeake Bay are partially standing, and that friction is weak to moderate. Moreover this choice ensures that the full dynamics of the mechanism is captured. The top panels of figure 2.2 show the amplitude and phase of the sea surface height, $|\hat{\eta}|$ and ϕ_η respectively, in the main channel for the default case without a secondary channel. Both panels show the partial standing character of the tidal wave. The lower panels show the amplitude ratio and phase shift for the default system, A_R and δ respectively, in the main channel. Parameter δ represents the phase shift between the tides in the presence and absence of the secondary channel.

The left lower panel of figure 2.2 shows the amplitude ratio as a function of x and x_{sc}. The solid black line is the unit contour, separating areas in (x, x_{sc})-parameter space where $A_\mathrm{R} > 1$ from areas in parameter space where $A_\mathrm{R} < 1$. Note that a minimum in the amplitude ratio is observed around $x_{sc} = 0.92$. The amplitude ratio $A_\mathrm{R}^{(2)} < 1$, indicating a decrease in sea surface height amplitude throughout

channel 2 for all locations of the secondary channel. However, in channel 1 values of $A_{\mathrm{R}}^{(1)}$ larger than 1 are observed, hence locally the tide can be amplified. Finally, near $x = 0$ it is found that $A_{\mathrm{R}} \neq 1$, meaning that the secondary channel influences the tidal characteristics at the open boundary. This occurs mainly when the secondary channel is positioned close to the open boundary. The effect becomes smaller when the distance between the open boundary and the secondary channel gets larger and friction causes dampening of the perturbation of the intervention. The right lower panel shows the phase shift, δ, caused by the secondary channel as a function of x and x_{sc}, where solid white lines are the zero-contours. This figure shows that the presence of the secondary channel influences the time of high and low water. This signal is approximately 90° out of phase with the amplitude ratio.

2.3.3 Sensitivity analysis

As a next step, the sensitivity of $A_{\mathrm{R}}^{(2)}$ to S_f, κ_1, and x_{sc} will be investigated. This is done because from a management perspective often the tidal range at the head of the estuary is of importance (Donner *et al.*, 2012). Changing S_f is equivalent to changing the secondary channel characteristics; width w_3, length $\tilde{l}$, depth h_3, and friction coefficient λ_3. Variation in κ_1 is achieved by changing the length (μ) of the main channel and the friction parameter ($\lambda_{1,2,3}$) in the entire network. Finally, changing x_{sc} shifts the position of the secondary channel.

The sensitivity of the amplitude ratio to S_f is shown in the left panel of figure 2.3 for a secondary channel located halfway along the main channel. The real part of S_f is along the horizontal axis and the imaginary part of S_f is along the vertical axis. Colours represent different values of $A_{\mathrm{R}}^{(2)}$. The solid white line indicates the unit contour level.

First, the circles in the figure represent the values of S_f for all parameters having their default values, except that the length of the secondary channel is varied. Each circle indicates an increment of 0.3 in the direction of the arrow, starting in the origin with $\tilde{l} = 0$. The lower left panel shows the value of $A_{\mathrm{R}}^{(2)}$ when following the circles, indicating that for large $\tilde{l}$ the amplitude ratio is a constant. This occurs because the reflected wave gets damped in the secondary channel. Indeed, from equation (2.19) it can be seen that for $\tilde{l}$ approaching infinity, the secondary channel factor goes to a constant value of $\mathrm{i}w_3/\kappa_3$, which is shown by the white dashed line. Increasing the width results in smaller amplitude ratios.

Second, the crosses indicate the functional behaviour of S_f with varying h_3, starting with zero depth in the origin. Again, symbols denote increments of 0.3 in the direction of the arrow. As h_3 becomes large κ_3 approaches zero. Then from equation (2.19) it is seen that $\tan(\kappa_3\tilde{l}) \sim \kappa_3\tilde{l}$, resulting in a constant real secondary channel factor of $w_3\tilde{l}$.

Finally, the plusses show S_f as a function of λ_3. For a frictionless system, $\lambda_3 = 0$,

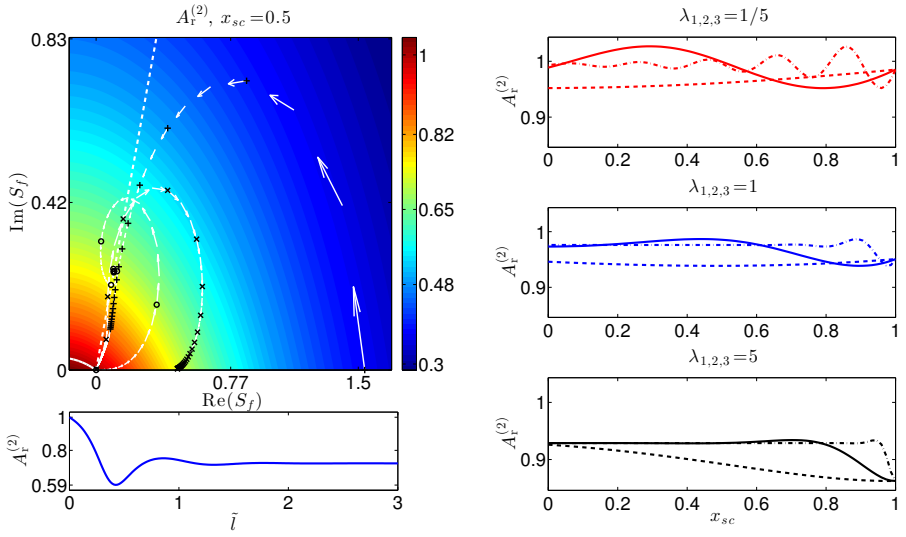

Figure 2.3: Left panel: Colour plot of the amplitude ratio $A_{\mathrm{R}}^{(2)}$ in channel 2 versus the real and imaginary part of the secondary channel factor S_f, defined in equation (2.19). The circles show the behaviour of S_f for varying length $\tilde{l}$ of the secondary channel, the crosses for varying depth h_3, and the plusses for varying friction coefficient λ_3. All markers indicate increments of 0.3 in the respective variable, directed along the arrows. The lower panel shows $A_{\mathrm{R}}^{(2)}$ as a function of $\tilde{l}$ when following the circles. The white dashed line shows the limit as $\tilde{l}$ gets large of the circles for different widths of the secondary channel. Right panel: $A_{\mathrm{R}}^{(2)}$ for different μ and λ as a function of x_{sc}. The solid line represents $\mu = \pi$, the dashed line $\mu = \pi/5$, and the dashed-dotted line $\mu = 5\pi$. The upper panel shows $\lambda_j = 1/5$ (weak friction), the middle panel $\lambda_j = 1$ (moderate friction), and the lower panel $\lambda_j = 5$ (strong friction).

the secondary channel factor is a real number since $\mathcal{I}(\kappa_3) = 0$. For large λ_3, friction is so strong that it prevents wave propagation into the secondary channel, thereby resulting in no modification of the original wave.
Next, $A_{\mathrm{R}}^{(2)}$ is computed for different lengths of the main channel, different friction values throughout the network, and different positions of the secondary channel. The results are presented in the right panels of figure 2.3. The solid line represents the results for the default main channel length, while the dashed (dashed-dotted) line represents those for the case that the length of the main channel is decreased (increased) by a factor of five. The middle panel shows results for the default value of the friction coefficient, while the upper (lower) panel shows those for decreased (increased) friction by a factor five in the entire network.

Increasing friction mainly results in a decreasing value and spatial dependence of the amplitude ratio. A striking feature is observed for the default channel length with low friction (red, solid line). Here, reduction of the amplitude is observed for secondary channel locations from $0.5 \leq x_{sc} \leq 1$, while amplification is observed for locations ranging from $0 \leq x_{sc} \leq 0.5$. Increasing friction results in a decrease of the amplitude ratio, finally leading to the vanishing of positions for which amplification is found.

2.4 Discussion

2.4.1 Physical mechanism

First, the mechanism will be discussed that causes the differences in amplitude and phase of the tidal wave in the main channel due to the presence of the secondary channel. The situation sketch in figure 4(a) shows the incoming waves (solid arrows) and outgoing waves (dashed arrows) in all channels. The forcing at the open boundary generates a primary wave (blue arrow) that propagates into the channel. At the vertex point it triggers a partially standing wave (purple arrows) in the secondary channel. The latter leads to two secondary (radiated) waves in the main channel, one incoming and one outgoing (cyan solid and black dashed arrows, respectively). The incoming primary wave (which, by definition, is unaffected by the secondary channel) and the incoming radiated wave reflect at the landward boundary. The resulting outgoing waves additionally affect the partially standing wave in the secondary channel.
The complex amplitude ratio in channel 2, $\mathrm{CAR}^{(2)}$, is determined for every x by the ratio of the complex amplitude $A_{2,1}$ of the incoming wave at the vertex point in the presence, and in the absence of the secondary channel. Furthermore, it is a constant because the incoming waves in channel 2 experience identical friction regardless of the presence of a secondary channel. According to equations (2.6), (2.7) and (2.13), the amplitude of the incoming primary wave at the vertex point can be written as $e^{\mathrm{i}\kappa_1 x_{sc}}$. Thus the complex amplitude ratio reads

$$\mathrm{CAR}^{(2)} = 1 + A_{rad} e^{-\mathrm{i}\kappa_1 x_{sc}} \ . \tag{2.20}$$

By combining equations (2.9), (2.10) and (2.12), the amplitude of the incoming radiated wave at the vertex point can be written in terms of the amplitude of the outgoing wave at the vertex point from the side-channel as

$$A_{\mathrm{rad}} = \frac{w_3 \kappa_1}{2\kappa_3} (1 - e^{-2\mathrm{i}\kappa_3 \tilde{l}}) A_{3,2} \ ,$$

which for a short secondary channel ($\mu\tilde{l} \ll 1$) simplifies to

$$A_{\mathrm{rad}} \approx \mathrm{i} w_3 \kappa_1 \tilde{l} \ A_{3,2} \ . \tag{2.21}$$

Furthermore, the combination of the equations (2.8)-(2.11) yields for the amplitude of the outgoing wave in the secondary channel at the vertex point

$$A_{3,2} = \frac{1 + e^{2\mathrm{i}\kappa_1(1-x_{sc})}}{1 + e^{-2\mathrm{i}\kappa_3\tilde{l}}}(e^{\mathrm{i}\kappa_1 x_{sc}} + A_{\mathrm{rad}}) \ .$$

Again assuming $\mu\tilde{l} \ll 1$ and using equation (2.21), this can be approximated as

$$A_{3,2} \approx \frac{1}{2}(1 + e^{2\mathrm{i}\kappa_1(1-x_{sc})})e^{\mathrm{i}\kappa_1 x_{sc}} \ . \tag{2.22}$$

By substituting equations (2.21) and (2.22) into equation (2.20), the solution for the complex amplitude ratio becomes

$$\mathrm{CAR}^{(2)} \approx 1 + \mathrm{i}w_3\kappa_1\tilde{l}\cos(\kappa_1(1 - x_{sc}))e^{\mathrm{i}\kappa_1(1-x_{sc})} \ .$$

Now, the low friction limit ($\mathcal{I}(\kappa_j) = 0$) is considered, as it yields considerable insight into the modifying mechanism of the tide due to the secondary channel. The amplitude ratio in this limit reads

$$A_{\mathrm{R}}^{(2)} \approx \left[1 - w_3\kappa_1\tilde{l}\sin(2\kappa_1(1 - x_{sc}))\right]^{1/2} \ .$$

Now, tidal range decreases ($A_{\mathrm{R}}^{(2)} < 1$) when $\sin(2\kappa_1(1-x_{sc})) > 0$, while tidal range increases when $\sin(2\kappa_1(1-x_{sc})) < 0$. Thus, positions of the secondary channel resulting in smaller tidal ranges are those for which the secondary channel is located less than a quarter wavelength away from the closed end of the main channel, i.e. $0 \leq \kappa_1(1 - x_{sc}) \leq \frac{1}{2}\pi$, modulo π. Amplification occurs for $\frac{1}{2}\pi \leq \kappa_1(1 - x_{sc}) \leq \pi$, modulo π. The minimum (maximum) amplitude ratio is observed at 1/8 times the wavelength of the tidal wave seaward from the open end (nodal point), since the radiated wave is strongest when both sea surface height amplitude and velocities are large.

The amplification is caused by the fact that, if the secondary channel is located more than a quarter wavelength from the closed end (figure 2.4(b)), it discharges its water into the main channel during flood tides. This is because the maximum velocity amplitude is attained in the nodal point of the primary wave. Consequently, velocities are smaller in front of the secondary channel than behind it when the secondary channel is located seaward from the nodal point. When the secondary channel is located landward from the nodal point the reverse processes occur, causing the secondary channel to discharge water in the main channel during ebb, leading to reduction of the tidal range in channel 2 (figure 2.4(c)).

2.4.2 Relevance and limitations

This study has yielded fundamental insight in the mechanisms dominating the response of channel networks to changes in network geometry, which has important implications for engineering works. There, man-made secondary channels are

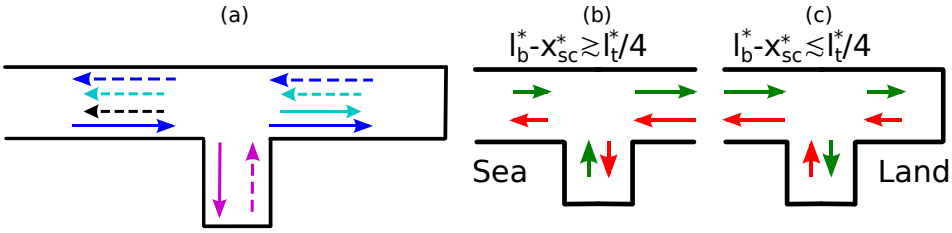

Figure 2.4: (a) Incoming and outgoing waves in the domain. Solid arrows depict incoming waves, while dashed arrows depict outgoing waves. (b) Flood (green arrows) and ebb (red arrows) velocities around the secondary channel located close to the nodal point of the forcing wave. For locations seaward of the nodal point mass is extracted from the secondary channel during flood. (c) As panel (b) but for a secondary channel located landward of the nodal point. Now, mass is extracted from the secondary channel during ebb.

considered as a measure to reduce tidal range in estuaries, e.g. in the Ems estuary situated at the Dutch-German border.

It was shown that for short secondary channels the amplitude of the modulating tidal wave was small ($O(\mu\tilde{l})$) compared to that of the forced incoming wave. Therefore, adding a new secondary channel to the system leads to a linear addition of its effect, since the response of the interaction between the secondary channels in the main channel is $O((\mu\tilde{l})^2)$.

The chosen representation of the system is obviously simplified. However, results with a sloping bottom in the main channel indicate that for realistic bottom slopes, i.e. a decrease in depth of up to half the initial depth, the behaviour is qualitatively similar as that for a constant depth. Similarly, changing the secondary channel to a Helmholtz basin with a narrow inlet channel followed by a wider basin yields no qualitative changes in the model results. Moreover, the linear friction coefficient should be obtained through a linearisation procedure of the quadratic bottom stress (cf. Zimmerman, 1992, and references therein). The coefficient obtained by considering only the main channel might not be representative for the network, which includes a secondary channel. Nevertheless, numerical experiments with a quadratic bottom stress show very similar results, indicating little sensitivity to the linearisation procedure.

Finally, note that although this research was applied to tidal characteristics, it can also be used to compute resonance characteristics of long gravity waves in harbours.

2.5 Conclusions

This study has resulted in both quantitative and qualitative assessment of the dependence of amplitude and phase of tidal waves in a semi-enclosed channel on the geometrical characteristics of a secondary channel. For this, analytical solutions of the linear one-dimensional shallow water equations, which govern the tidal motion in the network due to an imposed incoming wave at the open boundary, have been constructed and interpreted. From these an amplitude ratio has been defined as the ratio of the local amplitude of the sea surface height in the main channel in the presence and in the absence of the secondary channel.

For lengths of the main channel of the order of the tidal wave-length, short secondary channels and weak friction, it has been found that the secondary channel causes tides in the main channel to weaken (amplitude ratio < 1) if it is located between a node and the successive landward located antinode of the tide. Conversely, if the secondary channel is located between a node and the successive seaward located antinode, it causes tides in the main channel to become more resonant. The physical mechanism underlying this behaviour is that in the former case tidal velocities in the main and secondary channel near the vertex point are in phase, so that e.g. during flood the secondary channel accommodates part of the incoming water volume. In the latter case these velocities are out of phase and thus the opposite occurs.

Results reveal that there are optimum lengths and depths of the secondary channel for which the changes in tidal resonance characteristics in the main channel are maximum. Larger widths cause the amplitude ratio to become small. Increasing friction in, and/or reducing the length of the main channel causes the variations of the amplitude ratio to become less pronounced. These conclusions are robust with respect to mild depth variations within channels, varying the shape of the secondary channel and to the detailed formulation of bottom friction. The results obtained are of interest in the context of possible construction of retention basins in estuaries to effectively reduce tidal range.

Chapter 3

Effect of a secondary channel on the non-linear tidal dynamics in a semi-enclosed channel: a simple model

3.1 Introduction

Estuaries and semi-enclosed basins, which are common features of coastlines, often experience strong tidal motion. Many of these bodies of water consist of channels, connected in a network, such as the Yangtze estuary (China) (Jiang *et al.*, 2012) and Chesapeake Bay (USA) (Zhong *et al.*, 2008). Moreover, they are often subject to human influences, such as channel dredging and construction of secondary channels. Thus, knowledge about tidal dynamics in such semi-enclosed basins is important, e.g. for flood risk assessment or ecological management.

This study uses a simple model to gain insight into changes of the tidal propagation through a main channel due to a secondary channel. The advantage of simple models is that they are fast and flexible and yield a qualitative idea of the dynamics of the system. So far, simple models focused on the process that changes the resonance characteristics of a secondary channel. This process, called radiation damping, was investigated for tidal dynamics by Buchwald (1971); Garrett (1975) and Zimmerman (1992), who studied an elongated channel connected to a frictionless sea. They found that resonant modes of the secondary channel are damped by the outward radiation of waves from the entrance of the secondary channel. Defant (1961) studied branching in semi-enclosed basins for frictionless

This chapter is based on:
Alebregtse, N. C. & de Swart, H. E. 2014 Effect of a secondary channel on the non-linear tidal dynamics in a semi-enclosed channel: a simple model. *Ocean Dynamics* **64** (4), 573–585.

systems. He computed the eigenfrequency of such systems but did not investigate any further detailed resonance characteristics.
Recently, Alebregtse *et al.* (2013) studied the changes of tidal characteristics in a main channel due to the presence of a secondary channel, for varying positions and dimensions of the secondary channel. One of their main results was that, if friction is low, a secondary channel reduces tidal range at the head of a main channel when it is positioned less than a quarter tidal wavelength from the closed end of the main channel.
Two important limitations of the work done so far is that only sea surface variations were analysed and not velocity, and that only linear dynamics were considered. The tidal range was thus not influenced by the generation of internal overtides, nor was the transition period from high to low water (and vice versa) changed by the secondary channel. These issues are important because previous human interventions in estuaries have led to an increase in tidal range. Possible constructions of secondary channels to reduce tidal range are presently considered by managers, e.g. in the Ems estuary (Dutch-German border, Donner *et al.*, 2012).
The specific objectives of this study are twofold. The first is to test the hypothesis that distortions of the tide due to the presence of a secondary channel are generated locally, after which they propagate through the network. In that case, the behaviour of a specific tidal harmonic in the nonlinear model is similar to that of the harmonic in the linear model. The second objective is to quantify the effect of the secondary channel on tidal asymmetry in the network.
To meet the first objective, model results will be processed with harmonic analyses decomposing the signal in the M_2, M_4 and M_6 constituents. This will be done for a main channel only, as well as for a network with a secondary channel. The influence of the secondary channel on both the vertical tide and the horizontal tide will be assessed. The results for sea surface height will be compared with those of Alebregtse *et al.* (2013) to test the posed hypothesis. To meet the second objective, the non-linear tidal curves of both sea surface height and velocity will be analysed. Again, this is done by first considering only a main channel, and afterwards adding a secondary channel. The influence of the secondary channel on the asymmetry of the tide in the main channel will be quantified by analysing the tidal range and the duration of the falling tide as sea surface height characteristics, and the flood-to-ebb current ratio and the duration between maximum flood and ebb as velocity characteristics. The flood-to-ebb current ratio velocity asymmetry determines the net bedload transport of sediment (Aubrey, 1986; Friedrichs & Aubrey, 1988), while the duration between maximum flood and ebb is also important for suspended load transport (Groen, 1967). Therefore, changes in the asymmetries in velocity can indicate alterations of the direction and magnitude of net sediment transport.
The contents are as follows. In section 3.2, the model and analysis methods will

be presented. Results are presented in section 3.3. In section 3.4, these results will be discussed and section 3.5 will summarise the conclusions.

3.2 Model and methods

3.2.1 Model

The hydrodynamics are considered on a domain consisting of three channels, as shown in figure 3.1. Channel 1 and 2 constitute a main channel of length l_b. The width and depth are constant throughout channel 1 and channel 2. Channel 3 represents a secondary channel of length l_{sc}, which can have a different depth and width than those of the main channel. Each channel has a rectangular cross-section. Along channel position in the channels is described by an x_j coordinate ($j = 1, 2, 3$ is the channel index), ranging from $0 \leq x_1 \leq x_{sc}$, $0 \leq x_2 \leq (l_b - x_{sc})$, and $0 \leq x_3 \leq l_{sc}$ for channel 1, 2, and 3, respectively. There is also a general x coordinate, which is the coordinate for the main channel only.
The water motion is described by the one-dimensional, non-linear, cross-sectionally averaged shallow water equations. These are the along-channel momentum equation and the continuity equation,

$$\frac{\partial u_j}{\partial t} + u_j \frac{\partial u_j}{\partial x_j} = -g \frac{\partial \eta_j}{\partial x_j} - c_{d,j} \frac{|u_j| u_j}{h_j + \eta_j} \ , \tag{3.1}$$

$$\frac{\partial \eta_j}{\partial t} = -\frac{1}{w_j} \frac{\partial}{\partial x_j} \Big(w_j (h_j + \eta_j) u_j \Big) \ . \tag{3.2}$$

Here, u_j is the along-channel velocity, η_j the free surface elevation, t the time, w_j the channel width, h_j the channel depth, g the acceleration due to gravity, and $c_{d,j}$ the drag coefficient.
The system is forced by imposing only an incoming tidal wave at the open boundary of the main channel. This approach is based on the assumption that the incoming information in the domain is unchanged by changing conditions in the domain (such as adding a secondary channel). When modelling a system with a fixed sea surface elevation at the open boundary, the sum of the incoming and reflected waves from the domain are fixed.
To allow forcing of the system with only incoming information, Eqs (3.1) and (3.2) are analysed using the method of characteristics as described by Dronkers (1964) and Whitham (1974). This method uses Riemann invariants $r_j^{(k)}$ that carry information about the system along the characteristics with a velocity $c_j^{(k)}$ determined by the system. Eqs (3.1) and (3.2) translate to

$$\frac{dr_j^{(k)}}{dt} + f_j^{(k)}(x_j, t, u_j, \eta_j) = 0 \qquad \text{on } \frac{dx_j}{dt} = c_j^{(k)} \ , \tag{3.3}$$

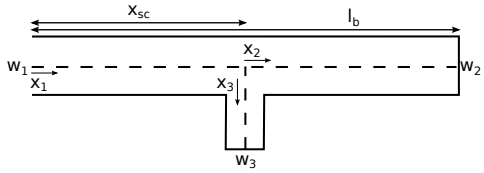

Figure 3.1: Model domain consisting of a main channel and secondary channel with the x_j-coordinates in the direction parallel to the main axis. The width continues smoothly in the main channel (from channel 1 to channel 2), which has a length l_b. The secondary channel is located at x_{sc} and has a length l_{sc}.

with $k = +$ or $k = -$,

$$r_j^{(k)} = u_j \pm 2\sqrt{g(h_j + \eta_j)} \ , \tag{3.4}$$

$$c_j^{(k)} = u_j \pm \sqrt{g(h_j + \eta_j)} \ , \tag{3.5}$$

$$f_j^{(k)} = c_{d,j} \frac{|u_j| u_j}{h_j + \eta_j} \ . \tag{3.6}$$

Note that in Eq 3.6 the width and depth have been considered constant, which will be used for the remainder of the analysis. A derivation of Eqs (3.3)–(3.6) is given in appendix 3.A.
The condition at the open boundary is prescribed as a purely incoming wave, where the incoming wave has a sea surface elevation consisting of only an M_2 tidal component,

$$r_1^{(+)} = 4\sqrt{g(h_1 + A\sin(\sigma t))} - 2\sqrt{g h_1} \qquad \text{at } x_1 = 0 \ , \tag{3.7}$$

with A an arbitrary amplitude and $\sigma = 2\pi/T$ the tidal frequency (T the tidal period). Due to the non-linear dependence of $r_j^{(k)}$ on η_j, the velocity signal of the incoming wave contains overtides at $x = 0$. Besides, five more conditions have to be prescribed. Two of those are the landward boundary conditions of the main channel and secondary channel, which are closed, i.e.

$$u_j = 0 \qquad \text{at} \begin{cases} j = 2, 3, \\ x_2 = (l_b - x_{sc}) \ , \\ x_3 = l_{sc} \ . \end{cases} \tag{3.8}$$

The other conditions arise from matching conditions at the vertex point, i.e. the point where the secondary channel connects to the main channel. First, continuity

of dynamic pressure must hold, i.e.

$$g\eta_j + \frac{1}{2}u_j^2 = g\eta_1 + \frac{1}{2}u_1^2 \qquad \text{at} \begin{cases} j = 2, 3, \\ x_1 = x_{sc}, \\ x_2 = x_3 = 0 \ . \end{cases} \tag{3.9}$$

Note that Eq (3.9) comprises two conditions.
The final matching condition is that the volume transport must be continuous,

$$A_1 u_1 = A_2 u_2 + A_3 u_3 \ , \qquad \text{at} \begin{cases} x_1 = x_{sc}, \\ x_2 = x_3 = 0 \ , \end{cases} \tag{3.10}$$

where $A_j = w_j(h_j + \eta_j)$ is the cross-sectional area of each channel at the vertex point.

3.2.2 Methods

Time integration

The system of Eqs (3.3) to (3.10) is solved by a numerical forward Euler time-stepping scheme. At each time step the new values of the Riemann invariants, $r_j^{(k)}$ are computed, as well as their changes in position x_j. Note that the change in x_j is different for the positive and negative Riemann invariant. After each time step, the solutions for $r_j^{(k)}$ are linearly interpolated back to the original grid for convenience of visualising and analysing the data.
First, the differential equations are solved every time step, after which values at the boundaries are replaced by the results from the boundary conditions. This is a valid approach, since propagation of information can be traced through the network. The condition at the closed boundary determines the negative Riemann invariant, since its positive counterpart arrives from the interior of the domain. The same reasoning applies to the matching conditions at the vertex point, meaning that for channel 1 the local negative Riemann invariant is solved, while for channel 2 and 3 the local positive Riemann invariants are solved. Since the matching conditions are non-linear, they are solved by means of a Newton-Raphson iterative procedure, which uses the solutions to the linearised equations as the initial value.

Analysis

The resulting time series for the sea surface height and velocity are harmonically analysed. Thus, the signals are decomposed in the semi-diurnal tidal component and its overtides, where the latter have integer times the frequency of the M_2

component,

$$\xi \approx \sum_{p=0}^{\infty} C_{\xi,p} \cos(p\sigma t - \chi_{\xi,p}) \ . \tag{3.11}$$

The ξ is the variable under consideration, either sea surface height or velocity, $C_{\xi,i}$ is the amplitude of component p and has a phase $\chi_{\xi,i}$. The different tidal constituents can be attributed to various non-linear processes (Parker, 1991).
The amplitudes and phases of the tidal components are analysed, both in a main channel without secondary channel, as well as in a network like in figure 3.1. From these, amplitude ratios are computed, which are defined for both sea surface height ($A_{r,p}$) and velocity ($V_{r,p}$) as the ratio between the amplitude of a harmonic constituent in presence and absence of the secondary channel, where p denotes which tidal component is analysed ($p = 1, 2, 3$). Also, phase shifts are calculated for sea surface height ($\Delta\phi_p$) and velocity ($\Delta\theta_p$), defined for a specific harmonic as the difference between the phase in the presence and absence of the secondary channel.
The presence of overtides, which result from nonlinear processes, causes the tidal curves (of both sea surface height and velocity) to be asymmetric. The degree of asymmetry of the full signals is determined by computing 4 quantities, viz. the tidal range, the duration of the falling tide (DFT), the ratio of maximum flood and maximum ebb velocities, and the duration between maximum flood and maximum ebb (DFE) (see figure 3.2). If the maximum flood velocity is larger than the maximum ebb velocity, the flow is called flood dominant (Friedrichs & Aubrey, 1988). If DFE is larger than half the tidal cycle the duration of slack after flood is larger than the duration of slack after ebb. This induces net sediment transport in the flood direction due to temporal settling lag (Groen, 1967; Dronkers, 1986). Figure 3.2 shows time series from the model for both sea surface height (panel a) and velocity (panel b) depicting the four asymmetry quantities.

3.3 Results

Firstly, a network will be defined. Secondly, the results from the harmonic analysis will be presented for a network both with and without secondary channel. Thirdly, the asymmetry of the tidal curves will be quantified by calculating the four asymmetry parameters that were defined in section 3.2.2. Again, the first model configuration consists of only a main channel after which the secondary channel is added. Finally, the sensitivity of tidal range at the closed end of the main channel for different secondary channel dimensions will be investigated.

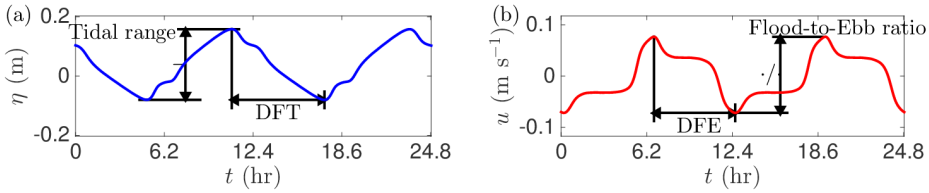

Figure 3.2: Time series as computed by the model indicating the definition of the four asymmetry quantities. Panel (a) shows sea surface height quantities tidal range and the duration of the falling tide (DFT). Panel (b) shows the maximum flood to maximum ebb ratio and the duration between maximum flood and maximum ebb (DFE).

3.3.1 Values of the model parameters

The network that is considered in this study is described by the parameters given in table 3.1. Values of the parameters are chosen, such that the length of the main channel equals half the M_2 tidal wavelength. These values are representative for long basins with small secondary channels. The sensitivity analysis will test the robustness of the results.

3.3.2 Harmonic analysis, no secondary channel

First, only a main channel is considered. Figure 3.3 shows the amplitude and phase of the harmonic components as a function of x/l_b for sea surface height and velocity. Here, x is the distance to the open boundary and l_b is the length of the

Table 3.1: Parameter value settings for the default system

Parameter	Value	Unit
h_j $(j = 1, 2, 3)$	10	m
w_j $(j = 1, 2, 3)$	180	m
σ	$1.4 \cdot 10^{-4}$	s^{-1}
$c_{d,j}$ $(j = 1, 2, 3)$	10^{-3}	
A	0.5	m
l_t	440	km
l_b	220	km
l_{sc}	7	km

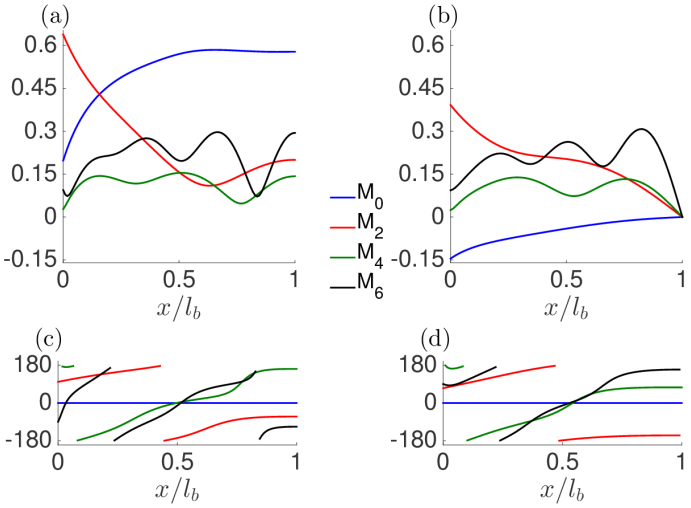

Figure 3.3: Harmonic analysis of time series in the main channel in absence of the secondary channel. Panel (a) shows the sea surface height amplitudes in the main channel as a function of the normalised coordinate x/l_b. The M_2 amplitude is in m, while all other tidal harmonics are in dm. Similarly, panel (b) shows velocity amplitudes in m/s for M_2 and in dm/s for the other harmonics. Panel (c) and (d) give the phase of the tidal harmonics in degrees for sea surface height and velocity, respectively.

main channel. At $x = 0.59$, a minimum is observed in the M_2 sea surface height amplitude (panel (a), red line), due to the partially standing nature of the tidal wave. This minimum is referred to as the remainder of a nodal point. The partially standing character can also be seen in the phase of the M_2 tide (panel (c), red line): with increasing x it first increases, while towards the land it becomes constant.

The residual component and all tidal components, except M_2, show larger amplitudes towards the closed end of the channel, which results from the internal generation of overtides. The remainders of nodal points are also observed for the higher harmonics of the tide.

The velocity amplitude of the M_2 tidal component gradually decreases towards the landward end of the main channel. Similar to the sea surface height, the velocity overtides also have increasing amplitudes towards the closed end of the main channel. Especially the M_6 component is strong, which results from quadratic bottom stress. This was concluded after conducting an experiment in which the bottom stress was linearised, resulting in a decline of the M_6 component.

From figure 3.3, it also becomes apparent that the overtides are predominantly internally generated, as the amplitudes of the higher harmonics are close to zero at the open boundary.

3.3.3 Harmonic analysis, with secondary channel

Sea surface height

Figure 3.4 shows the sea surface height amplitude ratio ($A_{r,p}$) of the first three tidal harmonics, for different normalised locations x/l_b in the main channel and for different normalised locations x_{sc}/l_b of the secondary channel. Panels (a), (c), and (e) contain results produced by the non-linear model, whereas panels (b), (d), and (f) show results generated by the linear model of Alebregtse *et al.* (2013). As the linear model does not produce internal overtides, the M_4 and M_6 component of the linear model result from forcing an incoming tidal component of the corresponding frequency at the open boundary.
Qualitatively, the results of the linear and non-linear model are similar for every tidal harmonic. Differences in pattern arise predominantly for the amplitude ratios of the overtides near the open boundary for locations of the secondary channel in the vicinity of this boundary. Quantitatively, there is also good agreement between the different modelling approaches. The M_2 and M_6 amplitude ratios are slightly higher in the linear model, while that of M_4 is lower. Moreover, near the open boundary the amplitude ratio of the overtides is more pronounced in the non-linear model than in the linear model.

Another difference between the results of the linear and non-linear model is seen in the area of the main channel that lies landward of the vertex point. The amplitude ratio is a constant there in the linear model, which is a result from identical friction experienced by the tidal wave in the presence and absence of a secondary channel. This is no longer true for the non-linear model, as the radiated wave from the secondary channel locally changes the velocity field and thus the friction.
Regarding the phase shift of the harmonic components in sea surface height ($\Delta\phi_p$) induced by the secondary channel (figure 3.5), the results of the non-linear model also compare qualitatively well with those of the linear model, except near the entrance (not shown). Quantitatively there are differences, as the non-linear model computes more pronounced patterns of phase change for the overtides than the linear model. Differences between the models for these tidal harmonics reach up to 30° in modelled phase shift. The phase shifts computed by the non-linear model are shown in figure 3.5 as functions of x/l_b and x_{sc}/l_b.
Note that, although the patterns of the amplitude ratio obtained with the linear and non-linear model are comparable for all harmonic constituents, the linear model is unable to simulate the correct magnitude of the overtides in the main channel in the absence of a secondary channel. Moreover, the phase shift of the

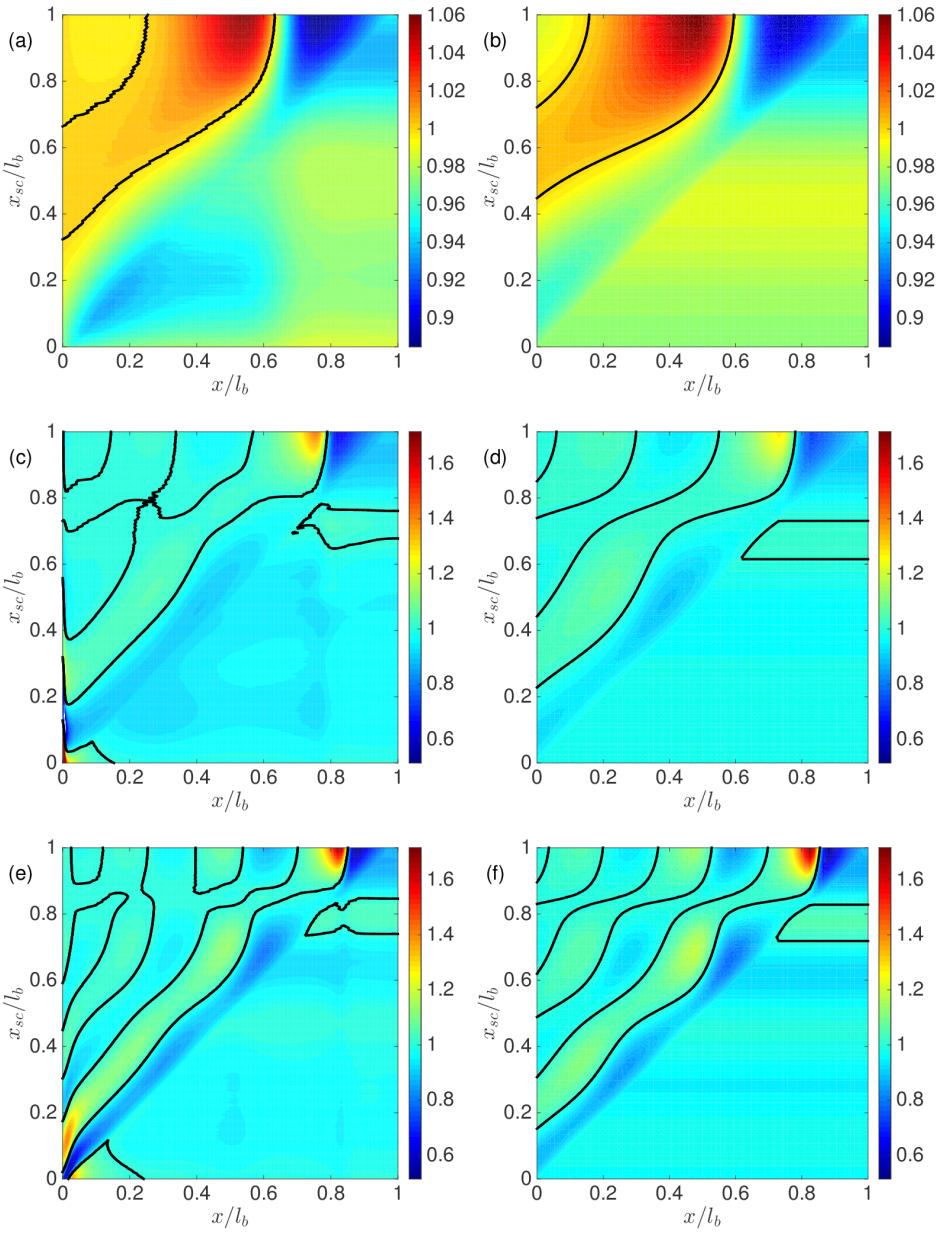

Figure 3.4: Amplitude ratios $A_{r,p}$ of sea surface height amplitude in the presence and absence of a secondary channel for M_2 (panel (a) and (b)), M_4 (panel (c) and (d)) and M_6 (panel (e) and (f)) as a function of x/l_b and the normalised location of the secondary channel x_{sc}/l_b. For comparison, the linear model results from Alebregtse *et al.* (2013) are plotted in panel (b), (d), and (f). Solid black lines are the unit contour.

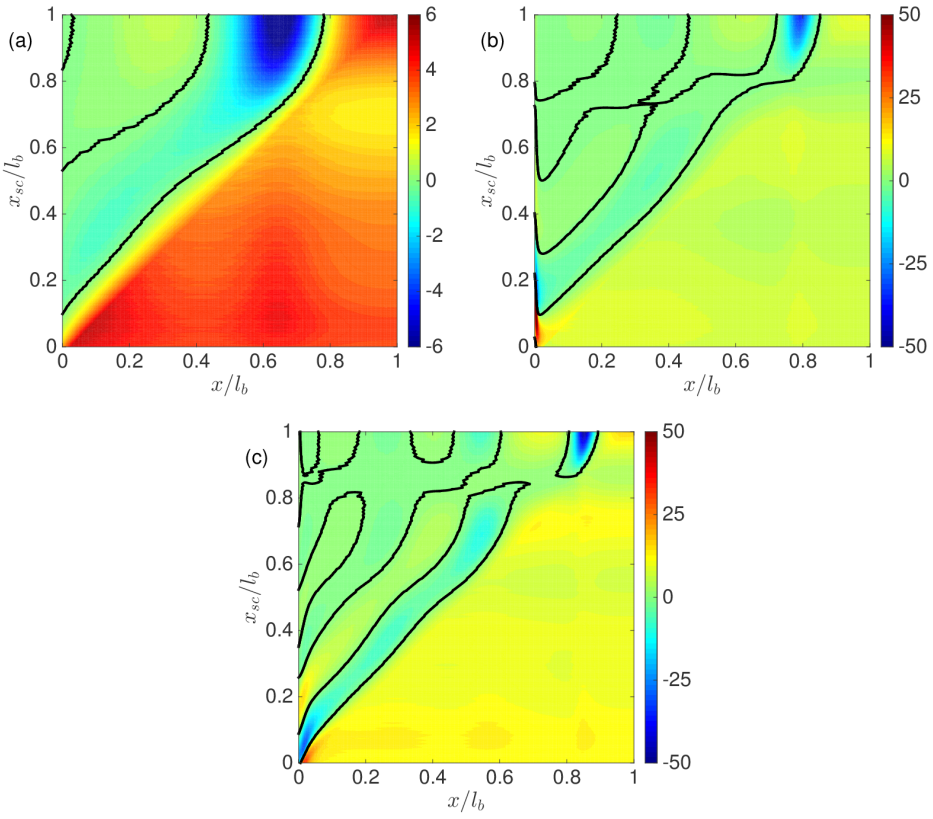

Figure 3.5: Phase shift $\Delta\phi_p$ between the harmonic components in the presence and absence of a secondary channel of sea surface height M_2 (panel (a)), M_4 (panel (b)) and M_6 (panel (c)) as a function of x/l_b and x_{sc}/l_b. Solid black lines are the zero contour.

M_4 and M_6 tidal harmonic is underestimated by the linear model. Therefore, the non-linear model provides important information on the non-linear propagation of tides through branching networks.

Velocity

Figure 3.6 shows the amplitude ratios of the first three harmonic constituents of the tidal velocity field ($V_{r,p}$) as functions of x/l_b and x_{sc}/l_b. These ratios turn out to be mostly of comparable magnitude as those of the sea surface height for all harmonic components, which were shown in figure 3.4. An exception concerns the

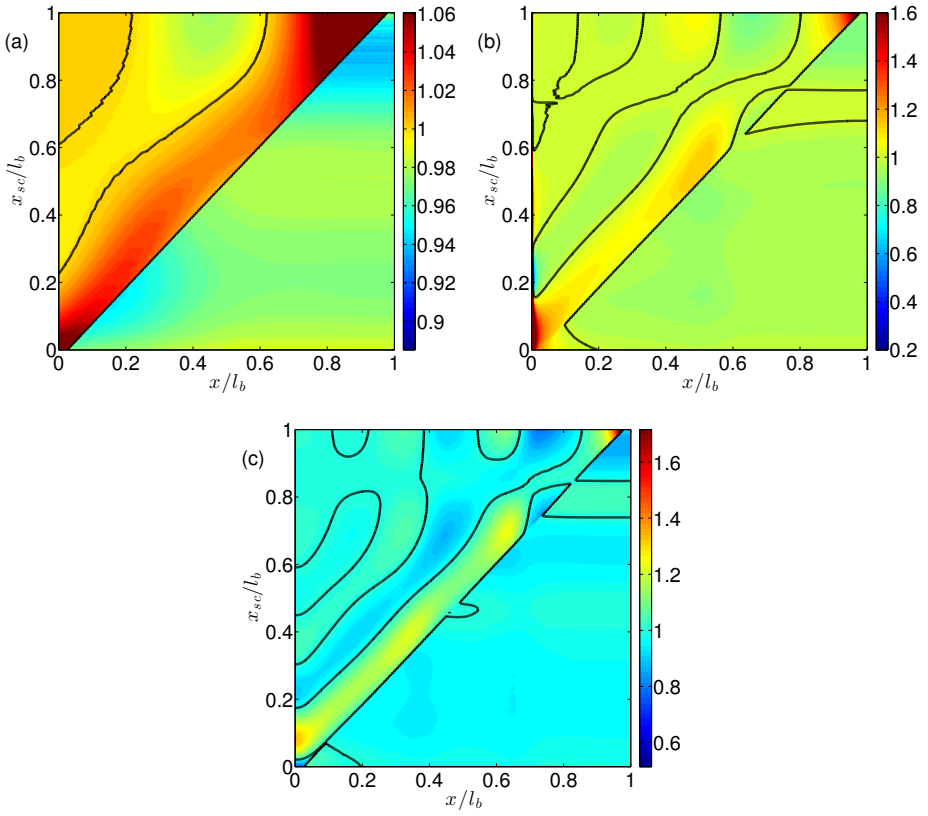

Figure 3.6: As figure 3.4 panel (a) through (c), but for the velocity amplitude ratios $V_{r,p}$. For $x > x_{sc}$ patterns in $V_{r,p}$ are very similar to those in $A_{r,p}$.

area close to the secondary channel, when that channel is positioned close to the landward end; Here $V_{r,p}$ is significantly larger than $A_{r,p}$. Furthermore, landward of the vertex point $V_{r,p}$ is also spatially similar to $A_{r,p}$. The maximum value attained by the velocity amplitude ratio is approximately 2, which is of the scale for $V_{r,2}$ and $V_{r,4}$. However, in the vicinity of the landward end, the velocity tends towards zero, due to the closed boundary. Thus, velocities remain small, despite the large relative increase.

Figure 3.7 shows the phase changes ($\Delta\theta_p$) occurring in the harmonic components of the velocity in dependence of x/l_b and x_{sc}/l_b. The changes that occur in the phase of the velocity landward of the vertex point also resemble the phase shift in sea surface height. Seaward of the vertex point the phase shift is generally smaller for the velocity than for sea surface elevation. There, patterns are also similar

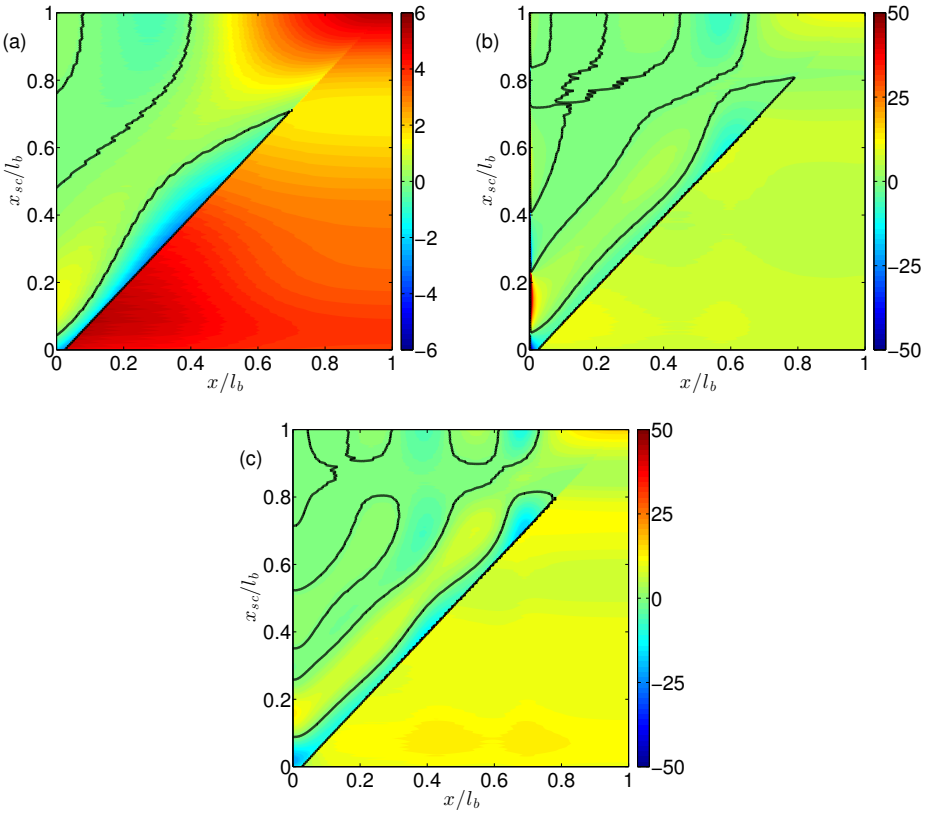

Figure 3.7: As figure 3.5, but for the phase shift $\Delta\theta_p$ in the velocity harmonics. For $x > x_{sc}$ patterns in $\Delta\theta_p$ are similar to those in $\Delta\phi_p$.

to those in the phase shift in the sea surface height (figure 3.5), but are shifted seaward.

3.3.4 Tidal curves, no secondary channel

To assess the spatial structure of tidal asymmetry in the main channel, the full time series of sea surface height and velocity are considered. When no secondary channel is present, the tidal signal near the open boundary appears as is shown in the upper panel figure 3.8. Both sea surface height and velocity are almost sinusoidal at this location. In contrast, the lower panel of figure 3.8 shows that the time series of sea surface height and velocity near the closed end of the main channel are highly asymmetric.

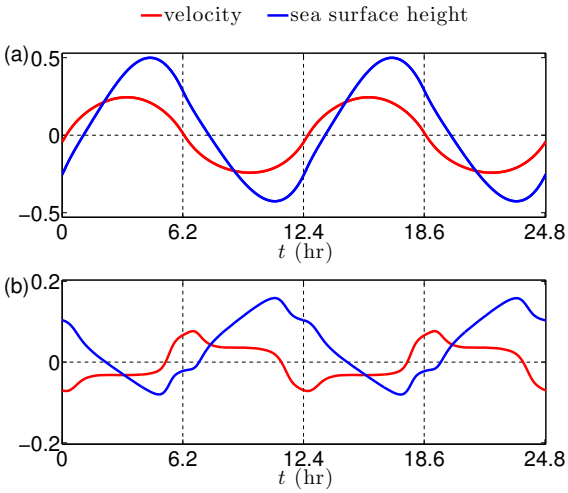

Figure 3.8: Time series of velocity (red) and sea surface height (blue) in the absence of a secondary channel at $x = l_b/10$ (panel (a)) and at $x = 9l_b/10$ (panel (b)).

Figure 3.9(a) shows the tidal range as a function of x/l_b in the main channel when the secondary channel is absent. The pattern of the tidal range resembles that of the M_2 tidal amplitude of sea surface height (see figure 3.3(a)). The tidal range attains a minimum around $x/l_b = 0.59$, which was also observed in the M_2 amplitude in figure 3.3.

The DFT relative to the tidal period T is shown in figure 3.9(b). It shows that DFT $> 1/2$ in the entire domain, thereby revealing that high water crests move faster than low water troughs. The flood-to-ebb velocity ratio is shown in figure 3.9(c). There is a short distance along the main channel $x < 0.2$, where the system is ebb dominant. However, most positions in the main channel experience stronger flood currents.

Finally, figure 3.9(d) shows DFE in units of the tidal period, at different locations in the main channel in absence of the secondary channel. It reveals that the main channel has a shorter transition from ebb to flood than from flood to ebb up to 60% into the main channel. The change between these two domains occurs around the location of the tidal range minimum.

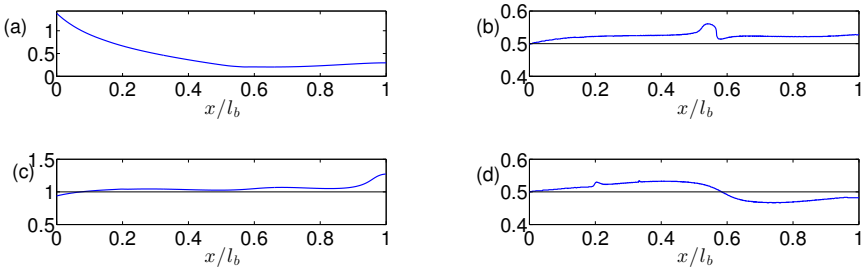

Figure 3.9: The asymmetry parameters as a function of x/l_b in the absence of a secondary channel: (a) tidal range; (b) duration of the falling tide (DFT, in units of the tidal period T), revealing high water travels faster than low water; (c) flood-to-ebb ratio ($|u_{fl}|/|u_{ebb}|$), a small area ($x/l_b < 0.2$) shows ebb dominant currents; (d) duration between maximum flood and maximum ebb (DFE, in units of the tidal period T).

3.3.5 Tidal curves, with secondary channel

Sea surface height

The spatial distribution of the tidal range (figure 3.9(a)) strongly resembles that of the M_2 amplitude (figure 3.3(a)). In contrast, the pattern of the tidal range ratio, shown in figure 3.10(a), displays several new features, when compared with the amplitude ratio of the M_2 sea surface height (see figure 3.4(a)). One of these is the anti-diagonal in the (x, x_{sc})-parameter space indicated by a solid white line for positions of the secondary channel landward of the tidal range minimum where the tidal range ratio has a minimum. This local minimum in tidal range ratio indicates the reduction of the tide achieves a local maximum. Its origin will be discussed in section 3.4.
The differences in DFT (ΔDFT) in the main channel induced by the presence of a secondary channel are shown in figure 3.10(b), Also here, an anti-diagonal in the (x, x_{sc})-parameter space is present. When the secondary channel is positioned at the location where tidal range attains a minimum, a near uniform increase in DFT is observed landward of the secondary channel, indicating that the difference in speed between high water and low water has increased due to the secondary channel.

Velocity

Figure 3.11(a) shows a contour plot of the ratio of flood-to-ebb velocity ratio U_r in the main channel for different locations of the secondary channel. Applying this

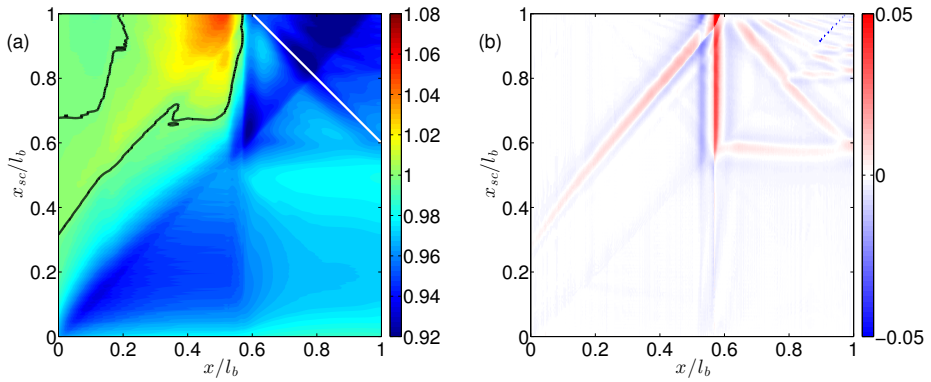

Figure 3.10: Changes in the sea surface height asymmetry characteristics due to a secondary channel. Panel (a): Ratio of the tidal range (T_r) in presence and absence of the secondary channel as a function of x/l_b and x_{sc}/l_b. The black line is the unit contour of T_r. The white line, at which T_r attains a minimum, is called an anti-diagonal. Panel (b): Difference between DFT in presence and absence of the secondary channel (ΔDFT) as a function of x/l_b and x_{sc}/l_b.

ratio to the results shown in figure 3.9(c) reveals that the small region near the open boundary remains ebb dominated, while the largest part of the domain remains flood dominant. The flood dominance is only reversed to an ebb dominance when $x_{sc}/l_b > 0.5$, in a small area around a quarter wavelength of the first overtide seaward of the secondary channel.

The changes induced in DFE (ΔDFE) by the secondary channel are shown in figure 3.11(b) as a function of x/l_b and x_{sc}/l_b. The duration both increases and decreases locally seaward of the secondary channel. When the secondary channel is located at the location of the minimum in tidal range, there is a landward decrease in DFE.

3.3.6 Sensitivity analysis

The tidal range ratio has been computed at the landward end of the main channel for different dimensions of the secondary channel. The position of the secondary channel was fixed halfway along the main channel. The results for the changes in dimension are shown in figure 3.12(a) through (c) for length, width and depth of the secondary channel, respectively. Additionally, the value of the tidal range ratio was computed at the landward end of the main channel for different lengths of the main channel (figure 3.12(d)). Default values are given by the dashed lines.

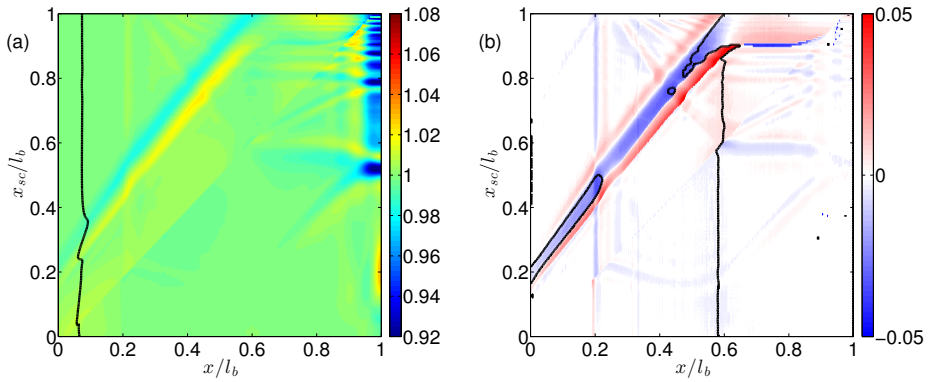

Figure 3.11: Changes in the velocity asymmetry characteristics due to a secondary channel. Panel (a): Ratio of the flood-to-ebb current ratio in presence and absence of the secondary channel as a function of x/l_b and x_{sc}/l_b. The black line is the unit contour of the flood-to-ebb current ratio. Panel (b): Change in DFE due to the secondary channel (ΔDFE) as a function of x and x_{sc} (lower panel). The black line is the contour with value 1/2 of DFE.

Figure 3.12(a) reveals that the optimal length of the secondary channel to reduce tidal range is around 100 km. For this setting, the length of the secondary channel is close to a quarter of the semi-diurnal tidal wavelength in the secondary channel, causing a minimum in tidal range at the vertex point. Consequently, tidal range landward of the vertex point will strongly decrease. Figure 3.12(b) shows that the tidal range ratio decreases linearly with increasing width of the secondary channel, at least up to a width of 1800 m. This indicates that the wider the secondary channel is, the more effective it is. From figure 3.12(c) it appears that for small depths a decrease in tidal range ratio is observed, resulting in smaller tidal ranges for shallower secondary channels. Variations in tidal range ratio due to changing depth are relatively small compared to those due to changes in length and width. The tidal range ratio turns out to reach a constant value for large depths. This occurs because in that case the waves radiating away from the secondary channel are identical to the incoming waves in the secondary channel, regardless of the depth.

Figure 3.12(d) reveals that the tidal range ratio reaches a minimum for a main channel with a length around 44 km. The occurrence of this minimum is consistent with linear theory (Alebregtse *et al.*, 2013), albeit that the length for which the minimum is attained is smaller because of friction and overtides. Long main channels all have a similar tidal range ratio of about 0.98 because the wave that

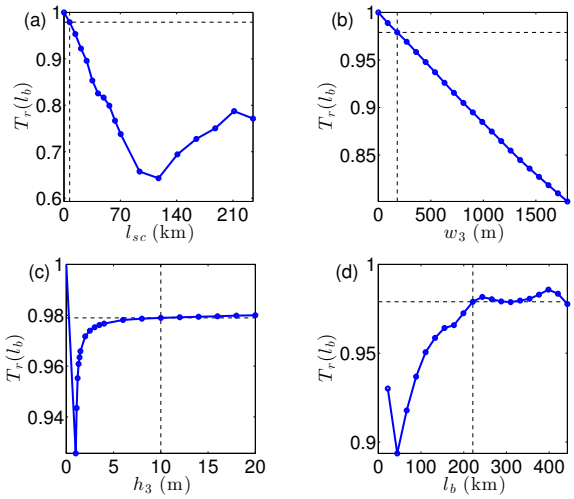

Figure 3.12: Tidal range ratio at the head of the main channel as a function of: (a) length of the secondary channel, (b) width of the secondary channel, (c) depth of the secondary channel and (d) length of the main channel. The secondary channel is located halfway along the main channel. Apart from the variable under consideration all variables are as given in table 3.1.

radiated from the secondary channel towards the landward end and subsequently reflects is damped out by bottom friction before it can re-enter the secondary channel.

3.4 Discussion

3.4.1 Changes in tidal characteristics due to a secondary channel

As explained in the introduction, the first objective of this study is to test the hypothesis that the secondary channel affects the tide by the local production of a distortion, which subsequently propagates through the network. This is based on the work of Alebregtse *et al.* (2013), who identified the linear mechanism causing modification of the M_2 harmonic constituent. They showed that the modification of the M_2 amplitude stems from waves radiating away from the vertex point, which appear due to the secondary channel, besides the undisturbed wave that is unaffected by the secondary channel. The phase of the radiated wave with respect to the undisturbed wave passing the secondary channel is determined by the distance

between the secondary channel and the head of the main channel. This in turn governs the effect of the secondary channel on the tide, resulting in higher (lower) values for the amplitude ratio when the radiated wave is in (out of) phase with the incoming tide.
The results of this study, demonstrating strong similarities between the spatial patterns of the linear and the non-linear amplitude ratios and phase shifts , indicate that the amplification mechanism is also valid for the non-linear model. This is because the attenuation mechanism only depends on the relative phase of the tidal component with respect to the landward end of the main channel and that, as explained by Speer & Aubrey (1985), the overtides are phase locked to the forcing tide when they are internally generated. Thus, the phase of the overtides shows similar phase propagation as the principal tide. This shows that the distortions of the tide induced by the presence of the secondary channel are determined locally but subsequently affect the entire network through the radiated waves.

3.4.2 Tidal range ratio

The minimisation of tidal range is of particular importance for flood-risk management. Therefore, the anti-diagonal observed in the (x, x_{sc})-parameter space for both the tidal range ratio and ΔDFT, shown in figure 3.10, is of particular interest, as it indicates a location where the tidal range has decreased the most.
From the harmonic analysis, shown in figure 3.3(a) and (b), it is deduced that after the M_2 tidal signal, the M_6 tidal signal is the strongest harmonic component present in the main channel. The main source of the M_6 component is the quadratic bottom stress. To eliminate its influence, a model run was performed with a linearised bottom stress. This resulted in minor M_6 tides. Subsequent computation of T_r showed a pattern, which resembled the spatial pattern of $A_{r,2}$. Thus, quadratic bottom stress can be identified as the dominant mechanism causing the spatial non-uniform response in T_r.

3.4.3 Effect of a secondary channel on velocity asymmetry

When comparing the velocity amplitude ratio $V_{r,p}$ with the sea surface height $A_{r,p}$, there appear strong similarities between the patterns landward of the secondary channel. These same similarities are also present between the patterns in the phase shift of sea surface height and velocity. The similarities arise from the fact that the radiated waves are travelling waves, one of which reflects at the closed end of the main channel. As a consequence, any change occurring in the sea surface height amplitude also translates to a similar change in velocity. Thus, the velocity

amplitude ratio follows the sea surface height amplitude ratio.
Adding a secondary channel to the main channel has a limited effect on the flood to ebb velocity ratio. At a distance seaward from the secondary channel equal to a quarter wavelength of the first overtide, this velocity asymmetry is slightly increased followed by a decrease in the asymmetry. Towards the landward end of the main channel the flood to ebb ratio is strongly reduced. However, velocities are close to zero there, due to the closed boundary condition and thus the velocity ratios are of limited importance there.
The DFE is also changed around a quarter wavelength of the first overtide seaward of the secondary channel. The decrease in DFE locally changes the transition from going faster from ebb to flood to faster transitions from flood to ebb. Moreover, for positions of the secondary channel near the closed end of the main channel, an increase in DFE is observed. However, the change is insufficient to turn the sign of the duration asymmetry in velocity.
Asymmetry of the velocity curve is an important indicator for the direction of the net sediment transport. For net bedload transport the flood velocity to ebb velocity ratio controls the direction of net transport due to overtides (Aubrey, 1986), whereas for fine sediment the asymmetry in transition duration from flood to ebb and vice versa is also relevant (Groen, 1967). Changes in the asymmetries can thus be used to identify changes in net sediment transport, especially whether the net sediment transport will increase or decrease.
Net bedload transport appears to be only mildly affected by the presence of a secondary channel. The changes occurring in the flood-to-ebb velocity ratio due to the secondary channel are not such that they reverse the direction of the peak current. Only in a small region at a distance of about a quarter M_4 tidal wavelength from the secondary channel, for secondary channels located at $x_{sc}/l_b > 0.5$, the velocity becomes ebb-dominant. For the net transport of suspended sediments a secondary channel is more important than for net bedload transport because the changes occurring in the transition duration are quite substantial. If DFE> 0.5 (hence a shorter duration of slack after flood) less sediment will settle down, resulting in higher suspended sediment concentrations in the successive tidal period and leading to net sediment transport in that direction. Since the secondary channel can change DFE from more to less than half the tidal cycle, the direction of net suspended sediment transport could potentially change direction.

3.4.4 Applications and limitations

The non-linear model described in this study provides an extension of the linear model presented by Alebregtse *et al.* (2013). It has shown additional insight in amplification mechanisms in tidal networks consisting of a main channel and a

secondary channel. Moreover, it contains a modification with respect to other tidal network models, as most one-dimensional network models demand continuity of sea surface height at vertex points instead of dynamical pressure, (cf. Bolla-Pittaluga *et al.*, 2003; Manoj *et al.*, 2009). However, velocity differences also induce small pressure differences over strong changes in cross-sectional area (Dronkers, 1964). Moreover, the model is readily extendable to include width and depth convergence, which can broaden its applicability.
Results from simple models can only be interpreted as first order responses of systems. In particular, the changes in velocity asymmetry have been used to yield a first estimate of changes in net sediment transport. Clearly, when considering sediment transport it is eventually important to solve the full advection-diffusion equation governing the erosion, deposition and transport of sediment. As yet, this is not possible for one-dimensional network models, due to unknown conditions at the vertex point for sediment distribution in bidirectional flow. Such conditions have only been empirically described for unidirectional flow, e.g. by Wang *et al.* (1995). Thus, for case studies, the use of complex numerical models is obviously of crucial importance.

3.5 Conclusions

Changes in vertical and horizontal tidal characteristics that occur in a main channel due to the presence of a secondary channel were investigated. This was done by using a one-dimensional tidal network model that solves the non-linear shallow water equations using the method of characteristics. Results obtained for a main channel without secondary channel were compared with those calculated for a main channel with a secondary channel at an arbitrary position along the main channel to assess the effect of a secondary channel on tidal characteristics. Both systems were forced with an identical incoming wave.
Both the amplitudes and phases of harmonic components of sea surface height and velocity, as well as four asymmetry parameters (tidal range, duration of the falling tide, flood-to-ebb ratio, and duration between maximum flood and maximum ebb) were computed and analysed. Ratios between values in the presence and absence of the secondary channel were calculated for the amplitudes of the harmonic components, the tidal range, and the flood-to-ebb ratio. Regarding the phases of the tidal harmonics and durations, a difference was computed between their values obtained for a configuration with and without a secondary channel.
The results for the harmonic components of the vertical tide from the non-linear model followed the amplification mechanism identified by Alebregtse *et al.* (2013). These results confirmed the hypothesis that the secondary channel locally produces a distortion, which radiates away from the secondary channel and thereby

influences the tide in the remainder of the network as well. Additionally, the use of a non-linear model added new insights in the response of the asymmetry characteristics of the tidal wave. Alebregtse *et al.* (2013) found a spatially uniform structure of the amplitude ratio of the sea surface height in the region landward of the vertex point. However, the tidal range ratio had a much more spatial non-uniform character than was obtained with the linear model. This results from the spatially non-uniform friction caused by the quadratic bottom stress formulation. The latter was demonstrated by considering the same model with a linearised stress formulation, resulting in the reduction of the spatial patterns landward area from the vertex point. Therefore, for management purposes it is also important to consider local effects of non-linear processes on the response of the sea surface height and velocity to the presence of the secondary channel.
The secondary channel has been shown to have a limited effect on the flood to ebb velocity ratio and thus only mildly influences the net bedload transport of sediment. The change in ratio is predominantly insufficient to change the direction of net sediment transport. This result might, however, depend on the dimensions of the secondary channel. Net transport of suspended sediment is more sensitive to the location of the secondary channel, as it strongly influences the duration between maximum flood and maximum ebb velocity (DFE). Most changes in DFE are confined to an area approximately a quarter of the M_4 tidal wavelength seaward of the secondary channel. If the secondary channel is located near the closed end of the main channel a large area of increased flood to ebb transition duration is observed. This potentially leads to reversal of the direction of net suspended load transport.

3.A Method of characteristics

First, equations (3.1) and (3.2) are written in tensor notation

$$A_{m,n}\frac{\partial \psi_n}{\partial t} + a_{m,n}\frac{\partial \psi_n}{\partial x} + b_m = 0 \ , \tag{3.12}$$

where $\psi_n = (u, \eta)^{\mathrm{T}}$ ($\cdot^{\mathrm{T}}$ indicates the transpose), $A_{m,n} = \delta_{m,n}$ ($\delta_{m,n}$ is the Kronecker delta function),

$$a_{m,n} = \begin{pmatrix} u & g \\ (h+\eta) & u \end{pmatrix},$$

and

$$b_m = \left(c_d \frac{|u|u}{h+\eta}, \ \frac{u(h+\eta)}{w}\frac{dw}{dx} + u\frac{dh}{dx} \right)^{\mathrm{T}} \ .$$

Now, two linear combinations are sought which obey a characteristic velocity, that is

$$l_m^{(k)}\left[A_{m,n}\frac{\partial \psi_n}{\partial t} + a_{m,n}\frac{\partial \psi_n}{\partial x} \right] + l_m^{(k)} b_m = 0 \ , \tag{3.13}$$

such that

$$l_m^{(k)} a_{m,n} = l_n c^{(k)} \ , \tag{3.14}$$

where $c^{(k)}$ is the characteristic velocity ($k = +$ or $k = -$). This velocity follows from

$$|a_{m,n} - c^{(k)}\delta_{m,n}| = 0 \ , \tag{3.15}$$

where $|\cdot|$ denotes the determinant. This yields the characteristic velocity as

$$c^{(k)} = u \pm \sqrt{g(h+\eta)} \ , \tag{3.16}$$

as is given in Eq (3.5).
Substituting Eq (3.16) into Eq (3.14), it is found that

$$l_m^{(k)} = (1, \ \pm\sqrt{\frac{g}{(h+\eta)}}) \ . \tag{3.17}$$

Combining Eqs (3.13) and (3.14) yields

$$\begin{aligned} &l_m^{(k)}\left[A_{m,n}\frac{\partial \psi_n}{\partial t} + c^{(k)}\frac{\partial \psi_n}{\partial x} \right] + l_m^{(k)} b_m = 0 && \text{on } \frac{dx}{dt} = c^{(k)} \ , \\ &l_m^{(k)}\frac{d\psi_m}{dt} + l_m^{(k)} b_m = 0 && \text{on } \frac{dx}{dt} = c^{(k)} \ . \end{aligned} \tag{3.18}$$

Now, a substitution is sought to replace $l_m \frac{d\psi_m}{dt}$ with a total derivative of a single variable, called the Riemann invariant. The Riemann invariants are determined by demanding

$$l_m^{(k)} = \frac{\partial r^{(k)}}{\partial \psi_m} \ , \tag{3.19}$$

which yields

$$r^{(k)} = u \pm 2\sqrt{g(h+\eta)} \ , \tag{3.20}$$

giving Eq (3.4).
From Eq (3.18), it follows that

$$\begin{aligned} f^{(k)} = l_m^{(k)} b_m = c_d \frac{|u|u}{h+\eta} + \\ \pm \sqrt{\frac{g}{(h+\eta)}} \Big(\frac{u(h+\eta)}{w} \frac{dw}{dx} + u \frac{dh}{dx} \Big) \ , \end{aligned} \tag{3.21}$$

which is Eq (3.6).
Thus, Eq (3.18) becomes with the use of Eqs (3.19) and (3.21)

$$\frac{dr^{(k)}}{dt} + f^{(k)}(x,t,u,\eta) = 0 \qquad \text{on } \frac{dx}{dt} = c^{(k)} \ , \tag{3.22}$$

which is Eq (3.3).

Chapter 4

Effect of river discharge and geometry on tides and net water transport in an estuarine network, an idealized model applied to the Yangtze Estuary

4.1 Introduction

Many estuaries around the world exhibit bifurcation characteristics, with river water being distributed over the different channels and eventually ending up in the ocean (e.g. the Yangtze Estuary, figure 4.1). This distribution is affected by the propagation of the tide through the estuarine network. First, additional residual transport due to nonlinear tidal rectification is generated (cf. Longuet-Higgins, 1953; Ianniello, 1977), hence the combination of river induced transport and tidal residual water transport determines the net water transport through the network (Buschman *et al.*, 2010). Second, net water transport also has an effect on the tidal propagation and river transport distribution through subtidal friction, implying a feedback (Buschman *et al.*, 2009). Knowledge of the net water transport through an estuarine network is important for e.g. computing salinity intrusion, flushing of pollutants and sediment transport.

Tidal propagation in estuarine networks has been investigated by e.g. Lorentz (1926); Hill & Souza (2006); Zhang *et al.* (2012); Alebregtse *et al.* (2013); Alebregtse & de Swart (2014) and Cai *et al.* (2014). These studies focused on tidal

This chapter is based on:
Alebregtse, N. C., & de Swart, H. E. 2015 Effect of river discharge and geometry on tides and net water transport in an estuarine network, an idealized model applied to the Yangtze Estuary. *Submitted to Continental Shelf Research*.

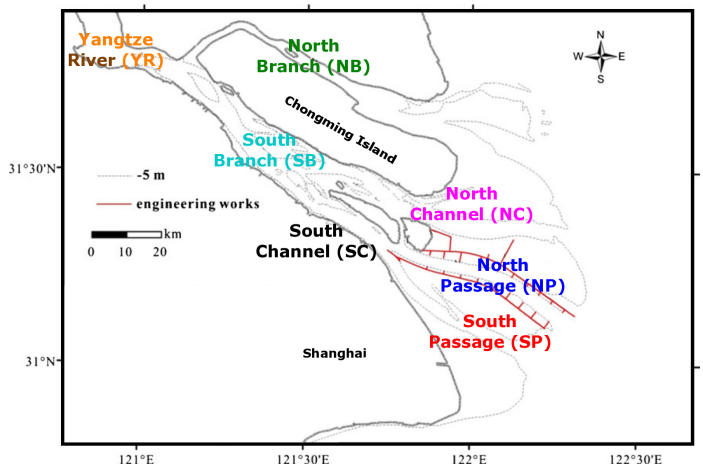

Figure 4.1: Map of the Yangtze estuary from Jiang *et al.* (2013). Channels are from North to South the Yangtze River (YR), North Branch (NB), South Branch (SB), North Channel (NC), South Channel (SC), North Passage (NP), and South Passage (SP). The training walls, groins and jetties from the Deepwater Navigation Channel (DNC), a large-scale human intervention, are indicated in red. Figure after Jiang *et al.* (2013).

properties, such as tidal sea surface amplitude, and phase propagation, and not on net water transport. Net water transport in networks due to different forcings was investigated a.o. by Ridderinkhof (1988); Buschman *et al.* (2010); Li *et al.* (2010); Sassi *et al.* (2011) and Zhang *et al.* (2011). Ridderinkhof (1988) considered a tidal network consisting of two channels and did not account for river discharge or the effect of residual currents on tidal damping. He found that a net water transport occurs towards the deeper and/or narrower channel for identical tidal forcing on both channels. Buschman *et al.* (2010) used a numerical model to investigate the division of net water transport at a tidally influenced bifurcation. They found that the residual transport due to nonlinear tidal rectification increases net water transport in the channel with the highest river transport, except when the bottom friction parameter in one of the channels was changed. Sassi *et al.* (2011) found that the tidal influence also decreases the asymmetric division of river water, due to so-called differential water level setup. The latter occurs because in a single channel the residual set-up increases with river transport due to increased subtidal friction. Since at the bifurcation the dynamic pressure in both channels has to be equal, the water mass associated with the excess pressure associated with this set-up is discharged through the channel with the smaller transport. Finally,

Li *et al.* (2010) and Zhang *et al.* (2011) determined the water diversion ratio in the Yangtze Estuary, which is the amount of net water transport through a branch, relative to the upstream net water transport. Li *et al.* (2010) applied a numerical model for this, and found that increasing river discharge leads to a more equal distribution of net water transport at all bifurcations in the Yangtze Estuary. Zhang *et al.* (2011) used data on tidal and salinity characteristics to infer residual flows through different channels of the Yangtze Estuary. They found a decrease in net water transport in the North Passage due to the construction of a navigation channel. Neither of these studies isolated the role of residual currents generated by the nonlinear interactions.

The results of Buschman *et al.* (2010) and Sassi *et al.* (2011) show the importance of nonlinear tidal dynamics in determining the net water transport in tidal networks. However, it is unclear which nonlinear processes (e.g. generation of overtides by advection, depth dependent friction, and Stokes transport) are most important in producing tidally induced residual transport. Therefore, this manuscript will extend the existing literature in three ways. First, by investigating the propagation of tides, which are subject to river-tide interactions, through an arbitrary estuarine network. Second, by computing residual and quarter diurnal currents that result from the nonlinear terms in the equations of motion in an estuarine network using a semi-analytical model. Third, tidal damping is coupled to both the tidal and the residual velocity. The semi-analytical model is obtained by applying a harmonic truncation to the water motion, and a subsequent scaling analysis of the dominant processes. Quadratic bottom stress is linearized with the use of Chebyshev polynomials, as described by Godin (1991, 1999). The analytical nature of the model allows for an identification of the dominant processes in determining the net water transport.

The model will be used to investigate tides and net water transport in the Yangtze Estuary, China, as a case study. The Yangtze Estuary is of high interest, because it is a typical estuarine network, and it is characterized by a strong seasonal cycle in river discharge. The latter exerts a marked influence on the tides through enhanced friction at higher discharges, as reported by Guo *et al.* (2015). Furthermore, the estuary has been subject to multiple anthropogenic changes to its geometry in the past decade. One change was due to the construction of the Deepwater Navigation Channel (DNC), which consists of two training walls and a deepening of the main fairway in one of the channels of the estuary (figure 4.1). These constructions strongly affected the hydrodynamics (Jiang *et al.*, 2012, 2013). Model results obtained for the wet and dry season will be compared with each other to identify the dominant processes governing net water transport in different seasons. Furthermore, model results for geometries resembling Yangtze Estuary in its current and historic state (i.e. post and pre-DNC) are compared to identify how these processes change due to anthropogenic influences. Differences between the model

results for the various cases will be investigated and explained, with a focus on changes in net water transport.
The manuscript is structured as follows. Section 4.2 presents the model equations and the characteristics of the study area. Section 4.3 presents the results, while section 4.4 analyses which processes govern the net water transport through an estuarine network and discusses model limitations. Section 4.5 contains the main conclusions.

4.2 Materials and methods

4.2.1 Model

Domain

Estuarine networks comprise multiple channels that are connected to each other, in which water motion mainly results from the joint action of river discharge and tides. A specific example of an estuarine network configuration, that can be seen as a highly schematized representation of the Yangtze Estuary, is shown in figure 4.2. The channels each have an arbitrary length ($l_{b,j}$), a constant depth (h_j) and an exponentially varying width (b_j) in the along-channel direction as

$$b_j(x) = b_{o,j} e^{(x-l_{o,j})/l_{c,j}} \ , \tag{4.1}$$

where j is the channel index, x is the along-channel coordinate increasing seaward, $b_{o,j}$ is the width at the end point, $l_{o,j}$ is the position of the end point of the channel, and $l_{c,j}$ is the exponential convergence length scale. The channels exhibit no lateral variability in depth. The begin- and endpoint of each channel are not necessarily located at either a boundary connected to the sea, or a boundary connected to a river, but can also be located at a bifurcation point where several channels join.

Hydrodynamics

In this study, hydrodynamics in tidal networks are described by the cross-sectionally averaged shallow water equations

$$\frac{\partial u}{\partial t} + u\frac{\partial u}{\partial x} = -g\frac{\partial \eta}{\partial x} - C_d\frac{|u|u}{h+\eta} \ , \tag{4.2a}$$

$$b\frac{\partial \eta}{\partial t} + \frac{\partial}{\partial x}\Big(b(h+\eta)u\Big) = 0 \ , \tag{4.2b}$$

where u is the along-channel cross-sectionally averaged velocity. Time is indicated by t, free surface elevation (with respect to the undisturbed water level) by η and gravitational acceleration by g. Furthermore, C_d is the drag coefficient. Note that Eqns. (4.2) are different for each channel, as the depth, width, and drag coefficient

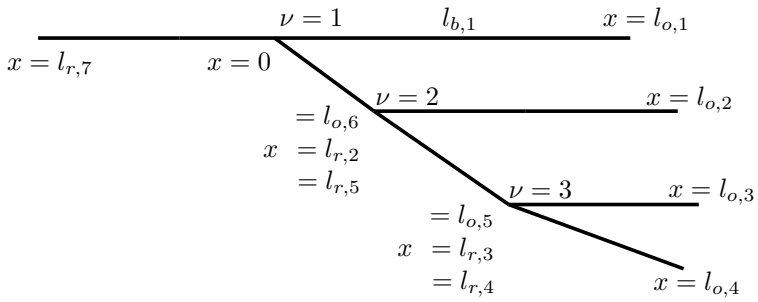

Figure 4.2: A scheme of a general estuarine network. The along-channel coordinate, x, increases downstream (towards sea). Each channel has a length $l_{b,j}$. The different $l_{o,j}$ denote the channel boundaries pointing towards the ocean, while the $l_{r,j}$ denote the boundaries pointing towards the river.

vary between channels. However, a channel index has been omitted to increase legibility. This will be done for most of the following equations as well, so unless it is specified otherwise a channel index is implied.
Boundary conditions are prescribed at the begin- and endpoint of each channel. All channels containing a boundary connected to the sea are forced by a tidal sea surface elevation, while channels with a boundary at the landward side are forced with a river discharge. The remainder of the boundary conditions consists of matching conditions at the bifurcation points, viz. continuity of dynamic pressure and conservation of mass. The boundary conditions for a network thus read

$$\eta_j = N_j \cos(\sigma t - \phi_j) \ , \qquad \text{at } x = l_{o,j} \ , \ j \in O \ , \tag{4.3a}$$

$$b_j(h_j + \eta_j)u_j = Q^{\mathrm{R}}_{0,j} \ , \qquad \text{at } x = l_{r,j} \ , \ j \in R \ , \tag{4.3b}$$

$$g\eta_j + \frac{\mu}{2}u_j^2 = g\eta_k + \frac{\mu}{2}u_k^2 \ , \qquad \forall j,k \in J_\nu \ , \ \nu \in V \ , \tag{4.3c}$$

$$\sum_{j \in J_\nu} b_j(h_j + \eta_j)u_j = 0 \ . \tag{4.3d}$$

Here, O denotes the set of channel indices connected to the sea at $x = l_{o,j}$ (for example, in Fig. 4.2 this means $O = \{1, 2, 3, 4\}$). At each channel, an amplitude (N_j) and phase (ϕ_j) of the semi-diurnal tide are prescribed. Further, σ is the tidal frequency $2\pi/T_p$, with T_p the tidal period. Moreover, R denotes the set of channel indices connected to a river at $x = l_{r,j} = l_{o,j} - l_{b,j}$, where each river has a prescribed discharge of $Q_{0,j}$ (in Fig. 4.2, $R = \{7\}$). For the matching conditions, J_ν is the set of channel indices that join at the bifurcation point ν under consideration, with V the set of all bifurcation points. For example, in Fig. 4.2 the set $V = \{1, 2, 3\}$ contains three bifurcation points, with $J_1 = \{1, 6, 7\}$, $J_2 = \{2, 5, 6\}$, and $J_3 = \{3, 4, 5\}$. Next, μ (with a value between 0 and 1) is a

head loss coefficient (van de Kreeke, 1988). Head loss accounts for frictional effects at strong cross-sectional jumps, e.g. due to eddy shedding. No head loss occurs if $\mu = 1$. Finally, Eqn. (4.3d) denotes conservation of mass. In this equation, the direction of the velocity towards or away from the bifurcation point has to be taken into account.

Net water transport

The net water transport is defined as the average of the volume transport over a tidal cycle, i.e.

$$\overline{Q} = \overline{b(h+\eta)u} = bh\overline{u} + b\overline{\eta u} \ , \tag{4.4}$$

where the overlines denote averaging over a tidal cycle. The first term on the right hand side contains the river velocity and residual velocities due to nonlinear tidal rectification, while the second term denotes the Stokes transport, which arises from the correlation between sea surface elevation and velocity.
Analysis of the net water transport is carried out by considering the water diversion ratio between two channels that are connected by a bifurcation. This ratio is the water transport through one of these channels, divided by the sum of the water transport in both channels. The net water diversion ratio (nWDR) is defined as this ratio applied for the net water transport, or

$$\text{nWDR} = \frac{\overline{Q}_j}{\overline{Q}_j + \overline{Q}_k} \ , \tag{4.5}$$

with j and k two downstream channels connected to a bifurcation point. The nWDR measures the fraction of upstream net water transport that is discharged through one of the branches at a bifurcation. For any bifurcation, the sum of the nWDR of the downstream channels is 1. For example, in Fig. 4.2 at bifurcation point $\nu = 1$, $\text{nWDR} = \overline{Q}_1/(\overline{Q}_1 + \overline{Q}_6)$.
Since the net water transport is difficult to measure, as it is the difference between two large numbers which have a large uncertainty (viz. the tidally integrated ebb and flood transport), research is often carried out on the ebb water diversion ratio, eWDR. Moreover, ebb water transport is important for the transport of sediments and pollutants. The ebb water diversion ratio is computed as the water diversion ratio applied to the tidally integrated volume of all seaward directed transport, i.e.

$$\text{eWDR} = \frac{\overline{Q}_{j,\text{ebb}}}{\overline{Q}_{j,\text{ebb}} + \overline{Q}_{k,\text{ebb}}} \ , \qquad \text{with } \overline{Q}_{j,\text{ebb}} = \overline{Q_j \mathcal{H}(Q_j)} \ . \tag{4.6}$$

In this expression, $\mathcal{H}$ is the Heaviside function, which equals 1 (0) for positive (negative) arguments, and Q_j is the total water transport defined within Eqn. (4.4).

Construction of approximate solutions

In this study, approximate solutions of Eqns. (4.2a) and (4.2b) are constructed. This will be done by using a twofold expansion. The first expansion consists of a harmonic truncation, while the second is a perturbation expansion. The harmonic truncation retains the residual, semi-diurnal, and quarter diurnal components, as these are typically the largest in estuarine networks. Thus, any system variable in any channel is first decomposed using the harmonic truncation as

$$\chi = \chi_0 + \chi_1 + \chi_2 \ , \tag{4.7}$$

with $\chi = \{u, \eta\}$. Here, the subscript indicates the harmonic component, where 0 represents the residual component, 1 the semi-diurnal lunar tidal component, and 2 the quarter diurnal component. The expression for each harmonic component is

$$\begin{aligned} u_n &= \mathcal{R}\left(\mathcal{U}_n(x)\ e^{-in\sigma t}\right) \ , \\ \eta_n &= \mathcal{R}\left(\mathcal{N}_n(x)\ e^{-in\sigma t}\right) \ , \end{aligned} \tag{4.8}$$

with n the harmonic component. Further, $\mathcal{R}$ denotes taking the real part of $\mathcal{U}_n$ and $\mathcal{N}_n$, the (complex) amplitudes that describe the spatial structure of velocity and free surface elevation, respectively. The perturbation expansion involves a small parameter, which is determined by the dominant hydrodynamic processes. A scaling of Eqns. (4.2a) and (4.2b) yields the ratio of the amplitude of the free surface elevation to the total depth ($\varepsilon \equiv N_1/h_1$) as a small parameter (for a derivation see appendix 4.A). The perturbation expansion subsequently splits each harmonic component into

$$\chi_n = \chi_n^{(0)} + \chi_n^{(1)} + ... \ , \tag{4.9}$$

where $\chi_n^{(0)}$ are the leading order solutions, which result from the external forcing (river discharge at the landward boundary, tidal forcing at the seaward boundary). Next, $\chi_n^{(1)}$ are the first order solutions, which result from nonlinear interactions between the leading order variables. The ratio of the magnitudes of $\chi_n^{(1)}$ and $\chi_n^{(0)}$ is of order ε. For convenience of notation, if either the subscript or superscript is omitted, the sum of all harmonics or of the retained contributions in the perturbation expansion is considered, respectively, i.e.

$$\chi^{(1)} = \chi_0^{(1)} + \chi_1^{(1)} + \chi_2^{(1)} \ , \text{ and} \qquad\qquad \chi_0 = \chi_0^{(0)} + \chi_0^{(1)} \ .$$

Net water transport

Applying the harmonic truncation to the net water transport, it evaluates as

$$Q_0 = bh\mathcal{U}_0 + b\mathcal{N}_0\mathcal{U}_0 + \frac{b}{4}(\mathcal{N}_1\mathcal{U}_1^\dagger + \mathcal{N}_1^\dagger\mathcal{U}_1) + \frac{b}{4}(\mathcal{N}_2\mathcal{U}_2^\dagger + \mathcal{N}_2^\dagger\mathcal{U}_2) \ ,$$

where the † denotes taking the complex conjugate. Note that the overline from Eqn. (4.4) has been replaced with the subscript 0 as these have identical meanings. Taking the perturbation expansion of the above expression yields for the leading and first order, respectively (see appendix 4.A),

$$Q_0^{(0)} = \underbrace{bh\mathcal{U}_0^{(0)}}_{1} \,, \tag{4.10a}$$

$$Q_0^{(1)} = \underbrace{bh\mathcal{U}_0^{(1)}}_{2} + \underbrace{\frac{b}{4}(\mathcal{N}_1^{(0)}\mathcal{U}_1^{(0)\dagger} + \mathcal{N}_1^{(0)\dagger}\mathcal{U}_1^{(0)})}_{3} + \underbrace{b\mathcal{N}_0^{(0)}\mathcal{U}_0^{(0)}}_{4} \,. \tag{4.10b}$$

Here, term 1 in Eqn. (4.10a) denotes the river induced transport, while in Eqn (4.10b) term 2 denotes the residual transport due to the tidally rectified Eulerian current, while term 3 and 4 are the correlation between sea surface height and velocity of the (external) semi-diurnal tide (the so-called Stokes transport) and river, respectively. The sum of the latter three contributions is the residual transport due to nonlinear interactions.

Friction

To allow for (semi-)analytical solutions, a harmonic truncation also has to be applied to the quadratic bottom stress, i.e.

$$\frac{\tau_b}{\rho} = C_d|u|u \approx \mathcal{T}_0 + \mathcal{T}_1 + \mathcal{T}_2 \,,$$

with τ_b the bottom stress, ρ the density of water, C_d a drag coefficient, and $\mathcal{T}_n$ the n^{th} harmonic component. Applying a Chebyshev expansion up to third order approximates the quadratic bottom stress with a cubic polynomial expression. The harmonic truncation of the velocity is substituted in the latter to investigate the effective friction of the different harmonic components. The result is (for a derivation see appendix 4.A, and Godin, 1991, 1999)

$$\begin{aligned}
\mathcal{T}_0 &= \underline{\lambda}_0\mathcal{U}_0 \;+\; \underline{\lambda}_{c0}\mathcal{R}(\mathcal{U}_2\mathcal{U}_1^{\dagger 2}) \,, \\
\mathcal{T}_1 &= \underline{\lambda}_1\mathcal{R}(\mathcal{U}_1 e^{-i\sigma t}) \;+\; \underline{\lambda}_{c1}\mathcal{R}(\mathcal{U}_0\mathcal{U}_2\mathcal{U}_1^{\dagger} e^{-i\sigma t}) \,, \\
\mathcal{T}_2 &= \underline{\lambda}_2\mathcal{R}(\mathcal{U}_2 e^{-2i\sigma t}) \;+\; \underline{\lambda}_{c2}\mathcal{R}(\mathcal{U}_0\mathcal{U}_1^{2} e^{-2i\sigma t}) \,.
\end{aligned} \tag{4.11}$$

The $\underline{\lambda}_m$ are (space dependent) effective friction coefficients of the corresponding harmonics for $m = \{0,\ 1,\ 2\}$. Additionally, for $m = \{c0,\ c1,\ c2\}$ the $\underline{\lambda}_m$ denote (space dependent) coupling coefficients of the harmonic with other harmonic

components. The expressions for the friction and coupling coefficients read

$$\begin{aligned}
\underline{\lambda}_0 &= \frac{16}{15\pi} C_d U \left[1 + 2 \left(\left(\frac{|\mathcal{U}_0^{(0)}|}{U} \right)^2 + \frac{3}{2} \left(\frac{|\mathcal{U}_1^{(0)}|}{U} \right)^2 \right) \right] , \\
\underline{\lambda}_1 &= \frac{16}{15\pi} C_d U \left[1 + 2 \left(3 \left(\frac{|\mathcal{U}_0^{(0)}|}{U} \right)^2 + \frac{3}{4} \left(\frac{|\mathcal{U}_1^{(0)}|}{U} \right)^2 \right) \right] , \\
\underline{\lambda}_2 &= \frac{16}{15\pi} C_d U \left[1 + 2 \left(3 \left(\frac{|\mathcal{U}_0^{(0)}|}{U} \right)^2 + \frac{3}{2} \left(\frac{|\mathcal{U}_1^{(0)}|}{U} \right)^2 \right) \right] , \\
\underline{\lambda}_{c0} &= \frac{8 C_d}{5\pi U} , \qquad \underline{\lambda}_{c1} = \frac{32 C_d}{5\pi U} , \qquad \underline{\lambda}_{c2} = \frac{16 C_d}{5\pi U} .
\end{aligned} \tag{4.12}$$

In these expressions, $U = |\mathcal{U}_0| + |\mathcal{U}_1| + |\mathcal{U}_2|$ is a space-dependent velocity scale. Results for the space dependent friction and coupling coefficients are averaged over each channel, i.e.

$$\lambda_m \equiv \frac{1}{l_b} \int_{l_r}^{l_o} \underline{\lambda}_m \, dx \, . \tag{4.13}$$

Values for λ_0, λ_1 and λ_2 are obtained through an iterative procedure. An initial guess is made for the values of the friction coefficients. Subsequently, all solutions are calculated for this friction value. With the obtained velocity solutions, the friction coefficients are computed again. These new values are compared to the input values. If the difference is too large, the new values are used to compute new solutions. This process is repeated until changes in the friction coefficients are below a certain threshold value.

Solutions

Leading order solution

Applying both the harmonic truncation and the truncated perturbation expansion to Eqns. (4.2a) and (4.2b) yields (see appendix 4.A for a derivation)

$$\mathcal{U}_n^{(0)} = \frac{-gh}{\lambda_n - in\sigma h} \frac{d\mathcal{N}_n^{(0)}}{dx} , \tag{4.14a}$$

$$-in\sigma \mathcal{N}_n^{(0)} = -\frac{1}{b} \frac{d}{dx} \left(bh \mathcal{U}_n^{(0)} \right) . \tag{4.14b}$$

These equations give a relation between the leading order velocity and sea surface elevation gradient, obtained from Eqn. (4.2a), while a relation between sea surface elevation and the divergence of the volume transport is constructed from

Eqn. (4.2b). The system of equations, Eqn. (4.14), allows solutions for the leading order free surface elevation as

$$\mathcal{N}_n^{(0)} = e^{\gamma x/2}\left(A_n^{(0)}\exp(i\kappa_n x) + B_n^{(0)}\exp(-i\kappa_n x)\right) \ . \tag{4.15}$$

Here, γ is the inverse convergence length, while $\kappa_{\pm n}$ is the wave number, including the effect of channel convergence and wave propagation direction. They are defined as

$$\gamma = \frac{-1}{l_c} \ ,$$
$$\kappa_n = \sqrt{\mu_n^2 - \frac{1}{4}\gamma^2} \ ,$$

where μ_n is the wave number without accounting for channel convergence, which reads

$$\mu_n^2 = n\left(\frac{n\sigma^2 h + i\sigma\lambda_n}{gh^2}\right) \ .$$

Lastly, $A_n^{(0)}$ and $B_n^{(0)}$ are constants that are determined by the boundary conditions, which for the leading order dynamics read

$$\left.\begin{aligned} \mathcal{N}_{0,j}^{(0)} &= 0 \ , \\ \mathcal{N}_{1,j}^{(0)} &= N_j e^{i\phi_j} \ , \end{aligned}\right\} \quad \text{at } x = l_{o,j} \ , \ j \in O \ , \tag{4.16a}$$

$$\left.\begin{aligned} b_j h_j \mathcal{U}_{0,j}^{(0)} &= Q_{0,j}^{\mathrm{R}} \ , \\ \mathcal{U}_{1,j}^{(0)} &= 0 \ , \end{aligned}\right\} \quad \text{at } x = l_{r,j} \ , \ j \in R \ , \tag{4.16b}$$

$$\left.\begin{aligned} \mathcal{N}_{n,j}^{(0)} &= \mathcal{N}_{n,k}^{(0)} \ , \\ \sum_{j\in J_\nu} b_j h_j \mathcal{U}_{n,j}^{(0)} &= 0 \ , \end{aligned}\right\} \quad \forall j,k \in J_\nu \ , \ \nu \in V \ . \tag{4.16c}$$

Here, Eqns. (4.16a) represent the conditions at the ocean boundaries, while Eqns. (4.16b) represent the conditions at the landward boundaries. Eqns. (4.16c) denote continuity of sea surface elevation, and conservation of mass at the bifurcation points.

For $n = 0$ (the residual harmonic), Eqn. (4.15) simplifies to

$$\mathcal{N}_0^{(0)} = A_0^{(0)} + B_0^{(0)}\exp(\gamma x) \ ,$$

showing that river transport induces a set-up towards the end of a channel. In nature, this set-up is partly provided by a bottom slope. Therefore, the set-up induced by the river is corrected with the set-up computed for a reference river discharge, viz. the annual average value for the river under consideration. In this way, a net set-up occurs for above average discharge and a net set-down occurs for below average discharge.

First order solution

Introducing the expansions from section 4.2.1 to Eqn. (4.2a) and (4.2b) yields the following differential equations for the first order system variables:

$$\mathcal{U}_n^{(1)} = -\frac{gh}{\lambda_n - in\sigma h}\frac{d\mathcal{N}_n^{(1)}}{dx} + \frac{h\mathcal{F}_n}{\lambda_n - in\sigma h} \ , \tag{4.17a}$$

$$-in\sigma\mathcal{N}_n^{(1)} = -\frac{1}{b}\frac{d}{dx}\Big(b(h\mathcal{U}_n^{(1)} + \mathcal{S}_n)\Big) \ . \tag{4.17b}$$

where $\mathcal{F}_n$ contains the nonlinear terms from Eqn. (4.2a), while S_n contains the nonlinear terms from Eqn. (4.2b). For the residual harmonic component, these read

$$\begin{aligned}\mathcal{F}_0 = &\underbrace{-\frac{1}{2}\frac{d}{dx}\Big(\mathcal{U}_0^{(0)2} + \frac{1}{2}\mathcal{U}_1^{(0)}\mathcal{U}_1^{(0)\dagger}\Big)}_{1} + \underbrace{\frac{\lambda_1}{4h^2}\Big(\mathcal{N}_1^{(0)}\mathcal{U}_1^{(0)\dagger} + \mathcal{N}_1^{(0)\dagger}\mathcal{U}_1^{(0)}\Big)}_{2} + \\ &+ \underbrace{\frac{\lambda_0}{h^2}\mathcal{N}_0^{(0)}\mathcal{U}_0^{(0)} + \frac{\lambda_{c0}}{2h}\Big(\mathcal{U}_2^{(1)}\mathcal{U}_1^{(0)\dagger 2} + \mathcal{U}_2^{(1)\dagger}\mathcal{U}_1^{(0)2}\Big)}_{3} \ ,\end{aligned} \tag{4.18}$$

$$\mathcal{S}_0 = \underbrace{\mathcal{N}_0^{(0)}\mathcal{U}_0^{(0)} + \frac{1}{4}\Big(\mathcal{N}_1^{(0)}\mathcal{U}_1^{(0)\dagger} + \mathcal{N}_1^{(0)\dagger}\mathcal{U}_1^{(0)}\Big)}_{4} \ . \tag{4.19}$$

Expressions for $\mathcal{F}_1$, $\mathcal{F}_2$, $\mathcal{S}_1$, and $\mathcal{S}_2$ are given in appendix 4.A. In Eqn. (4.18), term 1 denotes horizontal advection of momentum. Term 2 results from the depth dependence of friction. Term 3 in Eqn. (4.18) shows the coupling between the residual and quarter diurnal currents due to the quadratic bottom stress. Finally, term 4 in Eqn. (4.19) denotes Stokes transport, i.e. the net water volume transport per unit of width that is induced by the tidal wave.
Substituting Eqn. (4.17a) into Eqn. (4.17b) yields a differential equation for the free surface elevation, which reads

$$\frac{d^2\mathcal{N}_n^{(1)}}{dx^2} - \gamma\frac{d\mathcal{N}_n^{(1)}}{dx} + \mu_n^2 N = \frac{1}{b}\frac{d}{dx}\left[b\Big(\frac{\lambda_n - in\sigma h}{gh^2}\mathcal{S}_n + \frac{\mathcal{F}_n}{g}\Big)\right] \ . \tag{4.20}$$

The solutions of Eqn. (4.20) are of the form

$$\mathcal{N}_n^{(1)}(x) = e^{\gamma x/2}\left(A_n^{(1)}\exp(i\kappa_n x) + B_n^{(1)}\exp(-i\kappa_n x)\right) + \mathcal{P}_n(x) \ . \tag{4.21}$$

with $\mathcal{P}_n$ the particular solutions to Eqn. (4.20). Assuming the r.h.s. of Eqn. (4.20) to be an arbitrary function $\mathcal{G}_n$, the general form of the solution is

$$\mathcal{P}_n = e^{(\gamma/2+i\kappa_n)x}\int_0^x \frac{e^{-(\gamma/2+i\kappa_n)\xi}\mathcal{G}_n(\xi)}{2i\kappa_n}d\xi - e^{(\gamma/2-i\kappa_n)x}\int_0^x \frac{e^{-(\gamma/2-i\kappa_n)\xi}\mathcal{G}_n(\xi)}{2i\kappa_n}d\xi$$

Again, the $A_n^{(1)}$ and $B_n^{(1)}$ are found by using the boundary conditions. For the first order dynamics, these read

$$\left.\begin{aligned} \mathcal{N}_{0,j}^{(1)} &= 0 \ , \\ \mathcal{N}_{1,j}^{(1)} &= 0 \ , \\ \mathcal{N}_{2,j}^{(1)} &= 0 \ , \end{aligned}\right\} \text{at } x = l_{o,j} \ , \ j \in O \ , \tag{4.22a}$$

$$\left.\begin{aligned} \mathcal{U}_{0,j}^{(1)} &= 0 \ , \\ \mathcal{U}_{1,j}^{(1)} &= 0 \ , \\ \mathcal{U}_{2,j}^{(1)} &= 0 \ , \end{aligned}\right\} \text{at } x = l_{r,j} \ , \ j \in R \ , \tag{4.22b}$$

$$\left.\begin{aligned} g\mathcal{N}_{n,j}^{(1)} + \frac{\mu}{2}\mathcal{D}_{n,j} &= g\mathcal{N}_{n,k}^{(1)} + \frac{\mu}{2}\mathcal{D}_{n,k} \ , \\ \sum_{j\in J_\nu} b_j h_j \mathcal{U}_{n,j}^{(1)} &= -\sum_{j\in J_\nu} b_j \mathcal{S}_{n,j} \ , \end{aligned}\right\} \forall j,k \in J_\nu \ , \ \nu \in V \ . \tag{4.22c}$$

Eqns. (4.22a) denote the conditions at the ocean boundaries, while Eqns. (4.22b) represent the conditions at the landward boundaries. Furthermore, continuity of dynamic pressure is denoted by $\mathcal{D}_n$, while in the conservation of mass equation the Stokes transport appears in Eqn. (4.22c) ($\mathcal{S}_n$ from Eqn. (4.19)). The expression for the residual component of the dynamic pressure reads ($\mathcal{D}_1$ and $\mathcal{D}_2$ are given in appendix 4.A)

$$\mathcal{D}_0 = \mathcal{U}_0^{(0)2} + \frac{1}{2}\mathcal{U}_1^{(0)}\mathcal{U}_1^{(0)\dagger} \ . \tag{4.23}$$

Net water transport

The linear nature of the differential equations, Eqns. (4.14) and (4.17), allows the construction of solutions for the individual forcing mechanisms and forcing boundary conditions. The combination of the separate solutions provides the full solution to the differential equations. As a result, the residual transport due to the tidally rectified Eulerian current (the first term in Eqn. (4.10b)) is decomposed as

$$bh\mathcal{U}_0^{(1)} = bh\Big(\underbrace{\mathcal{U}_{0,\mathrm{A}}^{(1)}}_{1} + \underbrace{\mathcal{U}_{0,\mathrm{F}}^{(1)}}_{2} + \underbrace{\mathcal{U}_{0,\mathrm{C0}}^{(1)}}_{3} + \underbrace{\mathcal{U}_{0,\mathrm{S}}^{(1)}}_{4} + \underbrace{\mathcal{U}_{0,\mathrm{DP}}^{(1)}}_{5}\Big) \ . \tag{4.24}$$

In Eqn. (4.24), the terms 1 through 5 denote the Eulerian residual transport due to advection, depth dependent friction, the coupling of residual and quarter diurnal currents by quadratic bottom stress, the Stokes return flow, and dynamic pressure, respectively. The individual contributions result from the corresponding forcings described in Eqn. (4.18) (advection, depth dependent friction, and the coupling of residual and quarter diurnal currents by quadratic bottom stress), Eqn. (4.19) (Stokes transport), and Eqn. (4.22c) (dynamic pressure).

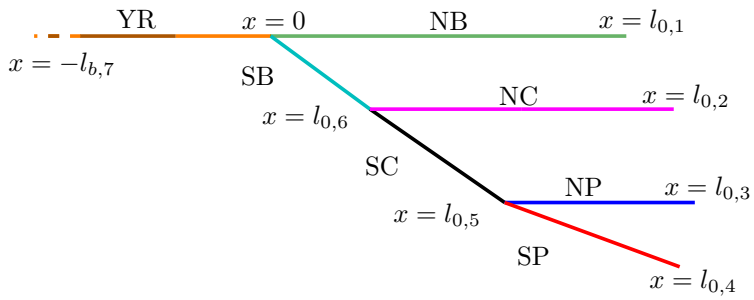

Figure 4.3: Tidal network representation of the Yangtze estuary. The along-channel coordinate, x, increases downstream (towards sea). Color coding of the channels is used in subsequent figures for easy identification of channels. The different l_o denote the end points of the channels, whereas $l_{b,7}$ is the end point of the final channel. The abbreviations of the channel names are given in the caption of figure 4.1.

4.2.2 Application to the Yangtze Estuary

The configuration of the Yangtze Estuary is that of an estuarine network, which on the large scale is characterized by a triple bifurcating structure. The discharge from Yangtze River is divided over four outlets (i.e. channels connected to the adjacent sea). The total tidal network comprises 7 channels, which are from north to south Yangtze River, North Branch, South Branch, North Channel, South Channel, North Passage, and South Passage (see Fig. 4.1). A schematic representation of the tidal network is given in Fig. 4.3. Geometric characteristics for all channels are given in table 4.1, which are derived from cross-sectional measurements in 2009 and from Google Earth. Close to the ocean boundaries the tidal range is around 2.5 m, which categorizes the estuary as meso-tidal (He *et al.*, 2001, see Table 4.2). The location of the tidal current limit varies substantially due to the strong seasonal cycle in river discharge of the Yangtze river. The monthly averaged river discharge, measured approximately 570 km landward from the apex point where the river first bifurcates, is around 10.000 m^3s^{-1} during the dry season. Monthly averaged discharge reaches values of 40.000 m^3s^{-1} in the wet season, while the annual average is around 28.300 m^3s^{-1} (Chen *et al.*, 2001; Jiang *et al.*, 2013).
Apart from strong natural variability, changes in hydrodynamics have occurred in the past decades due to large scale human interventions. A noticeable project in recent years is the Deepwater Navigation Channel (DNC) in the North Passage, which caused an increase in tidal currents (Ma *et al.*, 2011), and a decrease in ebb water diversion ratio in the North Passage.
Typical values of the drag coefficient are reported of $2.5 \cdot 10^{-3}$. Here, values have

Table 4.1: The channel length (l_b), the width at the seaward boundary (b_0), the position of the endpoint of the channel (l_0), the convergence length scale (l_c), and the depth (h) for all channels in the network after construction of the Deepwater Navigation Channel (DNC).

Channel	nr.	l_b (km)	b_o (km)	l_o (km)	l_c (km)	h (m)
Yangtze river 5 (YR5)	12	370	2.5	-200	1660	10
Yangtze river 4 (YR4)	11	50	3.2	-150	206	10
Yangtze river 3 (YR3)	10	50	4.1	-100	206	10
Yangtze river 2 (YR2)	9	50	5.2	-50	206	10
Yangtze river 1 (YR1)	8	50	6.6	0	206	10
North Branch (NB)	1	85	12	85	30	5
South Branch (SB)	7	51	14	51	64	9
North Channel (NC)	2	60	20	121	52	7
South Channel (SC)	5	23	6.2	74	-368	9
North Passage (NP)	3	61	3.5	135	470	11
South Passage (SP)	4	54	30	129	21	7

been chosen of $1.25 \cdot 10^{-3}$ in the network part of the estuary (i.e. the region downstream of the first bifurcation) to represent the data more accurately. These low values could be a result of high suspended sediment concentrations, which dampen turbulence and thus reduce frictional drag. Values were still taken a constant over a large area, such that fitting did not become the dominant process for obtaining reliable results. The value was increased linearly in 5 steps to $2.5 \cdot 10^{-3}$ for the Yangtze River.

Table 4.2: Values of the parameters related to the external forcing.

Channel	Forcing
YR5	10.000/40.000 $\mathrm{m^3 s^{-1}}$
NB	$1.55\cos(\sigma t - 0.92\pi)$
NC	$1.06\cos(\sigma t - 0.89\pi)$
NP	$1.30\cos(\sigma t - 0.89\pi)$
SP	$1.30\cos(\sigma t - 0.92\pi)$
σ	$1.4 \cdot 10^{-4}$ $\mathrm{s^{-1}}$

4.3 Results

This section first presents results on the tidal wave propagation and net water transport in the Yangtze estuary during dry and wet season. After that, the effect of the DNC on tidal propagation and net water transport will be investigated.

4.3.1 Tidal characteristics in the dry and wet season

The semi-diurnal tide

Figs. 4.4(a) and 4.4(b) show the amplitude and phase of the sea surface height of the semi-diurnal tide representative for the dry season after the construction of the DNC. The solid lines show the results for the sum of the leading order solution and the first order solution ($\mathcal{N}_1^{(0)} + \mathcal{N}_1^{(1)}$), while the dots in panels (a) and (b) show results from a harmonic analysis of the tidal table data for January 2011 (National Marine Data and Information Service, 2013). The locations of the tidal stations are shown in panel (c), while the station names are given in Table 4.3.
There is a fair agreement between the modeled and observed vertical tide, considering the simplified representation of the estuary applied in the model. The tidal amplitude in the North and South Passage generally decreases, with a notable difference between the modeled and observed sea surface amplitude at the most seaward station (station 7, Jigujiao). However, this station is located outside the DNC, and might therefore not be appropriately represented in the model. The modeled amplitude in South Branch is higher than the observed amplitude available from the local stations (9 and 13), but the model does show the increase in tidal amplitude from North Channel to South Branch.
The phase of the tidal wave is also represented reasonably well, as is seen in Fig. 4.4(b). The modeled tidal wave seems to propagate slightly faster in the

Table 4.3: Tidal table stations. Numbers reference to panel (c) in figure 4.4.

Number	Station name	Number	Station name
1	Baimaikou	9	Nanmengang
2	Beicaozhong	10	Niupijiao
3	Changxing	11	Qinglonggang
4	Hengsha	12	Sheshan
5	Hupu	13	Shidongkou
6	Jiangyin	14	Tianshenggang
7	Jigujiao	15	Wusong
8	Nancaodong	16	Zhongjun

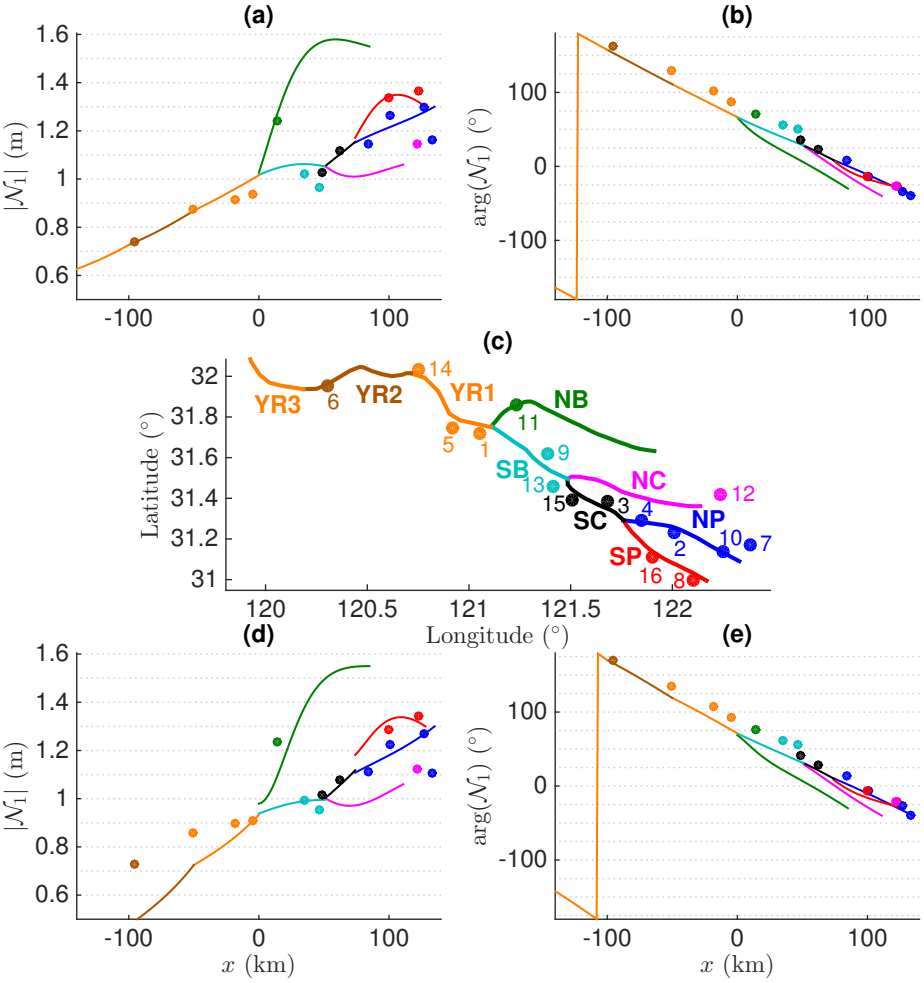

Figure 4.4: Sea surface height amplitude ($|\mathcal{N}_1|$, i.e. the absolute value of $\mathcal{N}_1$) and phase ($\arg(\mathcal{N}_1)$, i.e. the argument of $\mathcal{N}_1^{(0)}$) of the semi-diurnal tide versus distance x from the first bifurcation after construction of the DNC in the dry (wet) season in panel (a) and (b) (panel d and e), respectively. Lines show model results ($\mathcal{N}_1^{(0)} + \mathcal{N}_1^{(1)}$), and the dots show the data from the tidal table (National Marine Data and Information Service, 2013). Panel (c) shows a map of the Yangtze Estuary, where the colors correspond to the schematic from figure 4.3 for reference. The dots show the locations of the tidal stations, while the numbers reference to the station number from table 4.3.

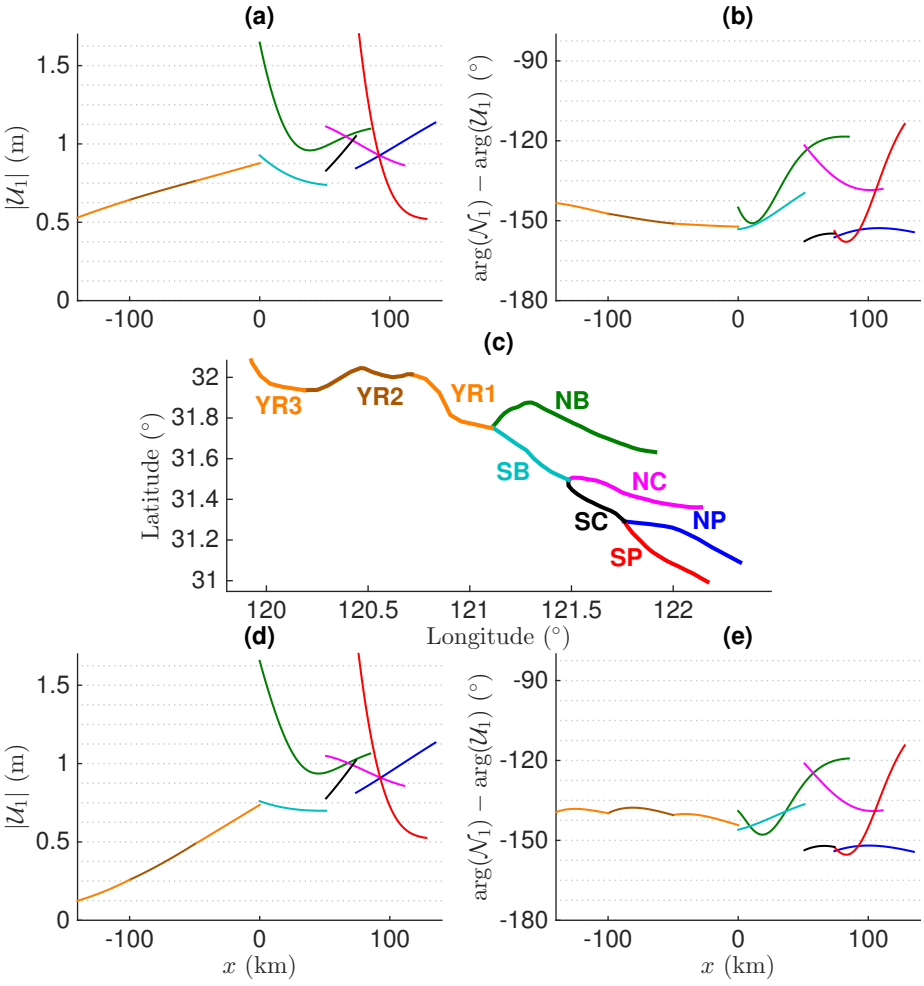

Figure 4.5: Velocity amplitude ($|\mathcal{U}_1|$) and phase relative to sea surface height ($\arg(\mathcal{N}_1) - \arg(\mathcal{U}_1)$) of the semi-diurnal tide versus distance x from the first bifurcation after construction of the DNC in the dry (wet) season as computed with the semi-analytical model in panel (a) and (b) (panel d and e), respectively. Panel (c) shows a map of the Yangtze Estuary, where the colors correspond to the schematic from figure 4.3 for reference.

network part of the estuary than the data suggest. The difference between the modeled and observed phase of the semi-diurnal tide decreases in the upstream part of the Yangtze River, which suggests that there the propagation of the tidal wave is slower in the model than in the field.
Panels (d) and (e) of Fig. 4.4 show the semi-diurnal tidal characteristics for the wet season after construction of the DNC. The increase in river discharge results in stronger attenuation of the tide compared to that in the dry season, which is especially visible in the Yangtze River. However, modeled tidal amplitudes in the Yangtze River are smaller than observed amplitudes in this area. There is no significant difference between the phase propagation of the tide in the wet and dry season, but phase propagation is slower in the wet season than in the dry season due to the increased friction levels.
Fig. 4.5 shows the modeled velocity characteristics after construction of the DNC. Panel (a) shows the velocity amplitude in the dry season, while panel (b) shows the phase relative to the sea surface elevation for the same season. The latter is an important quantity in determining the amount of Stokes transport by the semi-diurnal tidal wave (see term 3 in Eqn.(4.10b)). Stokes transport is maximum when the phase difference is $-180°$ (flood velocities are negative), while Stokes transport is 0 for a phase difference of $-90°$. Figs. 4.5(d) and 4.5(e) show the same as Figs. 4.5(a) and 4.5(b), but for the wet season. Velocities are lower in the wet season than in the dry season. This is a consequence of the increased river discharge, which results in increased friction values. Fig. 4.5(e) reveals that the phase difference between the sea surface elevation and velocity in the wet season is higher than in the dry season, which results in a reduced Stokes transport in the wet season.

The quarter diurnal tide

Model results and observations for sea surface height of the quarter diurnal (M_4) tidal wave are shown in Fig. 4.6. Again, panel (a) and (b) respectively show the tidal amplitude and phase for the dry season after construction of the DNC. Panels (c) and (d) show the same, but for wet season. The dots represent the observations, while the lines represent the model results. The model reproduces the increase in amplitude when moving into the estuary, as observed in the data The phase of the tidal wave is also similar, with the largest differences between model and data in North Channel and South Passage. Another difference between modeled and observed M_4 tide is that the latter show smaller amplitudes in the wet season than in the dry season, similar to the semi-diurnal tide, while the model produces larger quarter diurnal tidal amplitudes in the wet season than in the dry season. This indicates there are missing terms for the quarter diurnal tide, such as mass storage on the tidal flats, or momentum advection in the lateral direction.

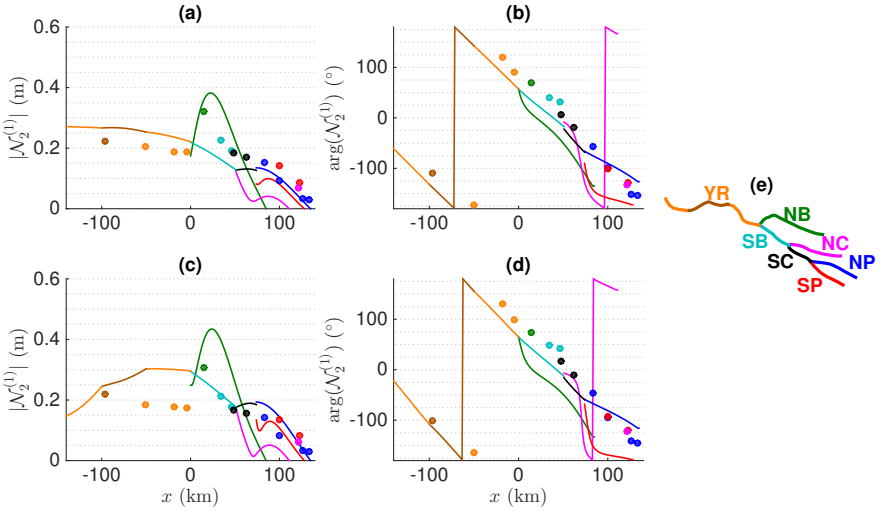

Figure 4.6: Sea surface height amplitude ($|\mathcal{N}_2^{(1)}|$) and phase ($\arg(\mathcal{N}_2^{(1)})$) of the quarter diurnal (M_4) tide versus distance x from the first bifurcation after construction of the DNC in the dry (wet) season in panel (a) and (b) (panel c and d), respectively. Lines show model results, while the dots show the data from the tidal table (National Marine Data and Information Service, 2013). Panel (e) shows the geometry of the Yangtze Estuary for reference of the colors.

Velocity characteristics of the M_4 tidal wave as computed with the model are shown in Fig. 4.7. The panels show amplitude and phase in the dry and wet season in panels (a) through (d), identical to Fig. 4.6. Similar to the sea surface elevation amplitudes, velocity amplitudes attain a maximum in the interior of the estuary because they are internally generated. Compared to the dry season, attenuation rates in the wet season are higher and tidal wave propagation is slower.

4.3.2 Net water transport in the dry and wet season

Net water transport involves river transport, viz. $Q_0^{(0)}$ in Eqn. (4.10a), and residual transport due to tidal rectification, i.e. $Q_0^{(1)}$ in Eqn. (4.10b). Fig. 4.8 shows the river transport in the different channels for the dry season in panel (a) by the dashed lines, while the net water transport (i.e. $Q_0^{(0)} + Q_0^{(1)}$) is shown by the solid lines. Fig. 4.8(b) shows the solutions for $Q_0^{(1)}$ for dry season by the dashed-dotted lines. Fig. 4.8(c) and 4.8(d) are identical to Fig. 4.8(a) and 4.8(b), except that they show solutions for the wet season

From Figs. 4.8(a) and (c), it is observed that distribution of river transport over

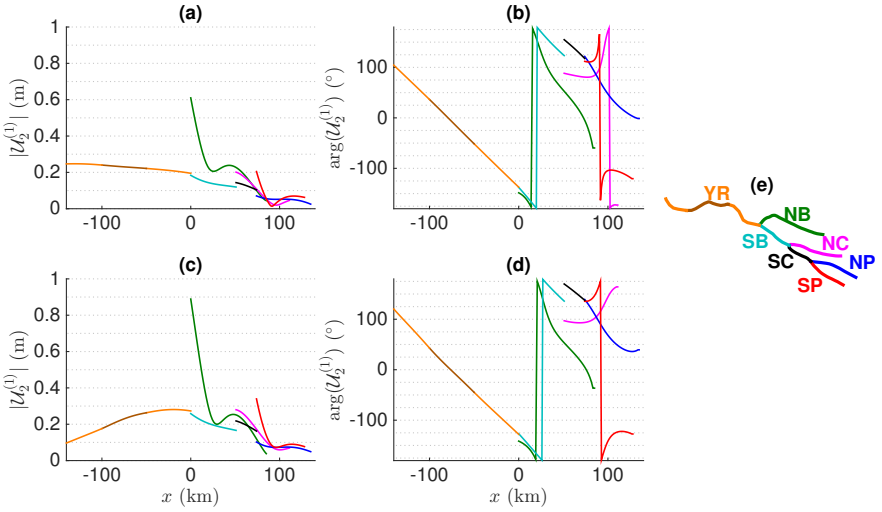

Figure 4.7: As Fig. 4.6, but for the M_4 velocity ($\mathcal{U}_2^{(1)}$).

the different channels is similar for both seasons, with wet season having a slightly more uneven distribution between North and South Channel, and a slightly more even distribution between North and South Passage. River transport through the North Branch is small compared to that in the South Branch due to the small cross-sectional area at the most upstream bifurcation where the Yangtze River bifurcates in the North and South Branch. The results confirm that $Q_0^{(1)}$ both enhances (as described by Buschman *et al.*, 2010) as well as decreases (as described by Sassi *et al.*, 2011) the uneven division of river transport at various bifurcations. The former occurs at the bifurcation between the North and South Channel, while the latter occurs at the bifurcation between the North and South Passage. Net water transport shows a larger variation in distribution over the channels between the dry and wet season than river transport. This is apparent from the net water diversion ratio, nWDR from Eqn. (4.5), given by the percentages in Fig. 4.8(a) and 4.8(c). The nWDR changes about 5 percentage point between the dry and wet season for all channels.

Figs. 4.8(b) and (d) reveal that $Q_0^{(1)}$ in the dry and wet season are similar for all channels, which is remarkable considering the differences in tidal characteristics (Fig. 4.4). Downstream of the bifurcation of the Yangtze River, tidal rectification produces a net water transport of a similar magnitude as the local river transport. Especially during dry season, the net water transport is determined for a large part by $Q_0^{(1)}$. Particularly, the North Branch hardly experiences any net water

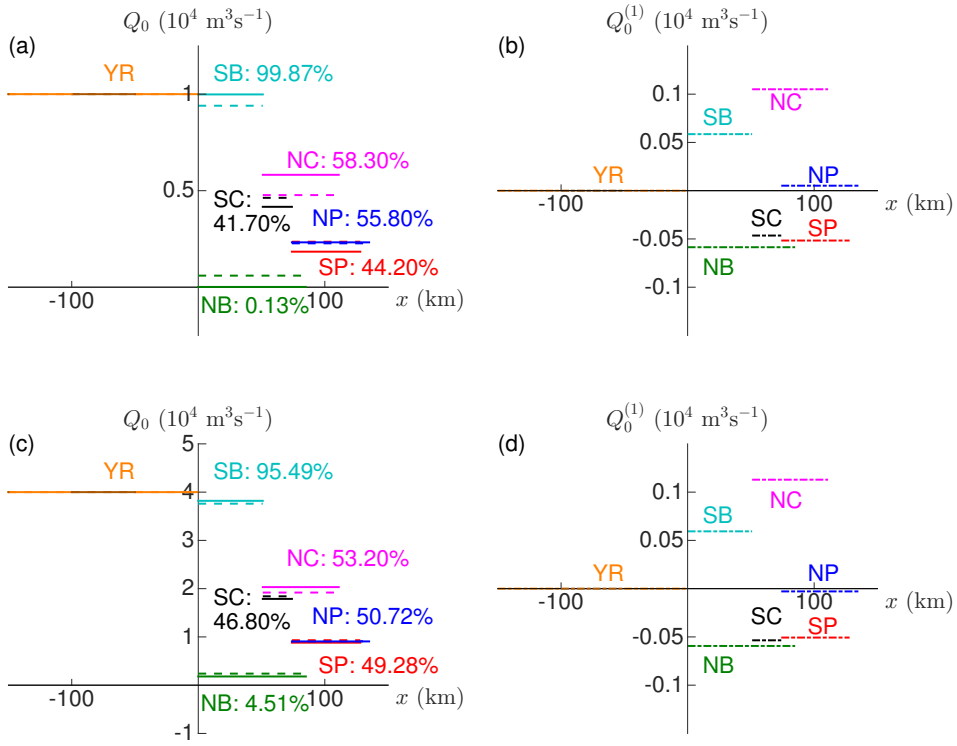

Figure 4.8: Panel (a) shows net water transport (Q_0, solid lines) and river transport ($Q_0^{(0)}$, dashed lines). Panel (b) shows residual transport due to tidal rectification ($Q_0^{(1)}$, dashed-dotted lines) in the dry season after construction of the DNC as a function of along-channel position x. Panels (c) and (d) are as panels (a) and (b), but for the wet season. Positive values denote transport towards the sea. The abbreviations of the channel names are defined in Table 4.1. The numbers denote the values of the net water diversion ratio, nWDR, as defined in Eqn. (4.5).

transport during dry season, which frequently leads to strong salt intrusion and even a spill over into South Branch, as reported by Wu *et al.* (2006).

4.3.3 Effect of the DNC on tidal characteristics

To study the effect of the DNC on the tidal hydrodynamics, the model geometry of the Yangtze Estuary was altered to represent the estuary in its historic state, i.e. prior to the construction of the DNC. Particularly, the geometry of the North Pas-

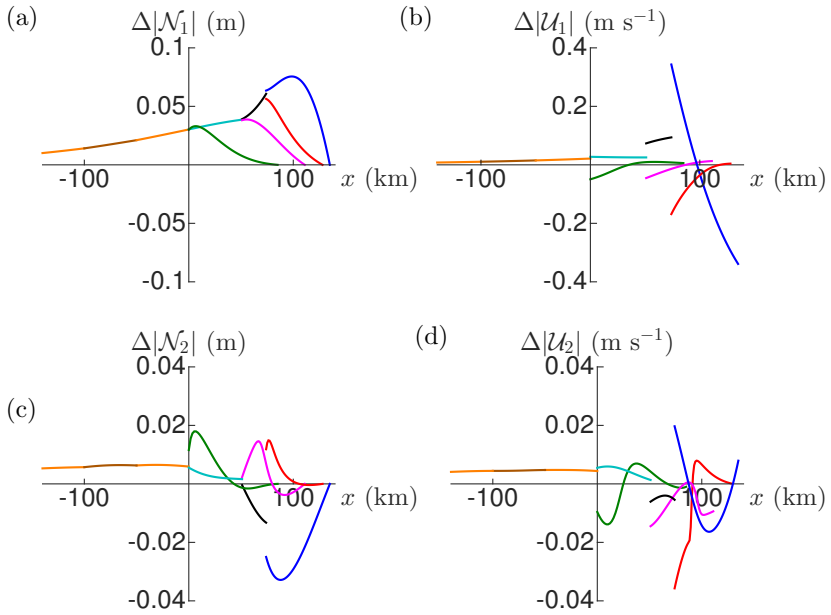

Figure 4.9: Difference between M_2 and M_4 tidal amplitudes in dry season before and after construction of the DNC. Panels (a) and (b) show the difference in sea surface height and velocity amplitude of the M_2 tide as a function of the along-channel position x, respectively. Panels (c) and (d) show the same for M_4. Note the different scales on the vertical axes in the panels.

sage was changed, for which new parameter values are given in Table 4.4. Prior to the construction of the DNC, the North Passage was shallower, and more funnel-shaped. The difference between the model results before and after construction of the DNC is presented in Fig. 4.9, i.e. model results using the default setting are subtracted from results using the new configuration. Panel (a) shows the difference in semi-diurnal sea surface height amplitude, while panel (b) shows the difference in semi-diurnal velocity amplitude. Sea surface height amplitudes decreased due to

Table 4.4: Geometrical parameters for the North Passage before construction of the DNC.

Channel	nr.	l_b (km)	b_0 (km)	l_0 (km)	l_c (km)	h (m)
North Passage (NP)	3	61	8.5	135	60	10

the construction of the DNC, while velocities have mostly increased. Velocity amplitude changed the most in the North Passage, consistent with earlier studies (Ma *et al.*, 2011) and observations (Jiang *et al.*, 2013), with increased velocities near the ocean boundary and decreased velocities towards the bifurcation point with South Passage. Velocity amplitude increased in South Passage, North Channel and North Branch, and decreased in South Channel and South Branch, indicating the global effect in the system of large scale interventions. Figs. 4.9(c) and 4.9(d) show the same as Figs. 4.9(a) and 4.9(b), but for the quarter diurnal harmonic component. Changes in this component are small for both sea surface elevation and velocity. Apart from North Passage and South Channel, sea surface height amplitudes of the M_4 tide decreased.

4.3.4 Effect of the DNC on net water transport

The effect of the DNC on net water transport is quantified by investigating changes in the net water diversion ratio (nWDR see Eqn. (4.5)). These changes are shown in Fig. 4.10. This figure shows for every channel the nWDR in green (blue) for the dry (wet) season before the construction of the DNC. Orange and cyan bars represent the nWDR in the dry and wet season after construction of the DNC, respectively. The latter bars represent the nWDR values shown in Figs. 4.8(a) and 4.8(c), respectively. The largest changes occurred at the bifurcation between North and South Passage. In the configuration after the construction of the DNC, North Passage receives a smaller fraction of the net water transport supplied by the South Channel. Changes are also observed at the bifurcation between North and South Channel. After the construction of the DNC, more net water transport from the South Branch is discharged through the North Channel. Consequently, the net water transport through North Passage is even smaller after construction of the DNC than before, since there is a smaller supply of net water transport from upstream.

4.4 Discussion

The results in section 4.3 showed differences in net water transport due to changes in river discharge, as well as due to changes in geometry. Relative distribution of river transport and residual transport due to nonlinear tidal rectification were similar in the wet and dry season. The construction of the DNC caused changes in tidal hydrodynamics, such as decreased semi-diurnal sea surface height amplitudes. This section will first compare the net water transport results from this study with reports in literature. During this comparison, important processes will be identified that determine the net water transport. Secondly, results on how these processes changed due to the construction of the DNC will be discussed. Thirdly,

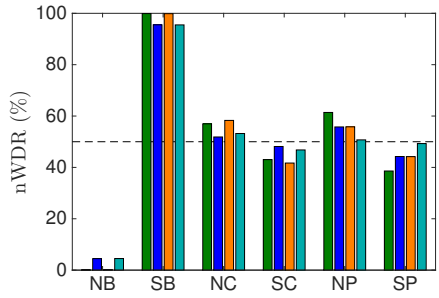

Figure 4.10: Net water diversion ratio nWDR, from Eqn. (4.5), computed for all channels in the dry and wet season before and after the construction of the DNC in green, blue, orange and cyan, respectively. The orange and cyan bars represent the nWDR values shown in Figs. 4.8(a) and 4.8(c), respectively. Channel name abbreviations are given in Table 4.1.

the results will be compared with the results from a 1D numerical network model to study the implications of the assumptions made in the analytical model (viz. the harmonic truncation, the truncated perturbation expansion and the linearization of the quadratic bottom stress).

4.4.1 Comparison of model output with literature

The smaller semi-diurnal tidal amplitudes obtained in wet season with the semi-analytical model, as well as the stronger seasonality of the tidal amplitude in the Yangtze River compared to the seasonality in the downstream part of the network are consistent with observations presented in Guo *et al.* (2015). Additionally, they reported higher M_4 tidal amplitudes in the downstream part of the Yangtze Estuary during the wet season, which is also found with the semi-analytical model. This contrasts the findings in the data from this manuscript, which have smaller M_4 tidal amplitudes in wet season throughout the estuary. Some of their observations are not reproduced, such as an occasional increase in M_2 tidal amplitude in wet season during spring tidal conditions. This might be the result of the damping of turbulence by stratification, which also causes stronger tides outside the Yangtze Estuary in the East China Sea during wet season (Kang *et al.*, 2002).
Fig. 4.11 shows ebb water diversion ratio, eWDR defined in Eqn. (4.6), for the North Passage as computed by the model in the diamonds. The green and blue diamonds show the model results before construction of the DNC, while the orange and cyan diamonds show model results after construction of the DNC. The green and orange diamonds show dry season values, while the blue and cyan diamonds

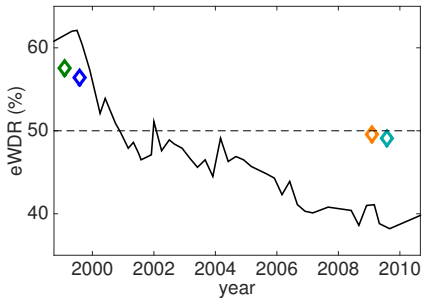

Figure 4.11: Observed ebb water diversion ratio eWDR, as defined in Eqn. (4.6), versus time at the bifurcation point between North and South Passage and South Channel is shown by the black line. The diamonds represent model values of the eWDR with geometries from Table 4.1 and 4.4, where green and orange represent dry season and blue and cyan represent wet season. Figure after Gao *et al.* (2009) and Jiang *et al.* (2012).

show wet season values. Observed eWDR's from Gao *et al.* (2009) are shown in the solid line. Gao *et al.* (2009) and Hu & Ding (2009) found that due to the DNC the eWDR has decreased in the North Passage from about 60% prior to the DNC, to 40% afterwards. The model reproduces the decreasing trend in eWDR observed in the measurements. However, the decrease computed by the model is less than observed. This is probably due to the effect of the training walls, which has not been accounted for in this model. These caused an increase in frictional drag in the North Passage, as reported by Gao *et al.* (2009) and Hu & Ding (2009).
The eWDR computed with the semi-analytical model is compared with results from Li *et al.* (2010) in Fig. 4.12(a). They used a complex numerical model to investigate both eWDR and nWDR in the different channels of the Yangtze Estuary. Their model includes additional processes, such as the effect of wind, the earth's rotation, spring-neap variations and salinity gradients. They performed a sensitivity study on wind forcing, with one scenario having zero wind stress. In Fig. 4.12(a), the orange bars are the eWDR in dry season after construction of the DNC as computed by the semi-analytical model. The pink and grey bars denote the values reported by Li *et al.* (2010). They report eWDR values for neap and spring tidal conditions, which are shown in the pink and grey bars, respectively. Since spring-neap variations are not accounted for in the semi-analytical model, the comparison is only made qualitative. At each bifurcation, the semi-analytical model produces a distribution similar to that obtained with the complex model.
Fig. 4.12(b) shows a similar comparison as in panel (a), but for the nWDR in dry season. Additional values as reported by Zhang *et al.* (2011) are shown in

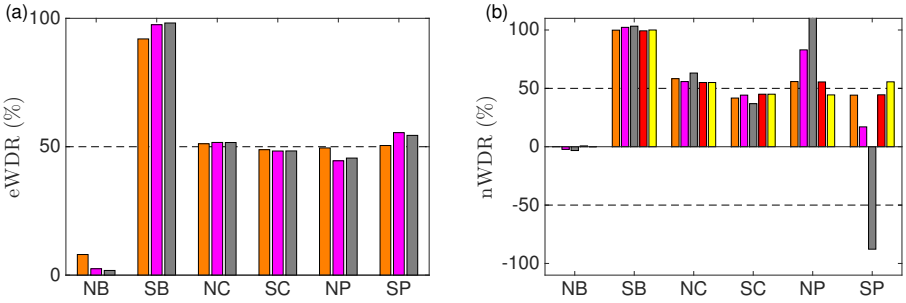

Figure 4.12: Comparison of the eWDR and nWDR as computed by the present model with values from literature in panel (a) and (b), respectively. Values are in percent for the dry season after construction of the DNC in orange. The eWDR value for the North Passage (panel a) corresponds to the orange diamond in Fig. 4.11. Values from Li *et al.* (2010) are in pink and grey and values from Zhang *et al.* (2011) are in red and yellow. For Li *et al.* (2010), pink bars are their neap tide results and grey bars are spring tide results. For Zhang *et al.* (2011), red bars are results for 17-18 Feb. 2003 and yellow bars are results for 9 Oct. 2006. Note that the nWDR value from Li *et al.* (2010) for North Passage during spring tide is off the scale at 184.79%. Channel name abbreviations are given in Table 4.1.

red and yellow. Here, the red bars represent their results from 17-18 Feb. 2003 and the yellow bars represent results for 9 Oct. 2006. Zhang *et al.* (2011) used an idealized model for salt intrusion, which they combined with data on salt intrusion to estimate the net water transport through the different channels of the Yangtze Estuary. The values for nWDR computed at all bifurcations with their model and the current model agree fairly well for the 2003 data (red bars) . In 2006, Zhang *et al.* (2011) predict the South Passage to have a larger outflow than North Passage, which is not found by the semi-analytical model. However, they do report a decrease of net water transport through North Passage during the construction of the DNC, as can be seen by comparing the red and yellow bars.

Comparing the results from Li *et al.* (2010) with the results from the semi-analytical model, a difference is observed for the North and South Branch. Li *et al.* (2010) report a net import of water through the North Branch. Net water transport through North Branch also reverses in this model for stronger tidal conditions or lower river discharge (not shown). Furthermore, the nWDR in South Passage is much smaller in the model from Li *et al.* (2010) than in the present study. For spring tidal conditions, a net import of water through South Passage is reported (note that this causes nWDR in North Passage to have a value of

184.79%, which is off the scale). The difference between the two models could be caused by density gradients and their resulting currents, or the presence of intertidal areas in the model of Li *et al.* (2010).

4.4.2 Net water transport mechanisms

The results of the semi-analytical model, as well as the results from Li *et al.* (2010), indicate a stronger net water transport in North Passage than in South Passage. To identify which nonlinear interactions are responsible for this distribution, Fig. 4.13 shows the different components of the net water transport as defined in Eqns. (4.10) and (4.24) in dry season. The changes that occurred in the individual contributions are investigated by comparing results after and before the construction of the DNC in the solid and dashed lines, respectively. Panels (a) through (f) show the contribution to net water transport due to river transport, horizontal advection, depth dependent friction, the effect of the coupling between residual and quarter diurnal currents by quadratic bottom stress, the Stokes transport and the associated return current, and dynamic pressure, respectively (for definitions see Eqn. (4.24)). River induced transport is the largest component of the net water transport in all channels, except in North Branch. The second term is the advection term, shown in Fig. 4.13(b). However, this term is of opposite sign as the dynamic pressure term in Fig. 4.13(f), and is largely compensated by it. Depth dependent friction (panel c), the coupling between residual and quarter diurnal currents (panel d), and Stokes transport and the associated return current (panel e) are of similar magnitude and thus contribute equally to the net water transport in the network.
The observed change in distribution of net water transport over the North and South Passage is caused by a decrease in river transport through North Passage (panel a) due to the construction of the DNC, and an increase through South Passage. The residual transport due to the tidal rectification through North Passage and South Passage increased due to the construction of the DNC for nearly all nonlinear processes (panels b through f), except for the residual transport due to the coupling between the residual and quarter diurnal currents, which did not change significantly (panel d).

4.4.3 Comparison of model output with a 1D numerical model

This model has applied several techniques to derive semi-analytical solutions to Eqns. (4.2a) and (4.2b), such as a new approximation to the quadratic bottom stress, a harmonic truncation and a perturbation analysis. In order to verify to what extend this approach is valid, a comparison will be presented between

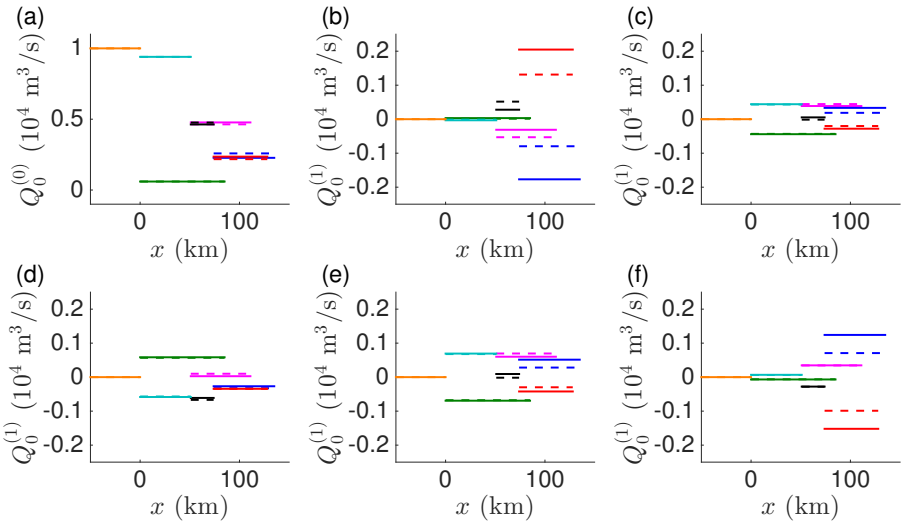

Figure 4.13: Different contributions to the net water transport ($Q_0^{(0)}$ and $Q_0^{(1)}$) in the dry season after and before construction of the DNC in solid and dashed lines, respectively. The panels show the solutions for; (a) river transport, (b) horizontal advection, (c) depth dependent friction, (d) the effect of λ_{c0}, (e) the Stokes transport and the associated return current, and (f) dynamic pressure.

the model results from the semi-analytical model and a model, which solves Eqns. (4.2a) and (4.2b) numerically. The latter model uses a central differencing scheme in the spatial coordinates and a Runge-Kutta(4) scheme for its time integration. Boundary conditions to the numerical model are identical to the ones posed in Eqn. (4.3).

Fig. 4.14 shows the results for the comparison, which was done for the dry season, after the construction of the DNC. In panel (a) and (b), the amplitude of the semi-diurnal amplitude of the sea surface height and velocity are plotted, respectively. Solid lines represent the results of the semi-analytical model, while the dashed lines represent the results of the numerical model. Overall, the differences are small, with an average error around 4%. This also holds for the phase of the sea surface height and velocity (panels c and d). Results for the quarter diurnal tide are shown in panels (e), (f), (g), and (h). Solid lines show the results of the semi-analytical model, and dashed lines the results of the numerical model. The average error in amplitude is about 18% for the quarter diurnal tide. Additionally, the dotted lines represent the results of the semi-analytical model without the coupling between the residual and quarter diurnal currents through quadratic bottom stress (i.e.

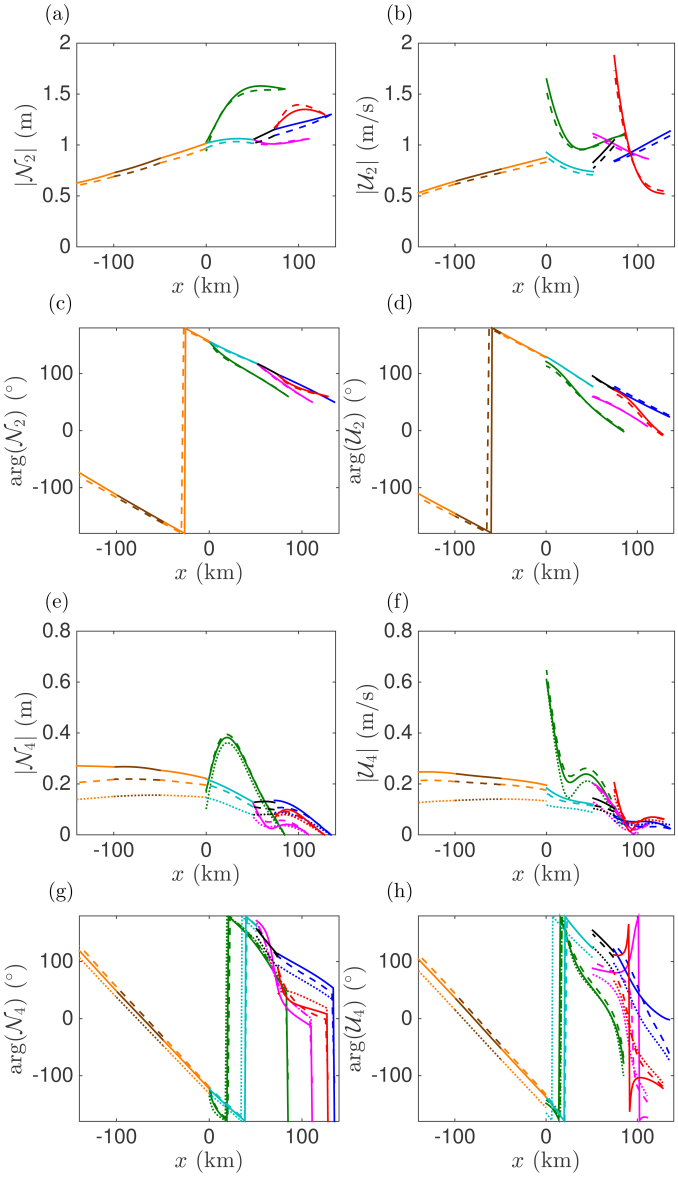

Figure 4.14: Comparison of the tidal characteristics between the semi-analytical model (solid lines) and the 1D numerical model (dashed lines) for the dry season, post DNC configuration. Panels (a) and (b) show the sea surface height and velocity amplitude of the M_2, while panel (e) and (f) show the same for M_4. Panels (c), (d), (g), and (h) show the phases of these quantities. In panels (e) through (h), the dotted lines show semi-analytical model results for $\lambda_{c2} = 0$, i.e. without the coupling between residual and quarter diurnal currents.

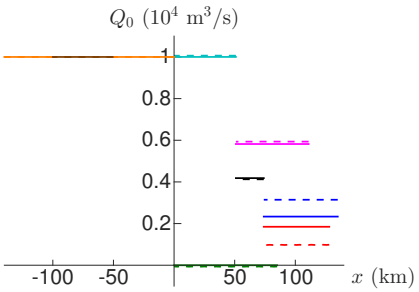

Figure 4.15: Comparison of the net water transport between the semi-analytical model (solid lines) and the 1D numerical model (dashed lines) for the dry season, post DNC configuration.

coefficient $\lambda_{c2} = 0$, where λ_{c2} is defined in Eqn. (4.12)). Without the coupling of the currents, the average error in amplitude is about 27%. This confirms the validity of the new approach adopted in linearizing the quadratic bottom stress in the semi-analytical model, and shows the strong influence of the river discharge on quarter diurnal tidal wave propagation.
Fig. 4.15 shows the distribution of the net water transport over the different channels, as calculated with the two models. Solid lines represent the results of the semi-analytical model and dashed lines are those of the numerical model. Overall, there is a good agreement between the net water transport obtained with both models. The largest difference is observed for the bifurcation between North and South Passage, which might be caused by the strong gradients in the semi-diurnal tidal velocity. These cause advective transport that is not captured accurately by the semi-analytical model. However, the semi-analytical model still captures the same relative division at this bifurcation, i.e. that North Passage has a higher net water transport than South Passage.

4.4.4 Model considerations

Despite several approximations, the model is able to capture the dominant features of tidal propagation and net water transport through the Yangtze Estuary, such as the increase in quarter diurnal tidal amplitude upstream in the Yangtze Estuary, and the decrease in eWDR in the North Passage due to construction of the DNC. Although these results have also been obtained with complex numerical models (e.g. Hu & Ding, 2009), the benefit of this modeling approach lies in the additional insight which the analytical solutions provide. This makes it possible to decompose the full solution into the contributions of its individual processes, allowing

the identification of dominant processes. Additionally, the model demands little computational power, is suited for performing sensitivity analyses and is readily applicable for other estuarine networks.
The comparison between the model and observations could be improved by slight adjustments in the drag coefficients, the phases at the open boundaries, or the depth of the channels. However, it is not the aim of this study to represent the data as accurately as possible, but rather to gain insight in the governing mechanisms of net water transport in estuarine networks. The errors in the phase of the sea surface height and velocity do not significantly influence the results for the net water transport and are therefore considered acceptable.
Additionally, this model neglected some processes such as the residual flow that results from density gradients caused by gradients in salinity. Density gradients cause a residual waterlevel set-up in single channel estuaries due to the gravitational circulations (Hansen & Rattray, 1965), as well as through asymmetric mixing (cf. Burchard & Hetland, 2010; Cheng *et al.*, 2010; Stacey *et al.*, 2010). This set-up results in additional residual water transport between channels in estuarine networks. Moreover, adding salinity dynamics yields insight in the differences in salt water intrusion between different channels, which in the Yangtze Estuary frequently result in spill-over of salt water from the North to the South Branch (Wu *et al.*, 2006).
Another neglected process is the temporal storage of water on intertidal areas (as described by Speer & Aubrey, 1985; Friedrichs & Aubrey, 1988; Ridderinkhof *et al.*, 2014), which gives rise to additional quarter diurnal tides. Tidal flats at present are mostly located alongside North Channel and South Passage, which are the two channels where quarter diurnal tides are underestimated most. Before construction of the DNC, there were also extensive tidal flats adjacent to North Passage. The effect of the disappearance of these tidal flats on the tidal wave propagation and the indirect effect on the net water transport has not been investigated and is an important topic for future investigations.
Finally, in the present model only one tidal constituent (M_2) is imposed at the seaward boundary. Tides in the Yangtze Estuary however also show noticeable diurnal components (daily inequality) and spring-neap variations (presence of the semi-diurnal S_2 constituent). Since diurnal components are about 25%, and the S_2 component about 50% of the M_2 tide, the net water transport due to tidal rectification of these components are expected to be an order of magnitude smaller than that of the M_2 tide. This approach yields insight in the stationary response of the system, revealing many characteristics observed in measurements.

4.5 Conclusions

In this manuscript, the influence of river discharge and geometry on tidal wave propagation and net water transport in estuarine networks was investigated. This was done using a semi-analytical model, which solves the cross-sectionally averaged shallow water equations, using a truncated harmonic expansion and a perturbation series. The model was applied to the Yangtze Estuary as a case study.
Model results were compared to sea surface height amplitude and phase data at 16 tidal stations. It was shown that an increase in river discharge leads to stronger attenuation of the semi-diurnal tide. Internal generation of the tide by nonlinear river-tide interactions were further shown to cause a decrease in semi-diurnal sea surface elevation amplitude. Semi-diurnal tidal velocity amplitude and the phase of sea surface height and velocity were hardly affected by the internally generated tide. Distribution of river induced transport, as well as residual transport induced by nonlinear tidal rectification, were shown to be fairly insensitive to river discharge. However, the relative contribution to net water transport of the latter is larger during low discharge. Hence, net water transport distribution experiences a stronger seasonal variability than either river transport distribution, or residual transport due to nonlinear tidal rectification.
Contrary to reports in earlier studies, this study showed that not only Stokes transport and its associated return current are important in driving net water transport in estuarine networks. Other nonlinear processes, such as horizontal advection of momentum, contribute equally in the distribution of net water transport over the different channels. Additionally, the importance was stressed of two terms which have received little attention in earlier literature compared to the more classical nonlinear interactions (viz. horizontal advection, the depth dependent term in friction, and Stokes transport). The first is the continuity of dynamic pressure at channel bifurcations. This term replaces the classical assumption of continuity of surface elevation at bifurcation points. The second is a coupling between residual and quarter diurnal currents through the quadratic bottom stress and was derived through a linearization of the quadratic bottom stress using Chebyshev polynomials.
An additional comparison of the semi-analytical model with the output from a numerical 1D model was performed to verify to what extent the model assumptions in the semi-analytical model were valid. This yielded additional confirmation that the coupling between residual and quarter diurnal currents by quadratic bottom stress is important in generating net water transport and quarter diurnal tides. Including the coupling between residual and quarter diurnal currents in the semi-analytical model reduced the difference between its results and the results obtained with the numerical model.

4.A Construction of approximate solutions

To analyze Eqns. (4.2a) and (4.2b), two techniques will be applied to the system variables. These are a harmonic truncation and a perturbation analysis. The former retains only the semi-diurnal, quarter diurnal and residual components of any variable, while the latter orders the various terms in the equations on their relative magnitude. The perturbation analysis requires a scaling of the dimensional equations. All these techniques will be consecutively presented in this appendix.

4.A.1 Harmonic truncation

Using the harmonic truncation, the velocity and sea surface elevation are written as

$$\begin{aligned} u_j &= \mathcal{U}_{0,j} + \frac{1}{2}(\mathcal{U}_{1,j}e^{-i\sigma t} + \mathcal{U}^{\dagger}_{1,j}e^{i\sigma t}) + \frac{1}{2}(\mathcal{U}_{2,j}e^{-2i\sigma t} + \mathcal{U}^{\dagger}_{2,j}e^{2i\sigma t}) \ , \\ \eta_j &= \mathcal{N}_{0,j} + \frac{1}{2}(\mathcal{N}_{1,j}e^{-i\sigma t} + \mathcal{N}^{\dagger}_{1,j}e^{i\sigma t}) + \frac{1}{2}(\mathcal{N}_{2,j}e^{-2i\sigma t} + \mathcal{N}^{\dagger}_{2,j}e^{2i\sigma t}) \ . \end{aligned} \tag{4.25}$$

First, the expansion is applied to the quadratic bottom stress term to construct an approximation to the friction term, which is linear in the velocity. Second, the expansion is applied to the momentum equation, Eqn. (4.2a). Third, it is applied to the continuity equation, Eqn. (4.2b). Finally, the harmonic truncation is applied to the boundary conditions, Eqn. (4.3a)–(4.3d).

Quadratic bottom stress

The quadratic bottom stress is approximated with the use of Chebyshev polynomials (Godin, 1991, 1999), viz.

$$C_{d,j}|u_j|u_j = C_{d,j}U_j^2|\tilde{u}_j|\tilde{u}_j \approx C_{d,j}U_j^2 \sum_{m=0}^{3} A_{m,j}T_m(\tilde{u}_j) \ , \tag{4.26}$$

with $\tilde{u}_j = u_j/U_j$ a normalized velocity, $U_j = |\mathcal{U}_{0,j}|+|\mathcal{U}_{2,j}|+|\mathcal{U}_{4,j}|$ a space dependent velocity scale, and

$$A_{m,j} = \frac{2}{\pi}\int_{-1}^{1} \frac{|\tilde{u}_j|\tilde{u}_j \ T_m(\tilde{u}_j)}{\sqrt{1-\tilde{u}_j^2}} \ d\tilde{u}_j \ ,$$

where $T_m(\tilde{u}_j)$ are the Chebyshev polynomials of order m, which read for the first four orders

$$\begin{aligned} T_0(\tilde{u}_j) &= 1 \ , & T_1(\tilde{u}_j) &= \tilde{u}_j \ , \\ T_2(\tilde{u}_j) &= 2\tilde{u}_j^2 - 1 \ , & T_3(\tilde{u}_j) &= 4\tilde{u}_j^3 - 3\tilde{u}_j \ . \end{aligned}$$

By using the substitution $\sin(\chi_j) = \tilde{u}_j$, and using $(1-\sin(\chi_j)^2)^{1/2} = \cos(\chi_j)$ and $\mathrm{d}\sin(\chi_j) = \cos(\chi_j)\mathrm{d}\chi_j$ the expressions for $A_{m,j}$ evaluate as

$$A_{m,j} = \frac{2}{\pi}\int_{-\pi/2}^{\pi/2} |\sin(\chi_j)|\sin(\chi_j)\; T_m\Big(\sin(\chi_j)\Big)\; d\chi_j \;.$$

For $m = 0, 2$, the functions to be integrated are odd, thus $A_{0,j} = A_{2,j} = 0$, while for $m = 1, 3$ the coefficients evaluate to $A_{1,j} = 8/3\pi$, and $A_{3,j} = 8/15\pi$. Substituting these coefficients into equation (4.26), it is found that

$$\begin{aligned} C_{d,j}U_j^2\sum_{m=0}^{3} A_{m,j}T_m(\tilde{u}_j) &= C_{d,j}U_j^2\left[\frac{8}{3\pi}\tilde{u}_j + \frac{8}{15\pi}(4\tilde{u}_j^3 - 3\tilde{u}_j)\right] \;, \\ &= \frac{16}{15\pi}C_{d,j}U_j\Big[u_j + \frac{2u_j^3}{U_j^2}\Big] \;. \end{aligned}$$

Now, the velocity is replaced with its harmonic truncation. This yields

$$\begin{aligned} \frac{16}{15\pi}C_{d,j}U_j\Big[u_j + \frac{2u_j^3}{U_j^2}\Big] = \frac{16}{15\pi}C_{d,j}U_j\times \\ \Big[\Big(\mathcal{U}_{0,j} + \frac{1}{2}(\mathcal{U}_{1,j}e^{-i\sigma t} + \mathcal{U}_{1,j}^{\dagger}e^{i\sigma t}) + \frac{1}{2}(\mathcal{U}_{2,j}e^{-2i\sigma t} + \mathcal{U}_{2,j}^{\dagger}e^{2i\sigma t})\Big) + \\ + \frac{2}{U_j^2}\Big(\mathcal{U}_{0,j} + \frac{1}{2}(\mathcal{U}_{1,j}e^{-i\sigma t} + \mathcal{U}_{1,j}^{\dagger}e^{i\sigma t}) + \frac{1}{2}(\mathcal{U}_{2,j}e^{-2i\sigma t} + \mathcal{U}_{2,j}^{\dagger}e^{2i\sigma t})\Big)^3\Big] \;. \end{aligned}$$

This expression is expanded using basic algebra. Only retaining the harmonic components with frequency equal to or lower than quarter diurnal and reordering the terms yields

$$\begin{aligned} C_{d,j}|u_j|u_j \approx \frac{16}{15\pi}C_{d,j}U_j\times \\ \Big[\Big(1 + \frac{2}{U_j^2}(\;|\mathcal{U}_{0,j}|^2 + \frac{3}{2}|\mathcal{U}_{1,j}|^2 + \frac{3}{2}|\mathcal{U}_{2,j}|^2)\Big)\mathcal{U}_{0,j} + \frac{3}{2}\mathcal{R}(\mathcal{U}_{2,j}\mathcal{U}_{1,j}^{\dagger 2}) + \\ + \Big(1 + \frac{2}{U_j^2}(3|\mathcal{U}_{0,j}|^2 + \frac{3}{4}|\mathcal{U}_{1,j}|^2 + \frac{3}{2}|\mathcal{U}_{2,j}|^2)\Big)\mathcal{R}(\mathcal{U}_{1,j}e^{-i\sigma t}) + 6\mathcal{R}(\mathcal{U}_{0,j}\mathcal{U}_{1,j}^{\dagger}\mathcal{U}_{2,j}e^{-i\sigma t}) + \\ + \Big(1 + \frac{2}{U_j^2}(3|\mathcal{U}_{0,j}|^2 + \frac{3}{2}|\mathcal{U}_{1,j}|^2 + \frac{3}{4}|\mathcal{U}_{2,j}|^2)\Big)\mathcal{R}(\mathcal{U}_{2,j}e^{-2i\sigma t}) + 3\mathcal{R}(\mathcal{U}_{0,j}\mathcal{U}_{1,j}^2e^{-2i\sigma t})\Big] \;, \\ = \quad \underline{\lambda}_{0,j}\mathcal{U}_{0,j} \;+\; \underline{\lambda}_{c0,j}\mathcal{R}(\mathcal{U}_{2,j}\mathcal{U}_{1,j}^{\dagger 2}) \;+ \\ + \underline{\lambda}_{1,j}\mathcal{R}(\mathcal{U}_{1,j}e^{-i\sigma t}) \;+\; \underline{\lambda}_{c1,j}\mathcal{R}(\mathcal{U}_{0,j}\mathcal{U}_{2,j}\mathcal{U}_{1,j}^{\dagger}e^{-i\sigma t}) \;+ \\ + \underline{\lambda}_{2,j}\mathcal{R}(\mathcal{U}_{2,j}e^{-2i\sigma t}) + \;\underline{\lambda}_{c2,j}\mathcal{R}(\mathcal{U}_{0,j}\mathcal{U}_{1,j}^2e^{-2i\sigma t}) \;. \end{aligned}$$

As was described in the main body of text, the values for the space dependent linearized friction coefficients are averaged over each channel, i.e.

$$\lambda_{m,j} \equiv \frac{1}{l_{b,j}}\int_{l_{r,j}}^{l_{o,j}} \underline{\lambda}_{m,j}\; dx \;, \qquad\qquad m = \{0,\; 1,\; 2,\; c0,\; c1,\; c2\} \;. \tag{4.27}$$

Momentum equation

With a harmonic expansion available for the quadratic bottom stress, the harmonic truncation is applied to the momentum equation. First, the momentum equation, Eqn. (4.2a), is rewritten as

$$(h_j+\eta_j)\left\{\frac{\partial u_j}{\partial t}+\frac{\partial}{\partial x}\left[\frac{1}{2}u_j^2+g\eta_j\right]\right\}=-C_{d,j}|u_j|u_j\ .$$

Substituting the harmonic truncation, Eqn. (4.25), and grouping the terms by frequency yields equations for the various harmonic components as.

Residual:

$$\begin{aligned}
&(h_j+\mathcal{N}_{0,j})\left\{\qquad\qquad \frac{d}{dx}\left[\frac{1}{2}\mathcal{U}_{0,j}^2+\frac{1}{4}\mathcal{U}_{1,j}\mathcal{U}_{1,j}^\dagger+\frac{1}{4}\mathcal{U}_{2,j}\mathcal{U}_{2,j}^\dagger+g\mathcal{N}_{0,j}\right]\right\}+\\
&\quad+\frac{1}{2}\mathcal{N}_{1,j}\left\{\quad\frac{1}{2}i\sigma\mathcal{U}_{1,j}^\dagger+\frac{d}{dx}\left[\frac{1}{2}\mathcal{U}_{0,j}\mathcal{U}_{1,j}^\dagger+\frac{1}{4}\mathcal{U}_{1,j}\mathcal{U}_{2,j}^\dagger+\frac{1}{2}g\mathcal{N}_{1,j}^\dagger\right]\right\}+\\
&\quad+\frac{1}{2}\mathcal{N}_{1,j}^\dagger\left\{-\frac{1}{2}i\sigma\mathcal{U}_{1,j}+\frac{d}{dx}\left[\frac{1}{2}\mathcal{U}_{0,j}\mathcal{U}_{1,j}+\frac{1}{4}\mathcal{U}_{1,j}^\dagger\mathcal{U}_{2,j}+\frac{1}{2}g\mathcal{N}_{1,j}\right]\right\}+\\
&\quad+\frac{1}{2}\mathcal{N}_{2,j}\left\{\quad i\sigma\mathcal{U}_{2,j}^\dagger+\frac{d}{dx}\left[\frac{1}{8}\mathcal{U}_{1,j}^{\dagger 2}+\frac{1}{2}\mathcal{U}_{0,j}\mathcal{U}_{2,j}^\dagger+\frac{1}{2}g\mathcal{N}_{2,j}^\dagger\right]\right\}+\\
&\quad+\frac{1}{2}\mathcal{N}_{2,j}^\dagger\left\{-i\sigma\mathcal{U}_{2,j}+\frac{d}{dx}\left[\frac{1}{8}\mathcal{U}_{1,j}^2+\frac{1}{2}\mathcal{U}_{0,j}\mathcal{U}_{2,j}+\frac{1}{2}g\mathcal{N}_{2,j}\right]\right\}=\\
&\qquad\qquad=-\lambda_{0,j}\mathcal{U}_{0,j}-\frac{\lambda_{c0,j}}{2}(\mathcal{U}_{2,j}\mathcal{U}_{1,j}^{\dagger 2}+\mathcal{U}_{2,j}^\dagger\mathcal{U}_{1,j}^2)\ ,
\end{aligned}\tag{4.28}$$

Semi-diurnal:

$$\begin{aligned}
&(h_j+\mathcal{N}_{0,j})\left\{-i\sigma\mathcal{U}_{1,j}+\frac{d}{dx}\left[\mathcal{U}_{0,j}\mathcal{U}_{1,j}+\frac{1}{2}\mathcal{U}_{1,j}^\dagger\mathcal{U}_{2,j}+g\mathcal{N}_{1,j}\right]\right\}+\\
&\quad+\mathcal{N}_{1,j}\left\{\qquad\qquad\frac{d}{dx}\left[\frac{1}{2}\mathcal{U}_{0,j}^2+\frac{1}{4}\mathcal{U}_{1,j}\mathcal{U}_{1,j}^\dagger+\frac{1}{4}\mathcal{U}_{2,j}\mathcal{U}_{2,j}^\dagger+g\mathcal{N}_{0,j}\right]\right\}+\\
&\quad+\mathcal{N}_{1,j}^\dagger\left\{-2i\sigma\mathcal{U}_{2,j}+\frac{d}{dx}\left[\frac{1}{8}\mathcal{U}_{1,j}^2+\frac{1}{2}\mathcal{U}_{0,j}\mathcal{U}_{2,j}+\frac{1}{2}g\mathcal{N}_{2,j}\right]\right\}+\\
&\quad+\mathcal{N}_{2,j}\left\{\quad i\sigma\mathcal{U}_{1,j}^\dagger+\frac{d}{dx}\left[\frac{1}{2}\mathcal{U}_{0,j}\mathcal{U}_{1,j}^\dagger+\frac{1}{4}\mathcal{U}_{1,j}\mathcal{U}_{2,j}^\dagger+\frac{1}{2}g\mathcal{N}_{1,j}^\dagger\right]\right\}+\\
&\quad+\mathcal{N}_{2,j}^\dagger\left\{\qquad\qquad\frac{d}{dx}\left[\frac{1}{2}\mathcal{U}_{1,j}\mathcal{U}_{2,j}\right]\right\}=\\
&\qquad\qquad=-\lambda_{1,j}\mathcal{U}_{1,j}-\lambda_{c1,j}\mathcal{U}_{0,j}\mathcal{U}_{2,j}\mathcal{U}_{1,j}^\dagger\ ,
\end{aligned}\tag{4.29}$$

Quarter diurnal:

$$
\begin{aligned}
&(h_j+\mathcal{N}_{0,j})\Big\{ -2i\sigma\mathcal{U}_{2,j}+\frac{d}{dx}\Big[\frac{1}{4}\mathcal{U}_{1,j}^2+\mathcal{U}_{0,j}\mathcal{U}_{2,j}+g\mathcal{N}_{2,j}\Big]\Big\}+\\
&\quad+\mathcal{N}_{1,j}\Big\{ -\frac{i\sigma}{2}\mathcal{U}_{1,j}+\frac{d}{dx}\Big[\frac{1}{2}\mathcal{U}_{0,j}\mathcal{U}_{1,j}+\frac{1}{4}\mathcal{U}_{1,j}^{\dagger}\mathcal{U}_{2,j}+\frac{1}{2}g\mathcal{N}_{1,j}\Big]\Big\}+\\
&\quad+\mathcal{N}_{1,j}^{\dagger}\Big\{ \frac{d}{dx}\Big[\frac{1}{4}\mathcal{U}_{1,j}\mathcal{U}_{2,j}\Big]\Big\}+\\
&\quad+\mathcal{N}_{2,j}\Big\{ \frac{d}{dx}\Big[\frac{1}{2}\mathcal{U}_{0,j}^2+\frac{1}{4}\mathcal{U}_{1,j}^{\dagger}\mathcal{U}_{1,j}+\frac{1}{4}\mathcal{U}_{2,j}^{\dagger}\mathcal{U}_{2,j}+g\mathcal{N}_{0,j}\Big]\Big\}+\\
&\quad+\mathcal{N}_{2,j}^{\dagger}\Big\{ \frac{d}{dx}\Big[\frac{1}{4}\mathcal{U}_{2,j}^2\Big]\Big\}=\\
&\qquad=-\lambda_{2,j}\mathcal{U}_{2,j}-\lambda_{c2,j}\mathcal{U}_{0,j}\mathcal{U}_{1,j}^2\ .
\end{aligned}
\tag{4.30}
$$

Continuity equation

Substituting the harmonic truncation, Eqn. (4.25), in the continuity equation, Eqn. (4.2b), yields for the various harmonic components

Residual:

$$
\begin{aligned}
&\frac{d}{dx}\Big[b_j h_j\mathcal{U}_{0,j}\Big]+\frac{d}{dx}\Big[b_j\mathcal{N}_{0,j}\mathcal{U}_{0,j}\Big]+\\
&+\frac{d}{dx}\Big[b_j\Big(\frac{1}{4}(\mathcal{N}_{1,j}\mathcal{U}_{1,j}^{\dagger}+\mathcal{N}_{1,j}^{\dagger}\mathcal{U}_{1,j})+\frac{1}{4}(\mathcal{N}_{2,j}\mathcal{U}_{2,j}^{\dagger}+\mathcal{N}_{2,j}^{\dagger}\mathcal{U}_{2,j})\Big)\Big]=0\ ,
\end{aligned}
\tag{4.31}
$$

Semi-diurnal:

$$
\begin{aligned}
&\frac{d}{dx}\Big[b_j h_j\mathcal{U}_{1,j}\Big]+\\
&+\frac{d}{dx}\Big[b_j\Big((\mathcal{N}_{0,j}\mathcal{U}_{1,j}+\mathcal{N}_{1,j}\mathcal{U}_{0,j})+\frac{1}{2}(\mathcal{N}_{1,j}^{\dagger}\mathcal{U}_{2,j}+\mathcal{N}_{2,j}\mathcal{U}_{1,j}^{\dagger})\Big)\Big]=i\sigma b_j\mathcal{N}_{1,j}\ ,
\end{aligned}
\tag{4.32}
$$

Quarter diurnal:

$$
\begin{aligned}
&\frac{d}{dx}\Big[b_j h_j\mathcal{U}_{2,j}\Big]+\\
&+\frac{d}{dx}\Big[b_j\Big((\mathcal{N}_{0,j}\mathcal{U}_{2,j}+\mathcal{N}_{2,j}\mathcal{U}_{0,j})+\frac{1}{2}\mathcal{N}_{1,j}\mathcal{U}_{1,j}\Big)\Big]=2i\sigma b_j\mathcal{N}_{2,j}\ .
\end{aligned}
\tag{4.33}
$$

Boundary conditions

Using the harmonic truncation on the boundary conditions transforms them for the various harmonic components to

Residual:

$$
\begin{aligned}
&\mathcal{N}_{0,j} = 0 \text{ , at } x = l_{o,j} \text{ , } j \in O \text{ ,} \\
&b_j h_j \mathcal{U}_{0,j} + b_j \mathcal{N}_{0,j} \mathcal{U}_{0,j} + \frac{b_j}{4}(\mathcal{N}_{1,j}\mathcal{U}_{1,j}^{\dagger} + \mathcal{N}_{1,j}^{\dagger}\mathcal{U}_{1,j}) + \\
&\qquad + \frac{b_j}{4}(\mathcal{N}_{2,j}\mathcal{U}_{2,j}^{\dagger} + \mathcal{N}_{2,j}^{\dagger}\mathcal{U}_{2,j}) = Q_{0,j} \text{ , at } x = l_{r,j} \text{ , } j \in R \text{ ,} \\
&g\mathcal{N}_{0,j} + \frac{\mu}{2}\mathcal{U}_{0,j}^2 + \frac{\mu}{4}\mathcal{U}_{1,j}\mathcal{U}_{1,j}^{\dagger} + \frac{\mu}{4}\mathcal{U}_{2,j}\mathcal{U}_{2,j}^{\dagger} = \\
&\qquad = g\mathcal{N}_{0,k} + \frac{\mu}{2}\mathcal{U}_{0,k}^2 + \frac{\mu}{4}\mathcal{U}_{1,k}\mathcal{U}_{1,k}^{\dagger} + \frac{\mu}{4}\mathcal{U}_{2,k}\mathcal{U}_{2,k}^{\dagger} \text{ , } \forall j,k \in J_\nu \text{ , } \nu \in V \text{ ,} \\
&\sum_{j\in J_\nu} b_j h_j \mathcal{U}_{0,j} = -\sum_{j\in J_\nu} b_j \mathcal{N}_{0,j}\mathcal{U}_{0,j} + \\
&\qquad - \sum_{j\in J_\nu} \frac{b_j}{4}\Big(\mathcal{N}_{1,j}\mathcal{U}_{1,j}^{\dagger} + \mathcal{N}_{1,j}^{\dagger}\mathcal{U}_{1,j} + \mathcal{N}_{2,j}\mathcal{U}_{2,j}^{\dagger} + \mathcal{N}_{2,j}^{\dagger}\mathcal{U}_{2,j}\Big) \text{ ,}
\end{aligned}
\tag{4.34}
$$

Semi-diurnal:

$$
\begin{aligned}
&\mathcal{N}_{1,j} = N_j e^{i\phi_j} \text{ , at } x = l_{o,j} \text{ , } j \in O \text{ ,} \\
&h_j \mathcal{U}_{1,j} + \Big(\mathcal{N}_{0,j}\mathcal{U}_{1,j} + \mathcal{N}_{1,j}\mathcal{U}_{0,j}\Big) + \\
&\qquad + \frac{1}{2}\Big(\mathcal{N}_{1,j}^{\dagger}\mathcal{U}_{2,j} + \mathcal{N}_{2,j}\mathcal{U}_{1,j}^{\dagger}\Big) = 0 \text{ , at } x = l_{r,j} \text{ , } j \in R \text{ ,} \\
&g\mathcal{N}_{1,j} + \mu\mathcal{U}_{0,j}\mathcal{U}_{1,j} + \frac{\mu}{2}\mathcal{U}_{2,j}\mathcal{U}_{1,j}^{\dagger} = \\
&\qquad = g\mathcal{N}_{1,k} + \mu\mathcal{U}_{0,k}\mathcal{U}_{1,k} + \frac{\mu}{2}\mathcal{U}_{2,k}\mathcal{U}_{1,k}^{\dagger}, \ \forall j,k \in J_\nu \text{ , } \nu \in V \text{ ,} \\
&\sum_{j\in J_\nu} b_j h_j \mathcal{U}_{1,j} = -\sum_{j\in J_\nu} b_j \Big(\mathcal{N}_{0,j}\mathcal{U}_{1,j} + \mathcal{N}_{1,j}\mathcal{U}_{0,j}\Big) + \\
&\qquad - \sum_{j\in J_\nu} \frac{b_j}{2}\Big(\mathcal{N}_{1,j}^{\dagger}\mathcal{U}_{2,j} + \mathcal{N}_{2,j}\mathcal{U}_{1,j}^{\dagger}\Big) \text{ ,}
\end{aligned}
\tag{4.35}
$$

Quarter diurnal:

$$
\begin{aligned}
&\mathcal{N}_{2,j} = 0 \text{ , at } x = l_{o,j} \text{ , } j \in O \text{ ,} \\
&h_j \mathcal{U}_{2,j} + \Big((\mathcal{N}_{0,j}\mathcal{U}_{2,j} + \mathcal{N}_{2,j}\mathcal{U}_{0,j}) + \frac{1}{2}\mathcal{N}_{1,j}\mathcal{U}_{1,j} \Big) = \\
&\qquad = 0 \text{ , at } x = l_{r,j} \text{ , } j \in R \text{ ,} \\
&g\mathcal{N}_{2,j} + \frac{\mu}{4}\mathcal{U}_{1,j}^2 + \mu \mathcal{U}_{0,j}\mathcal{U}_{2,j} = \\
&\qquad = g\mathcal{N}_{2,k} + \frac{\mu}{4}\mathcal{U}_{1,k}^2 + \mu \mathcal{U}_{0,k}\mathcal{U}_{2,k}, \ \forall j,k \in J_\nu \text{ , } \nu \in V \text{ ,} \\
&\sum_{j \in J_\nu} b_j h_j \mathcal{U}_{2,j} = - \sum_{j \in J_\nu} b_j \Big((\mathcal{N}_{0,j}\mathcal{U}_{2,j} + \mathcal{N}_{2,j}\mathcal{U}_{0,j}) + \frac{1}{2}\mathcal{N}_{1,j}\mathcal{U}_{1,j} \Big) \text{ .}
\end{aligned}
\tag{4.36}
$$

4.A.2 Scaling

To perform the perturbation analysis, the equations have to be made dimensionless. This is done by using representative scales, which read

$$
\begin{aligned}
\mathcal{U}_{n,j} &= V\widetilde{\mathcal{U}}_{n,j} \text{ ,} & \mathcal{N}_{n,j} &= N_1\widetilde{\mathcal{N}}_{n,j} \text{ ,} & h_j &= h_1\widetilde{h}_j \text{ ,} \\
x &= L_t\widetilde{x} \text{ ,} & t &= \sigma^{-1}\widetilde{t} \text{ ,} & b_j &= b_{0,1}\widetilde{b}_j \text{ ,}
\end{aligned}
\tag{4.37}
$$

where $V = \varepsilon c$ is a velocity scale ($\varepsilon \equiv N_1/h_1$ and $c = \sqrt{gh_1}$ the shallow water wave phase speed), N_1 is the forcing amplitude in the first channel, h_1 is the depth of the first channel, $L_t = c/\sigma$ is the wavelength of the frictionless tidal wave in a channel with depth h_1, σ is the angular tidal frequency, and $b_{0,1}$ is the width at the sea boundary of the first channel. The dimensions and tidal amplitude of the first channel are considered to be representative for the estuarine network. The subscript asterisks denote dimensionless quantities.
Introducing the scales from Eqn. (4.37) to Eqns. (4.28)–(4.36), yields equations for the dimensionless quantities. As these equations are very similar to Eqns. (4.28)–(4.36), they are only presented here for the residual component.

Momentum equation:

$$
\begin{aligned}
&(\widetilde{h}_j+\varepsilon\widetilde{\mathcal{N}}_{0,j})\Big\{\qquad\qquad \frac{d}{d\widetilde{x}}\Big[\frac{\varepsilon}{2}\widetilde{\mathcal{U}}_{0,j}^2+\frac{\varepsilon}{4}\widetilde{\mathcal{U}}_{1,j}\widetilde{\mathcal{U}}_{1,j}^\dagger+\frac{\varepsilon}{4}\widetilde{\mathcal{U}}_{2,j}\widetilde{\mathcal{U}}_{2,j}^\dagger+\widetilde{\mathcal{N}}_{0,j}\Big]\Big\}\\
&\quad+\frac{\varepsilon}{2}\widetilde{\mathcal{N}}_{1,j}\Big\{\quad\frac{1}{2}i\,\widetilde{\mathcal{U}}_{1,j}^\dagger+\frac{d}{d\widetilde{x}}\Big[\frac{\varepsilon}{2}\widetilde{\mathcal{U}}_{0,j}\widetilde{\mathcal{U}}_{1,j}^\dagger+\frac{\varepsilon}{4}\widetilde{\mathcal{U}}_{1,j}\widetilde{\mathcal{U}}_{2,j}^\dagger+\frac{1}{2}\widetilde{\mathcal{N}}_{1,j}^\dagger\Big]\Big\}+\\
&\quad+\frac{\varepsilon}{2}\widetilde{\mathcal{N}}_{1,j}^\dagger\Big\{-\frac{1}{2}i\,\widetilde{\mathcal{U}}_{1,j}+\frac{d}{d\widetilde{x}}\Big[\frac{\varepsilon}{2}\widetilde{\mathcal{U}}_{0,j}\widetilde{\mathcal{U}}_{1,j}+\frac{\varepsilon}{4}\widetilde{\mathcal{U}}_{1,j}^\dagger\widetilde{\mathcal{U}}_{2,j}+\frac{1}{2}\widetilde{\mathcal{N}}_{1,j}\Big]\Big\}+\\
&\quad+\frac{\varepsilon}{2}\widetilde{\mathcal{N}}_{2,j}\Big\{\qquad i\,\widetilde{\mathcal{U}}_{2,j}^\dagger+\frac{d}{d\widetilde{x}}\Big[\frac{\varepsilon}{8}\widetilde{\mathcal{U}}_{1,j}^{\dagger 2}+\frac{\varepsilon}{2}\widetilde{\mathcal{U}}_{0,j}\widetilde{\mathcal{U}}_{2,j}^\dagger+\frac{1}{2}\widetilde{\mathcal{N}}_{2,j}^\dagger\Big]\Big\}+\\
&\quad+\frac{\varepsilon}{2}\widetilde{\mathcal{N}}_{2,j}^\dagger\Big\{\quad-i\,\widetilde{\mathcal{U}}_{2,j}+\frac{d}{d\widetilde{x}}\Big[\frac{\varepsilon}{8}\widetilde{\mathcal{U}}_{1,j}^2+\frac{\varepsilon}{2}\widetilde{\mathcal{U}}_{0,j}\widetilde{\mathcal{U}}_{2,j}+\frac{1}{2}\widetilde{\mathcal{N}}_{2,j}\Big]\Big\}=\\
&\qquad\qquad=-\widetilde{\lambda}_{0,j}\widetilde{\mathcal{U}}_{0,j}-\frac{\widetilde{\lambda}_{c0,j}}{2}(\widetilde{\mathcal{U}}_{2,j}\widetilde{\mathcal{U}}_{1,j}^{\dagger 2}+\widetilde{\mathcal{U}}_{2,j}^\dagger\widetilde{\mathcal{U}}_{1,j}^2)\ ,
\end{aligned}
\tag{4.38}
$$

Continuity equation:

$$
\begin{aligned}
&\frac{d}{d\widetilde{x}}\Big[\widetilde{b}_j\widetilde{h}_j\widetilde{\mathcal{U}}_{0,j}\Big]=-\frac{d}{d\widetilde{x}}\Big[\varepsilon\widetilde{b}_j\widetilde{\mathcal{N}}_{0,j}\widetilde{\mathcal{U}}_{0,j}\Big]+\\
&\qquad-\frac{d}{d\widetilde{x}}\Big[\frac{\varepsilon\widetilde{b}_j}{4}\Big(\widetilde{\mathcal{N}}_{1,j}\widetilde{\mathcal{U}}_{1,j}^\dagger+\widetilde{\mathcal{N}}_{1,j}^\dagger\widetilde{\mathcal{U}}_{1,j}+\widetilde{\mathcal{N}}_{2,j}\widetilde{\mathcal{U}}_{2,j}^\dagger+\widetilde{\mathcal{N}}_{2,j}^\dagger\widetilde{\mathcal{U}}_{2,j}\Big)\Big]\ ,
\end{aligned}
\tag{4.39}
$$

Boundary conditions:

$$
\begin{aligned}
&\widetilde{\mathcal{N}}_{0,j}=0\ ,\ \text{at}\ \widetilde{x}=\widetilde{l}_{o,j}\ ,\ j\in O\ ,\\
&\widetilde{b}_j\widetilde{h}_j\widetilde{\mathcal{U}}_{0,j}+\varepsilon\widetilde{b}_j\Big(\widetilde{\mathcal{N}}_{0,j}\widetilde{\mathcal{U}}_{0,j}+\frac{1}{4}(\widetilde{\mathcal{N}}_{1,j}\widetilde{\mathcal{U}}_{1,j}^\dagger+\widetilde{\mathcal{N}}_{1,j}^\dagger\widetilde{\mathcal{U}}_{1,j})\Big)+\\
&\qquad+\frac{\varepsilon\widetilde{b}_j}{4}\Big(\widetilde{\mathcal{N}}_{2,j}\widetilde{\mathcal{U}}_{2,j}^\dagger+\widetilde{\mathcal{N}}_{2,j}^\dagger\widetilde{\mathcal{U}}_{2,j}\Big)=\frac{Q_{0,j}^{\mathrm{R}}}{b_{0,1}h_1V}\ ,\ \text{at}\ x_*=l_{r,j*}\ ,\ j\in R\ ,\\
&\widetilde{\mathcal{N}}_{0,j}+\frac{\varepsilon\mu}{2}\widetilde{\mathcal{U}}_{0,j}^2+\frac{\varepsilon\mu}{4}\widetilde{\mathcal{U}}_{1,j}\widetilde{\mathcal{U}}_{1,j}^\dagger+\frac{\varepsilon\mu}{4}\widetilde{\mathcal{U}}_{2,j}\widetilde{\mathcal{U}}_{2,j}^\dagger=\\
&\qquad=\widetilde{\mathcal{N}}_{0,k}+\frac{\varepsilon\mu}{2}\widetilde{\mathcal{U}}_{0,k}^2+\frac{\varepsilon\mu}{4}\widetilde{\mathcal{U}}_{1,k}\widetilde{\mathcal{U}}_{1,k}^\dagger+\frac{\varepsilon\mu}{4}\widetilde{\mathcal{U}}_{2,k}\widetilde{\mathcal{U}}_{2,k}^\dagger\ ,\ \forall j,k\in J_\nu\ ,\ \nu\in V\ ,\\
&\sum_{j\in J_\nu}\widetilde{b}_j\widetilde{h}_j\widetilde{\mathcal{U}}_{0,j}=-\sum_{j\in J_\nu}\varepsilon\widetilde{b}_j\widetilde{\mathcal{N}}_{0,j}\widetilde{\mathcal{U}}_{0,j}+\\
&\qquad-\sum_{j\in J_\nu}\frac{\varepsilon\widetilde{b}_j}{4}\Big(\widetilde{\mathcal{N}}_{1,j}\widetilde{\mathcal{U}}_{1,j}^\dagger+\widetilde{\mathcal{N}}_{1,j}^\dagger\widetilde{\mathcal{U}}_{1,j}+\widetilde{\mathcal{N}}_{2,j}\widetilde{\mathcal{U}}_{2,j}^\dagger+\widetilde{\mathcal{N}}_{2,j}^\dagger\widetilde{\mathcal{U}}_{2,j}\Big)\ ,
\end{aligned}
\tag{4.40}
$$

where $\widetilde{\lambda}_{m,j}=\lambda_{m,j}/h_1\sigma$ are the scaled linearized friction coefficients.

4.A.3 Perturbation expansion

Next, the perturbation expansion is introduced, which expands the dimensionless state variables ($\widetilde{\mathcal{U}}_{n,j}$ and $\widetilde{\mathcal{N}}_{n,j}$) with the use of the small parameter ε as

$$\begin{aligned}\widetilde{\mathcal{U}}_{n,j} &= \widetilde{\mathcal{U}}^{(0)}_{n,j} + \varepsilon\widetilde{\mathcal{U}}^{(1)}_{n,j} + \text{h.o.t.}\ ,\\ \widetilde{\mathcal{N}}_{n,j} &= \widetilde{\mathcal{N}}^{(0)}_{n,j} + \varepsilon\widetilde{\mathcal{N}}^{(1)}_{n,j} + \text{h.o.t.}\ ,\end{aligned} \tag{4.41}$$

where h.o.t. stands for higher order terms. The expansion from Eqn. (4.41) is introduced to Eqn. (4.38) and the equivalent equations for the semi-diurnal and quarter diurnal component. Subsequently, all higher order terms (i.e. $\geq \mathcal{O}(\varepsilon^2)$) are dropped. Then, terms are grouped by their ordering in ε (i.e. all terms proportional to ε^0 and ε^1 are grouped together, respectively). This results in an ordered set of linear differential equations, which are solved consecutively. These equations are presented below.

Leading order ($\mathcal{O}(\varepsilon^0)$)

With some rewriting of the terms, the leading order momentum and continuity equations read

$$\begin{aligned}
\widetilde{\mathcal{U}}^{(0)}_{0,j} &= \frac{-\widetilde{h}_j}{\widetilde{\lambda}_{0,j}}\frac{d\widetilde{\mathcal{N}}^{(0)}_{0,j}}{d\widetilde{x}}\ , & 0 &= -\frac{1}{\widetilde{b}_j}\frac{d}{d\widetilde{x}}\left(\widetilde{b}_j\widetilde{h}_j\widetilde{\mathcal{U}}^{(0)}_{0,j}\right)\ ,\\
\widetilde{\mathcal{U}}^{(0)}_{1,j} &= \frac{-\widetilde{h}_j}{\widetilde{\lambda}_{1,j}-i\widetilde{h}_j}\frac{d\widetilde{\mathcal{N}}^{(0)}_{1,j}}{d\widetilde{x}}\ , & -i\widetilde{\mathcal{N}}^{(0)}_{1,j} &= -\frac{1}{\widetilde{b}_j}\frac{d}{d\widetilde{x}}\left(\widetilde{b}_j\widetilde{h}_j\widetilde{\mathcal{U}}^{(0)}_{1,j}\right)\ ,\\
\widetilde{\mathcal{U}}^{(0)}_{2,j} &= \frac{-\widetilde{h}_j}{\widetilde{\lambda}_{2,j}-2i\widetilde{h}_j}\frac{d\widetilde{\mathcal{N}}^{(0)}_{2,j}}{d\widetilde{x}}\ , & -2i\widetilde{\mathcal{N}}^{(0)}_{2,j} &= -\frac{1}{\widetilde{b}_j}\frac{d}{d\widetilde{x}}\left(\widetilde{b}_j\widetilde{h}_j\widetilde{\mathcal{U}}^{(0)}_{2,j}\right)\ .
\end{aligned} \tag{4.42}$$

Finally, the leading order boundary conditions are

$$\left.\begin{aligned}\widetilde{\mathcal{N}}^{(0)}_{0,j} &= 0\ ,\\ \widetilde{\mathcal{N}}^{(0)}_{1,j} &= \frac{N_j}{N_1}e^{i\phi_j}\ ,\\ \widetilde{\mathcal{N}}^{(0)}_{2,j} &= 0\ ,\end{aligned}\right\}\ \text{at } \widetilde{x}=\widetilde{l}_{o,j}\ ,\ j\in O\ , \tag{4.43a}$$

$$\left.\begin{aligned}\widetilde{b}_j\widetilde{h}_j\widetilde{\mathcal{U}}^{(0)}_{0,j} &= \frac{Q^{\mathrm{R}}_{0,j}}{b_{0,1}h_1V}\ ,\\ \widetilde{\mathcal{U}}^{(0)}_{1,j} &= 0\ ,\\ \widetilde{\mathcal{U}}^{(0)}_{2,j} &= 0\ ,\end{aligned}\right\}\ \text{at } \widetilde{x}=\widetilde{l}_{r,j}\ ,\ j\in R\ , \tag{4.43b}$$

$$\left.\begin{aligned} \widetilde{\mathcal{N}}_{0,j}^{(0)} &= \widetilde{\mathcal{N}}_{0,k}^{(0)} \ , \\ \widetilde{\mathcal{N}}_{1,j}^{(0)} &= \widetilde{\mathcal{N}}_{1,k}^{(0)} \ , \\ \widetilde{\mathcal{N}}_{2,j}^{(0)} &= \widetilde{\mathcal{N}}_{2,k}^{(0)} \ , \end{aligned}\right\} \forall j,k \in J_\nu \ , \ \nu \in V \ , \tag{4.43c}$$

$$\begin{aligned} \sum_{j\in J_\nu} \widetilde{b}_j \widetilde{h}_j \widetilde{\mathcal{U}}_{0,j}^{(0)} &= 0 \ , \\ \sum_{j\in J_\nu} \widetilde{b}_j \widetilde{h}_j \widetilde{\mathcal{U}}_{1,j}^{(0)} &= 0 \ , \\ \sum_{j\in J_\nu} \widetilde{b}_j \widetilde{h}_j \widetilde{\mathcal{U}}_{2,j}^{(0)} &= 0 \ . \end{aligned} \tag{4.43d}$$

Re-dimensionalizing Eqns. (4.42) and (4.43) yields Eqns. (4.14)–(4.16). Since there is no external M_4 forcing, the solution for the leading order quarter diurnal tide is equal to zero everywhere. This system describes the river flow ($\widetilde{\mathcal{U}}_0^{(0)}$ and $\widetilde{\mathcal{N}}_0^{(0)}$) and the semi-diurnal tidal flow ($\widetilde{\mathcal{U}}_1^{(0)}$ and $\widetilde{\mathcal{N}}_1^{(0)}$). The technique to obtain solutions for the residual and semi-diurnal component are outlined in the main body of text.

First order ($\mathcal{O}(\varepsilon^1)$)

The first order momentum and continuity equations read

$$\begin{aligned} \widetilde{\mathcal{U}}_{0,j}^{(1)} &= \frac{-\widetilde{h}_j}{\widetilde{\lambda}_{0,j}} \frac{d\widetilde{\mathcal{N}}_{0,j}^{(1)}}{d\widetilde{x}} + \frac{\widetilde{h}_j}{\widetilde{\lambda}_{0,j}} \widetilde{\mathcal{F}}_{0,j} \ , \\ \widetilde{\mathcal{U}}_{1,j}^{(1)} &= \frac{-\widetilde{h}_j}{\widetilde{\lambda}_{1,j} - i\widetilde{h}_j} \frac{d\widetilde{\mathcal{N}}_{1,j}^{(1)}}{d\widetilde{x}} + \frac{\widetilde{h}_j}{\widetilde{\lambda}_{1,j} - i\widetilde{h}_j} \widetilde{\mathcal{F}}_{1,j} \ , \\ \widetilde{\mathcal{U}}_{2,j}^{(1)} &= \frac{-\widetilde{h}_j}{\widetilde{\lambda}_{2,j} - 2i\widetilde{h}_j} \frac{d\widetilde{\mathcal{N}}_{2,j}^{(1)}}{d\widetilde{x}} + \frac{\widetilde{h}_j}{\widetilde{\lambda}_{2,j} - 2i\widetilde{h}_j} \widetilde{\mathcal{F}}_{2,j} \ , \end{aligned} \tag{4.44}$$

$$\begin{aligned} 0 &= -\frac{1}{\widetilde{b}_j} \frac{d}{d\widetilde{x}} \left(\widetilde{b}_j \widetilde{h}_j \widetilde{\mathcal{U}}_{0,j}^{(1)} + \widetilde{b}_j \widetilde{\mathcal{S}}_{0,j} \right) \ , \\ -i\widetilde{\mathcal{N}}_{1,j}^{(1)} &= -\frac{1}{\widetilde{b}_j} \frac{d}{d\widetilde{x}} \left(\widetilde{b}_j \widetilde{h}_j \widetilde{\mathcal{U}}_{1,j}^{(1)} + \widetilde{b}_j \widetilde{\mathcal{S}}_{1,j} \right) \ , \\ -2i\widetilde{\mathcal{N}}_{2,j}^{(1)} &= -\frac{1}{\widetilde{b}_j} \frac{d}{d\widetilde{x}} \left(\widetilde{b}_j \widetilde{h}_j \widetilde{\mathcal{U}}_{2,j}^{(1)} + \widetilde{b}_j \widetilde{\mathcal{S}}_{2,j} \right) \ . \end{aligned} \tag{4.45}$$

In Eqns. (4.44) and (4.45), the symbols $\widetilde{\mathcal{F}}_{n,j}$ and $\widetilde{\mathcal{S}}_{n,j}$ contain forcing terms from the momentum and continuity equation, respectively, for the corresponding har-

monic component. These equations read

$$\begin{aligned}
\widetilde{\mathcal{F}}_{0,j} &= -\frac{1}{2}\frac{d}{d\widetilde{x}}\Big(\widetilde{\mathcal{U}}_{0,j}^{(0)2} + \frac{1}{2}\widetilde{\mathcal{U}}_{1,j}^{(0)}\widetilde{\mathcal{U}}_{1,j}^{(0)\dagger}\Big) + \frac{\widetilde{\lambda}_{0,j}}{\widetilde{h}_j^2}\widetilde{\mathcal{N}}_{0,j}^{(0)}\widetilde{\mathcal{U}}_{0,j}^{(0)} + \\
&\quad + \frac{\widetilde{\lambda}_{1,j}}{4\widetilde{h}_j^2}\Big(\widetilde{\mathcal{N}}_{1,j}^{(0)}\widetilde{\mathcal{U}}_{2,j}^{(0)\dagger} + \widetilde{\mathcal{N}}_{2,j}^{(0)\dagger}\widetilde{\mathcal{U}}_{1,j}^{(0)}\Big) + \\
&\quad + \frac{\widetilde{\lambda}_{c0,j}}{2\widetilde{h}_j}\Big(\widetilde{\mathcal{U}}_{2,j}^{(1)}\widetilde{\mathcal{U}}_{1,j}^{(0)\dagger 2} + \widetilde{\mathcal{U}}_{2,j}^{(1)\dagger}\widetilde{\mathcal{U}}_{1,j}^{(0)2}\Big) \ , \\
\widetilde{\mathcal{F}}_{1,j} &= -\frac{d}{d\widetilde{x}}\Big(\widetilde{\mathcal{U}}_{0,j}^{(0)}\widetilde{\mathcal{U}}_{1,j}^{(0)}\Big) + \frac{\widetilde{\lambda}_{0,j}}{\widetilde{h}_j^2}\widetilde{\mathcal{N}}_{1,j}^{(0)}\widetilde{\mathcal{U}}_{0,j}^{(0)} + \frac{\widetilde{\lambda}_{1,j}}{\widetilde{h}_j^2}\widetilde{\mathcal{N}}_{0,j}^{(0)}\widetilde{\mathcal{U}}_{1,j}^{(0)} + \\
&\quad + \frac{\widetilde{\lambda}_{c1,j}}{\widetilde{h}_j}\widetilde{\mathcal{U}}_{0,j}^{(0)}\widetilde{\mathcal{U}}_{2,j}^{(1)}\widetilde{\mathcal{U}}_{1,j}^{(0)\dagger} \ , \\
\widetilde{\mathcal{F}}_{2,j} &= -\frac{1}{4}\frac{d}{d\widetilde{x}}\Big(\widetilde{\mathcal{U}}_{1,j}^{(0)2}\Big) + \frac{\widetilde{\lambda}_{1,j}}{2\widetilde{h}_j^2}\widetilde{\mathcal{N}}_{1,j}^{(0)}\widetilde{\mathcal{U}}_{1,j}^{(0)} + \frac{\widetilde{\lambda}_{c2,j}}{\widetilde{h}_j}\widetilde{\mathcal{U}}_{0,j}^{(0)}\widetilde{\mathcal{U}}_{1,j}^{(0)2} \ ,
\end{aligned} \tag{4.46}$$

$$\begin{aligned}
\widetilde{\mathcal{S}}_{0,j} &= \widetilde{\mathcal{N}}_{0,j}^{(0)}\widetilde{\mathcal{U}}_{0,j}^{(0)} + \frac{1}{4}\Big(\widetilde{\mathcal{N}}_{1,j}^{(0)}\widetilde{\mathcal{U}}_{1,j}^{(0)\dagger} + \widetilde{\mathcal{N}}_{1,j}^{(0)\dagger}\widetilde{\mathcal{U}}_{1,j}^{(0)}\Big) \ , \\
\widetilde{\mathcal{S}}_{1,j} &= \widetilde{\mathcal{N}}_{1,j}^{(0)}\widetilde{\mathcal{U}}_{0,j1}^{(0)} + \widetilde{\mathcal{N}}_{0,j}^{(0)}\widetilde{\mathcal{U}}_{1,j}^{(0)} \ , \\
\widetilde{\mathcal{S}}_{2,j} &= \frac{1}{2}\widetilde{\mathcal{N}}_{1,j}^{(0)}\widetilde{\mathcal{U}}_{1,j}^{(0)} \ .
\end{aligned} \tag{4.47}$$

Finally, the first order boundary conditions are

$$\left.\begin{aligned}
\widetilde{\mathcal{N}}_{0,j}^{(1)} &= 0 \ , \\
\widetilde{\mathcal{N}}_{1,j}^{(1)} &= 0 \ , \\
\widetilde{\mathcal{N}}_{2,j}^{(1)} &= 0 \ ,
\end{aligned}\right\} \text{at } \widetilde{x} = \widetilde{l}_{o,j} \ , \ j \in O \ , \tag{4.48a}$$

$$\left.\begin{aligned}
\widetilde{h}_j\widetilde{\mathcal{U}}_{0,j}^{(1)} &= -\widetilde{\mathcal{N}}_{0,j}^{(0)}\widetilde{\mathcal{U}}_{0,j}^{(0)} \ , \\
\widetilde{h}_j\widetilde{\mathcal{U}}_{1,j}^{(1)} &= -\widetilde{\mathcal{N}}_{1,j}^{(0)}\widetilde{\mathcal{U}}_{0,j}^{(0)} \ , \\
\widetilde{h}_j\widetilde{\mathcal{U}}_{2,j}^{(1)} &= 0 \ ,
\end{aligned}\right\} \text{at } \widetilde{x} = \widetilde{l}_{r,j} \ , \ j \in R \ , \tag{4.48b}$$

$$\left.\begin{aligned}
\widetilde{\mathcal{N}}_{0,j}^{(1)} + \frac{\mu}{2}\widetilde{\mathcal{D}}_{0,j} &= \widetilde{\mathcal{N}}_{0,k}^{(1)} + \frac{\mu}{2}\widetilde{\mathcal{D}}_{0,k} \ , \\
\widetilde{\mathcal{N}}_{1,j}^{(1)} + \frac{\mu}{2}\widetilde{\mathcal{D}}_{1,j} &= \widetilde{\mathcal{N}}_{1,k}^{(1)} + \frac{\mu}{2}\widetilde{\mathcal{D}}_{1,k} \ , \\
\widetilde{\mathcal{N}}_{2,j}^{(1)} + \frac{\mu}{2}\widetilde{\mathcal{D}}_{2,j} &= \widetilde{\mathcal{N}}_{2,k}^{(1)} + \frac{\mu}{2}\widetilde{\mathcal{D}}_{2,k} \ ,
\end{aligned}\right\} \forall j,k \in J_\nu \ , \ \nu \in V \ , \tag{4.48c}$$

$$\begin{aligned}
\sum_{j\in J_\nu} \widetilde{b}_j \widetilde{h}_j \widetilde{\mathcal{U}}_{0,j}^{(1)} &= -\sum_{j\in J_\nu} \widetilde{b}_j \widetilde{\mathcal{S}}_{0,j} \ , \\
\sum_{j\in J_\nu} \widetilde{b}_j \widetilde{h}_j \widetilde{\mathcal{U}}_{1,j}^{(1)} &= -\sum_{j\in J_\nu} \widetilde{b}_j \widetilde{\mathcal{S}}_{1,j} \ , \\
\sum_{j\in J_\nu} \widetilde{b}_j \widetilde{h}_j \widetilde{\mathcal{U}}_{2,j}^{(1)} &= -\sum_{j\in J_\nu} \widetilde{b}_j \widetilde{\mathcal{S}}_{2,j} \ ,
\end{aligned} \tag{4.48d}$$

with the dynamic pressure for each harmonic component as

$$\begin{aligned}
\widetilde{\mathcal{D}}_{0,j} &= \widetilde{\mathcal{U}}_{0,j}^{(0)2} + \frac{1}{2}\widetilde{\mathcal{U}}_{1,j}^{(0)}\widetilde{\mathcal{U}}_{1,j}^{(0)\dagger} \ , \\
\widetilde{\mathcal{D}}_{1,j} &= 2\widetilde{\mathcal{U}}_{0,j}^{(0)}\widetilde{\mathcal{U}}_{1,j}^{(0)} \ , \\
\widetilde{\mathcal{D}}_{2,j} &= \frac{1}{2}\widetilde{\mathcal{U}}_{1,j}^{(0)2} \ .
\end{aligned} \tag{4.49}$$

Eqns. (4.44)–(4.49) yield Eqns. (4.17a)–(4.19) and Eqns. (4.22) and (4.23) after redimensionalizing. These equations describe residual flow and sea surface elevation due to nonlinear shallow water effects, the internally generated M_2 tide due to river-tide interactions and the M_4 tide computed due to nonlinear terms in the shallow water equations. The solutions to these equations are again presented in the main body of text.

Chapter 5

The effect of intertidal areas on velocity in tidal channels; momentum sink and overtopping

5.1 Introduction

Shallow inland seas (e.g. the Wadden Sea, a marginal sea in the south North Sea) and estuaries (e.g. the Ems estuary at the Dutch-German border) with strong tidal currents are often characterized by deep channels with adjacent tidal flats, which fall dry during part of the tidal cycle. These tidal flats have long been known to have a strong influence on the hydrodynamics, by providing a source for overtides of the principal tidal component. Overtides result in asymmetric velocity and sea surface curves (e.g. Boon & Byrne, 1981; Speer & Aubrey, 1985; Friedrichs & Aubrey, 1994; Brown & Davies, 2010). These asymmetries are in turn important e.g. for determining net sediment transport and morphological stability of a tidal channel. Two overtide generating processes associated with tidal flats are the temporary storage of mass and the dissipation of momentum on the tidal flats, as were identified by e.g. Dronkers (1964) and Speer (1984). However, while mass storage has received quite some attention in the literature, this is not the case for momentum sink. Speer & Aubrey (1985) developed a numerical cross-sectionally average (1-D) model, which solves the nonlinear shallow water equations in a short tidal channel, i.e. the ratio of the basin length to the local tidal wavelength is small. The model parametrically accounted for mass storage on the adjacent tidal flats. They found that in the absence of tidal flats, the maximum flood currents are stronger than the ebb currents (flood dominance). The storage of water on the tidal flats on the other hand produces ebb dominance. Friedrichs & Aubrey (1988) corroborated the earlier findings that water storage on tidal flats favours ebb dominance. They considered a broad range of tidal flat widths and tidal sea surface amplitudes. Recently, Ridderinkhof *et al.* (2014) extended these results to include channels of arbitrary length. They found that for

increasing length of the channels, tidal flats favour flood currents.
A limitation of all previous studies is that they only considered linearly sloping flats. In nature, wide flats are observed (see for example Dronkers, 2005), which feature a range of shapes from concave to convex (Friedrichs & Aubrey, 1996; Friedrichs, 2011). Moreover, they assumed the local width of the tidal flats to be a constant fraction of the the channel width. However, many basins, such as the Wadden Sea, show different along-channel distributions of the tidal flats (cf. van Straaten & Kuenen, 1957; van Prooijen & Wang, 2013). Additionally, it is often observed that two parallel channels are separated by a tidal flat during low water, while they are connected during high water. This occurs e.g. in the Ems estuary, at the Dutch-German border and in the Yangtze Estuary, China. The overtopping of water from one channel to another has been considered by Hamilton (1990) for the Columbia River estuary (USA). He found that overtopping enhances currents in one channel at the expanse of those in the adjacent channel. In the Columbia River estuary, overtopping occurs naturally. In contrast, in the Ems estuary and the Yangtze Estuary man-made dams (partially) prevent the exchange of water. Thus, it is important to investigate what the effect is of changes in the exchange flow on tidal velocity characteristics in the channels (amplitude, peak asymmetry, duration asymmetry).
This manuscript has three specific aims. First, to consider the effect of tidal flats in a single channel with different along-channel distributions and different cross-sectional shapes of the tidal flats. Second, to investigate which overtides are generated in this configuration by the dissipation of momentum on the tidal flats and how this influences the ebb or flood dominance. Third, to study how the connection between two parallel channels during part of the tidal cycle by a tidal flat affects the velocity characteristics, such as the peak flood to peak ebb ratio, and the difference in duration between the transition from flood to ebb and vice versa. Changes in the peak velocity ratio will be linked to changes in net bedload sediment transport, while the differences in the duration asymmetry will be coupled to net suspended sediment transport. These goals will be achieved by considering two different geometries in a numerical model that solves the cross-sectionally averaged shallow water equations. The first contains a single channel with adjacent tidal flats. The sink of momentum on the tidal flats will be systematically investigated by considering different tidal flat areas, different tidal flat slopes and different along-channel distributions. Results of model runs with and without the momentum sink term will be compared and differences will be explained by investigating analytically which harmonic components are generated by this term. The second geometry contains two parallel channels, which are connected by a plateau which lies at an arbitrary fixed height between the low and high water line. In this way it only facilitates communication between the two channels during part of the tidal cycle. A comparison between model runs with and without tidal flat overtop-

ping will be presented with results for varying depths between the two channels, as well as different heights of the connecting tidal plateau between the two channels. Section 5.2 will describe the equations, how these are numerically solved, and give an overview of parameter settings. Results are presented in section 5.3, first for the single channel configuration and thereafter for the parallel channel configuration. In section 5.4 results will be discussed, including their implications for net transport of coarse and fine sediment. Finally, section 5.5 contains the conclusions.

5.2 Methods

5.2.1 Domain

In this study two distinct geometries are considered. One consists of a single channel with adjacent tidal flats, while another consists of two parallel channels connected by a tidal flat. The along-channel velocity on the tidal flats is assumed to be zero. The different configurations will be discussed consecutively.

Single channel geometry

This geometry comprises a basin of length l_b, which contains a channel of uniform depth h with adjacent tidal flats along the entire channel. The width of the basin is thus

$$b(x,t) = b_c(x) + b_f(x,t) \ , \tag{5.1}$$

where b is the local width of the basin, x is the along-channel coordinate increasing landward, t is time, and b_c and b_f are the widths of the channel and (submerged) tidal flats respectively. The width of the channel is assumed to decrease exponentially,

$$b_c(x) = b_{c,0} \exp\left(-\frac{x}{l_c}\right) \ , \tag{5.2}$$

with $b_{c,0}$ the channel width at the mouth, and l_c the e-folding length of the width convergence. The tidal flat width varies with the height of the free surface (see Fig. 5.1). Friedrichs & Aubrey (1996) and Friedrichs (2011) discussed equilibrium bottom profiles for intertidal areas, which range from concave to convex. Here, the family of concave tidal flat profiles is approximated by an additional constant width of intertidal area and a subsequent linear slope up to the high water line. The mathematical expression is

$$b_f(x,t) = b_{f,m}(x)\left(1 - \frac{1}{2q} + \frac{1}{2q}\frac{2\eta - (\eta_{\min} + \eta_{\max})}{\eta_{\max} - \eta_{\min}}\right) \ , \tag{5.3}$$

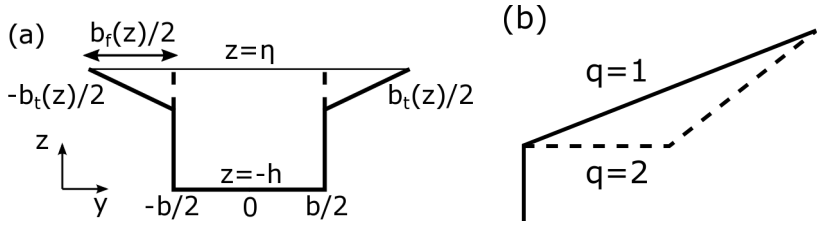

Figure 5.1: Panel (a): Cross-sectional profile applied in the single channel geometry. Panel (b): Lateral tidal flat profiles for different q as defined in Eq. (5.3).

with $b_{f,m}$ the maximum tidal flat width, $1/(2q)$ the linear slope of the tidal flat, η the local water level, and $\eta_{\min}$ ($\eta_{\max}$) the value of the local low (high) water line. For $q = 1$, this reduces back to the classical linear sloping tidal flats as was applied by Speer & Aubrey (1985); Friedrichs & Aubrey (1988) and Ridderinkhof *et al.* (2014) (see Fig. 5.1b).
Two different along-channel distributions of tidal flats are considered, i.e. one in which the tidal flats converge alongside the length of the channel, and one in which the width of the basin is considered constant. The first configuration is depicted in Fig. 5.2(a) and is formulated as

$$b_{f,m}(x) = b_{f,0} \exp\left(-\frac{x}{l_c}\right) , \tag{5.4}$$

while the constant basin configuration is shown in Fig. 5.2(b) and is formulated as

$$b_{f,m}(x) = b_{f,0} + b_{c,0}\left[1 - \exp\left(-\frac{x}{l_c}\right)\right] . \tag{5.5}$$

In both expressions, $b_{f,0}$ is the maximum width of the tidal flats at the mouth of the tidal channel. The amount of tidal flats is quantified by the ratio of the total maximum tidal flat area to the tidal channel area ($R_A = \mathrm{A}_{tf}/\mathrm{A}_c$). For the respective configurations, this reduces to

$$R_A = b_{f,m}/b_{c,0} \text{ , and} \tag{5.6}$$

$$R_A = \frac{l_b}{l_c}\frac{1 + b_{f,0}/b_{c,0}}{1 - \exp(-l_b/l_c)} - 1 . \tag{5.7}$$

Parallel channel geometry

In this geometry, two channels of length l_b, uniform depth h and constant width b are modelled parallel to each other. The two channels have different lengths, as well as different depths and widths. The channels exchange water over a tidal flat

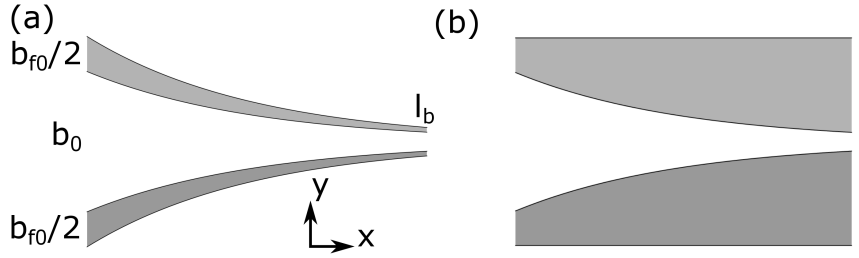

Figure 5.2: Plan view of the single channel configuration. Panel (a): Exponentially converging width of both the channel and tidal flats. Panel (b): Constant basin width with an exponentially converging channel.

with no lateral variability, which lies at a fixed height in between the low water line and the high water line at height h_f. The exchange occurs over a limited stretch of the channels, thus one of the channels is also partly characterized as a single channel. A top view of this configuration is provided in Fig. 5.3. The cross-sectional profile of the two channels is depicted in Fig. 5.4. In the remainder of the manuscript, variables for either of the channels are identified by a subscript l or r for the left or right channel, respectively.

5.2.2 Hydrodynamics

Hydrodynamics are modelled using the cross-sectionally averaged shallow water equations, as were introduced by Dronkers (1964) and derived in Appendix 5.A. These read for each channel

$$b_c \frac{\partial \eta}{\partial t} + \frac{\partial}{\partial x}\Big(b_c(h+\eta)u\Big) + V_\perp = 0 \ , \tag{5.8a}$$

$$\frac{\partial}{\partial t}\Big[b_c(h+\eta)u\Big] + \frac{\partial}{\partial x}\Big[b_c(h+\eta)u^2\Big] + u_\perp V_\perp \ = -g b_c(h+\eta)\frac{\partial \eta}{\partial x} - C_d b_c |u| u \ , \tag{5.8b}$$

in which u is the velocity averaged over the channel cross-section, t is time, g is the gravitational acceleration, and C_d is a drag coefficient. Furthermore, $V_\perp$ is a lateral volume transport per unit of length, which is positive for flow out of the channel. Finally, $u_\perp$ is the along-channel momentum per unit of mass that is transferred from the channel to the shoal (or vice versa) by $V_\perp$. Hence, $u_\perp V_\perp$ denotes the lateral momentum transport per unit of mass. Expressions for $V_\perp$ and $u_\perp V_\perp$ for the different geometries will be discussed more in the next subsections. The model is forced by an oscillating sea surface elevation at the open boundary

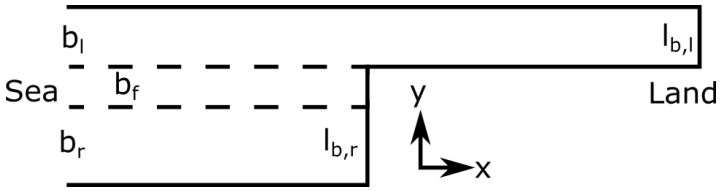

Figure 5.3: Plan view of the parallel channel geometry. The overtopping tidal flat is indicated by the dashed line.

$(x = 0)$ as

$$\eta(0,t) = A_{M2}\cos(\sigma t) \ ,$$

where A_{M2} is the forcing amplitude and $\sigma = 2\pi/P_t$ is the semi-diurnal angular tidal frequency (P_t is the period of the semi-diurnal M_2 tide, 12 hours and 25 minutes). At the closed end of each channel ($x = l_b$) the along-channel velocity is set to zero.

Lateral transport terms for the single channel

In the single channel geometry, the lateral transport terms describe the exchange flow with the tidal flats. Following the assumption of a uniformly rising sea surface elevation over the width of the basin at every cross section, the transport of mass and momentum from the tidal flats on either side of the channel are equal. The combined lateral volume transport per unit of length from both the tidal flats is approximated by

$$V_\perp = b_f \frac{\partial \eta}{\partial t} \ , \tag{5.9}$$

showing a proportionality with the velocity of the free surface and the instantaneous width of the tidal flat. For a rising sea level, water is exported to the tidal flats, while for the falling tide the opposite occurs. The along-channel momentum per unit of mass at the transition from the channel to the tidal flats is assumed to be equal to

$$u_\perp = u\mathcal{H}\left(\frac{\partial \eta}{\partial t}\right) \ . \tag{5.10}$$

Here, $\mathcal{H}(s)$ is the Heaviside function which is 1 (0) for positive (negative) arguments s. Thus, the along-channel momentum per unit of mass at the transition from the channel to the flat matches the along-channel momentum per unit of mass in the channel on the rising tide, while it is zero for the falling tide. This

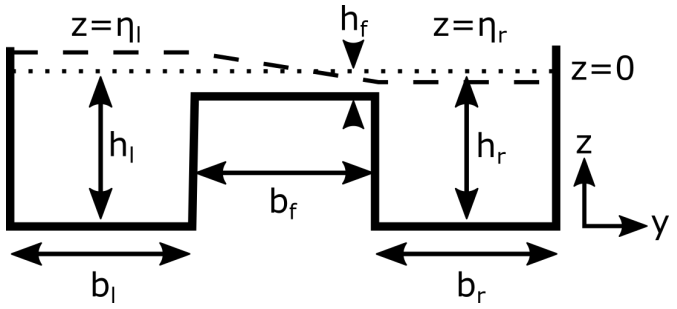

Figure 5.4: Shape of the cross-section for the parallel channel geometry.

expression (parametrically) accounts for the dissipation of momentum from the channel on the tidal flats, which is the momentum sink under investigation. Using Eqs. (5.9) and (5.10), Eq. (5.8) transforms to

$$(b_c + b_f)\frac{\partial \eta}{\partial t} + \frac{\partial}{\partial x}\Big(b(h+\eta)u\Big) = 0 \ , \tag{5.11a}$$

$$\frac{\partial u}{\partial t} + u\frac{\partial u}{\partial x} - \frac{u b_f}{b_c(h+\eta)}\frac{\partial \eta}{\partial t}\mathcal{H}\left(-\frac{\partial \eta}{\partial t}\right) = -g\frac{\partial \eta}{\partial x} - \frac{C_d|u|u}{h+\eta} \ . \tag{5.11b}$$

Here, Eq. (5.11a) has been used to rewrite Eq. (5.8b) to Eq. (5.11b) and the property of the Heaviside function has been applied that $\mathcal{H}(s) - 1 = -\mathcal{H}(-s)$.

Lateral transport terms for the parallel channels

In the parallel channel configuration, Eq. (5.8) is solved for both the left and right channel. Hence, the lateral transport terms also have a value in both channels, which will be denoted with a subscript l and r. The lateral volume transport per unit of length in the parallel channel geometry represents the exchange of water between the two channels. Two situations are distinguished. Firstly, if neither of the channels has a sea surface elevation above the tidal flat plateau, there is no exchange of water, thus

$$\begin{aligned} V_{\perp,l} &= 0 \ , && \text{if } \eta_l \leq h_f \ , \\ V_{\perp,r} &= 0 \ , && \text{if } \eta_r \leq h_f \ , \end{aligned} \tag{5.12}$$

where h_f is the height of the tidal flat plateau. If either of the channels has a sea surface elevation above the tidal flat plateau, $V_{\perp,l}$ and $V_{\perp,r}$ are determined

through a lateral momentum equation, such that if $\eta_l > h_f$, or $\eta_r > h_f$, then

$$\begin{aligned} \frac{\partial v}{\partial t} &= -g\frac{\tilde{\eta}_r\mathcal{H}(\tilde{\eta}_r) - \tilde{\eta}_l\mathcal{H}(\tilde{\eta}_l)}{b_f} - \frac{C_d|v|v}{\frac{1}{2}(\tilde{\eta}_l\mathcal{H}(\tilde{\eta}_l) + \tilde{\eta}_r\mathcal{H}(\tilde{\eta}_r))} \ , \\ V_{\perp,l} &= \left[\frac{\tilde{\eta}_l\mathcal{H}(\tilde{\eta}_l) + \tilde{\eta}_r\mathcal{H}(\tilde{\eta}_r)}{2}\right] v \ , \\ V_{\perp,r} &= -\left[\frac{\tilde{\eta}_l\mathcal{H}(\tilde{\eta}_l) + \tilde{\eta}_r\mathcal{H}(\tilde{\eta}_r)}{2}\right] v \ . \end{aligned} \tag{5.13}$$

Here, $\tilde{\eta}_l = \eta_l - h_f$ and $\tilde{\eta}_r = \eta_r - h_f$, i.e. the water level above the tidal flat plateau in the channels. Moreover, v is the depth averaged velocity in the lateral direction over the tidal flat. The momentum equation is adopted from Hamilton (1990), who applied the same equation when both channels had a surface elevation above the tidal flat plateau. However, he used a broad-crested weir formula, when the elevation in only one channel was above the tidal flat plateau. This approach causes discontinuities in the lateral velocity, v, both when sea surface rises above the tidal flat plateau as well as when it falls below the tidal flat plateau. In the current approach, the momentum equation contains Heaviside functions to prevent these discontinuities during the rising tide. Finally, the along-channel momentum per unit of mass that is transferred from the channel to the tidal flat (or vice versa) is given by

$$\begin{aligned} u_{\perp,l} &= u_l\mathcal{H}(v) \ , \\ u_{\perp,r} &= u_r\mathcal{H}(-v) \ , \end{aligned} \tag{5.14}$$

Thus, no along-channel momentum is transferred from one channel to the other. Rather, the along-channel momentum is dissipated on the tidal flats. Note that the current approach implies there is no storage of water on the tidal flat. The transfer of water between the channels is instantaneous, which is an approximation of nature where the tidal flat has to be flooded first.

5.2.3 Numerical scheme

Eqs. (5.8), and the appropriate equations for the lateral transports, are solved numerically. The model uses a regular grid in space, with u and η both computed in all grid-points. The internal grid points use central differencing for spatial derivatives, which reads

$$\frac{\partial f}{\partial x} \approx \frac{f(x+\Delta x) - f(x-\Delta x)}{2\Delta x} \ ,$$

for an arbitrary function $f(x)$. The accuracy of this approximation is quadratic in the grid-distance (Δx). At the boundaries second order accurate up- and down-

wind scheme are applied, which read

$$\frac{\partial f}{\partial x} \approx \frac{-3/2f(x) + f(x+\Delta x) - 1/2f(x+2\Delta x)}{2\Delta x} \quad \text{, at } x = 0 \text{ ,}$$
$$\frac{\partial f}{\partial x} \approx \frac{3/2f(x) - f(x-\Delta x) + 1/2f(x-2\Delta x)}{2\Delta x} \quad \text{, at } x = l_b \text{ .}$$

Time integration is carried out using a Runge-Kutta scheme of fourth order, which for an arbitrary time derivative

$$\frac{\partial f}{\partial t} = F(f(t), t) \text{ ,}$$

computes the temporal change in a variable as

$$\begin{aligned} f(t+\Delta t) &= f(t) + \frac{\Delta t}{6}(k_1 + 2k_2 + 2k_3 + k_4) \\ k_1 &= F(f(t), t) \text{ ,} \\ k_2 &= F(f(t) + \frac{\Delta t}{2}k_1, t + \frac{\Delta t}{2}) \text{ ,} \\ k_3 &= F(f(t) + \frac{\Delta t}{2}k_2, t + \frac{\Delta t}{2}) \text{ ,} \\ k_4 &= F(f(t) + \Delta t\ k_3, t + \Delta t) \text{ .} \end{aligned}$$

Finally, since the solutions to Eq. (5.8) and the width of the basin depend on each other through the minimum and maximum water levels, these values are updated several times during the model run.

5.2.4 Analysis

The output from the model is analyzed using a harmonic analysis. Time series of any state variable are decomposed in harmonic components as

$$\xi = \sum_{k=0}^{\infty} C_{\xi,k} \cos(k\sigma t - \phi_{\xi,k}) \text{ ,} \tag{5.15}$$

which contains the dominant semi-diurnal lunar tidal component and its overtides. The latter have an integer times the frequency of the principal tide. Here, $\xi = \{u, \eta, V_\perp\}$ can be any of the state variables, $C_{\xi,k}$ is the amplitude of harmonic component k of this variable and $\chi_{\xi,k}$ is the corresponding phase.
The change in different harmonic components due to the incorporation of momentum sink and overtopping will be investigated. Moreover, for momentum sink on the tidal flats in the single channel an analytical analysis will be performed to determine which harmonic components are most strongly affected by this process. In this study, only harmonic components from $k = 0$ (residual) up to $k = 3$ (M_6)

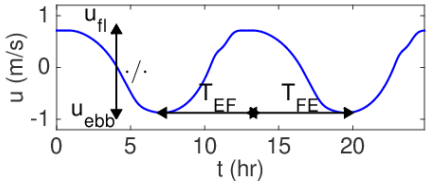

Figure 5.5: Time series of velocity as computed by the model for the single channel configuration without tidal flats. The peak velocity ratio (u_{fl}/u_{ebb}) and the difference in duration between peak velocities (T_{FE} - T_{EF}) are indicated for clarity.

are considered, as these are the most dominant components in most estuaries, and thus also contribute strongest to the tidally averaged (net) transport of bedload sediment (van de Kreeke & Robaczewska, 1993) and suspended sediment (Groen, 1967; Dronkers, 1986).
Implications on changes in net sediment transport will be given based on the ratio of peak flood (u_{fl}) to peak ebb velocity (u_{ebb}), and the difference in the duration of the transition from peak flood to peak ebb velocity (T_{FE}) and the duration of the transition from peak ebb to peak flood (T_{EF}), similar to Alebregtse & de Swart (2014, see Fig. 5.5). The velocity ratio (u_{fl}/u_{ebb}) is an important indicator for the direction of net bedload transport (coarse sediment), which reacts nearly instantaneously to the flow. If the velocity ratio is larger than 1 the net bedload transport is in the flood direction, while for ratios smaller than 1 transport is in the ebb direction (Friedrichs & Aubrey, 1988). The difference in the duration between peak velocities ($T_{FE} - T_{EF}$) is more important for fine sediment, as pointed out by Groen (1967), Dronkers (1986), and de Swart & Zimmerman (2009, appendix B). While sediment is eroded during the peak velocity events, settling takes place during slack conditions. If the transition from peak flood to peak ebb velocities lasts longer than the transition from peak ebb to peak flood velocities, more sediment can settle after the erosion event of the peak flood velocities. This leads to less sediment in the water column for transport during ebb. Hence, the net fine sediment transport of this mechanism is in the flood direction. Ebb directed net transport of this mechanism is stronger when the time between peak ebb and peak flood is longer than the time between peak flood and peak ebb.

5.2.5 Model set-up

Single channel

The single channel domain was chosen to resemble shallow tidal basins such as the Ameland Inlet in the Dutch Wadden Sea. This basin comprises an exponentially

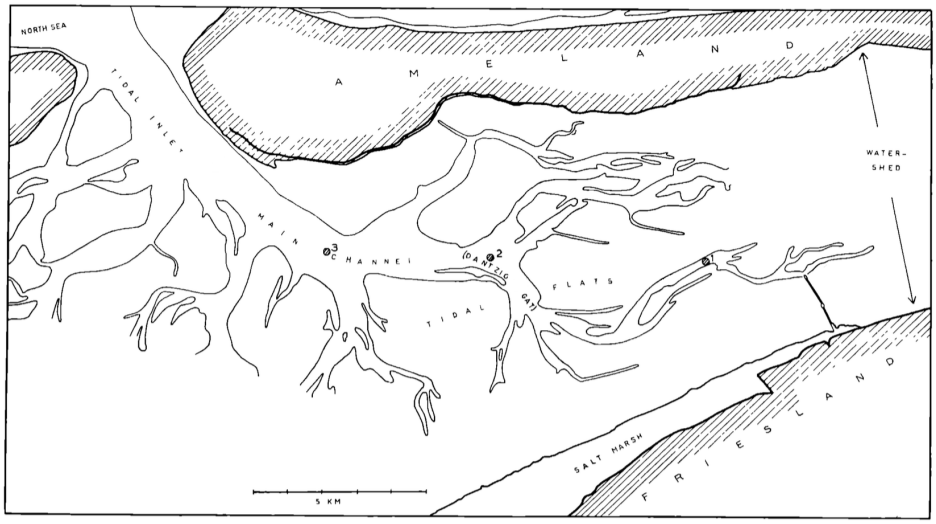

Figure 5.6: Map of the Ameland basin, located in the Dutch part of the Wadden Sea, which is a marginal sea of the North Sea. The numbers indicate measurement locations of the velocity. Figure after Postma (1961).

converging channel and extensive tidal flat areas. Depth, channel length and width convergence length scale for the Ameland Inlet were taken from Dronkers (2005). Tidal flat area and tidal flat lateral profile were varied, as well as the along-channel distribution of the tidal flats.

Parallel channels

The model configuration for the parallel channels is chosen to resemble the upstream part of the Ems estuary (see Fig. 5.7). In its seaward part, the model domain consists of two parallel channels of 13 km long, after which it continues as a single channel up to the landward boundary. The last stretch is an additional 47 km long and has a default depth of 8 m. The left (long) channel is represented with a constant width of 1 km, while the right channel has a depth of 4 m and a

Table 5.1: Model configuration as used in the single channel domain. This set-up resembles the Ameland inlet as given by Dronkers (2005).

Variable	l_b (km)	l_c (km)	h (m)	b_0 (m)	R_A	A_{M2} (m)	q
Value	25	15	3.75	4000	0–6	1.25	1–2

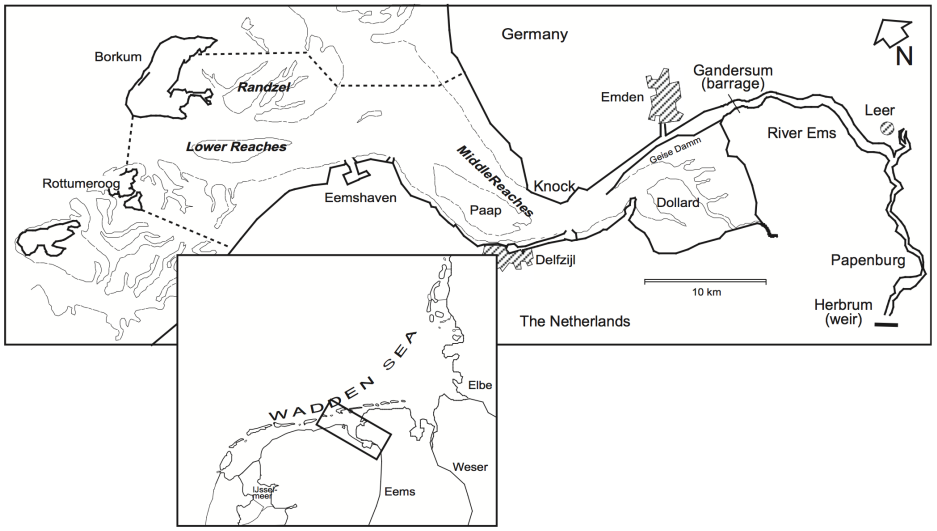

Figure 5.7: Map of the Ems estuary, located in the Dutch part of the Wadden Sea, which is a marginal sea of the North Sea. Figure after de Jonge (2000).

constant width of 7 km. The two channels are connected by a 4 km wide tidal flat. This mimics the Ems river from Knock to Herbrum with the left channel, and the Dollart bassin with the right channel. The height of the tidal flat plateau, as well as the depth of the left channel (over the entire length of 60 km) is varied.

5.3 Results

5.3.1 Single channel

For the single channel configuration, the effect of three parameters on the cross-sectionally averaged, along-channel velocity will be investigated. Firstly, the amount

Table 5.2: Model configuration as used in the parallel channels domain. This set-up resembles the upstream part of the Ems estuary.

Variable	l_b (km)	h (m)	b_0 (m)	$b_{f,0}$ (m)	A_{M2} (m)	h_f (m)
Value (left)	13	4–12	1000	4000	1.3	-1.5–1.5
Value (left, ext.)	47	4–12	1000	0	–	–
Value (right)	13	4	7000	4000	1.3	-1.5–1.5

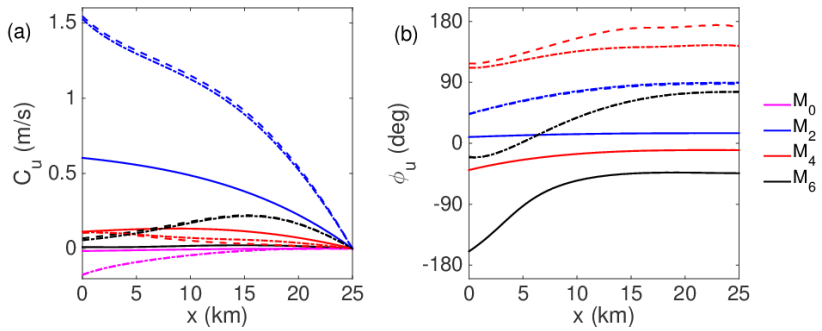

Figure 5.8: Panel (a): Amplitude of the harmonic components of tidal velocity versus along-channel distance for a basin configuration as in Fig. 5.2(a). Solid lines show results for $R_A = 0$ (Eq. 5.6), while the dashed (dashed-dotted) lines show results for $R_A = 6$ and $q = 1$ without (with) momentum sink. Panel (b): as panel (a), but for the phase of the harmonic velocity components.

of tidal flats adjacent to the main channel. Secondly, the lateral profile of the tidal flats. And finally, the along-channel distribution of the tidal flats. All scenarios will be analyzed both with and without accounting for momentum sink on the tidal flats.

Exponentially decreasing flat width

In this section, results will be presented for model runs using the model configuration such as depicted in Fig. 5.2(a). Firstly, in Fig. 5.8 the velocity amplitude (panel a) and phase (panel b) of the different harmonic components are plotted as a function of the along-channel coordinate. Solid lines depict model results for a channel without tidal flats (i.e. $R_A = 0$), and dashed (dashed-dotted) lines represent model results for $R_A = 6$ with linear sloping tidal flats, i.e. $q = 1$, without (with) momentum sink accounted for. The presence of tidal flats increases M_2 and M_6 tidal velocities indicated by the blue and black lines, respectively. Quarter diurnal velocities (red lines) decrease due to the tidal flats. Momentum sink slightly lowers M_2 and M_6 velocity amplitudes throughout the basin, while M_4 velocity amplitude is slightly enhanced.
Fig. 5.9 shows the dependence of the differences in the harmonic components of the velocity (in cm/s) at the seaward boundary ($x = 0$) between model results including and excluding the momentum sink on the tidal flats on the ratio of tidal flat area to channel area and tidal flat slope. Positive differences indicate an increase in velocity amplitude due to momentum sink. Investigating the seaward boundary

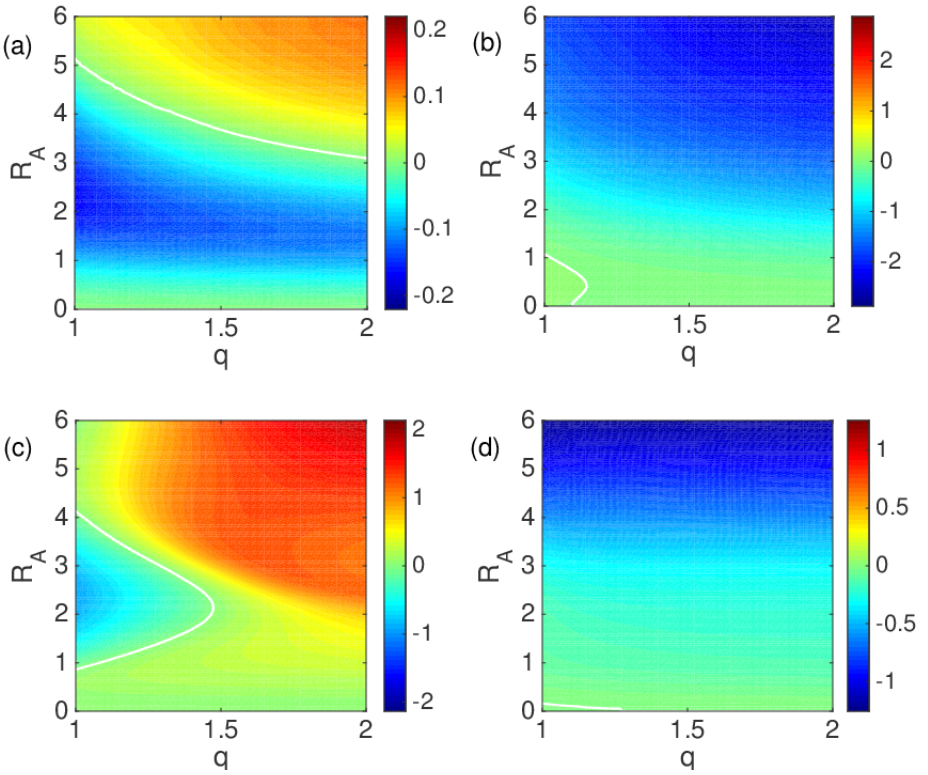

Figure 5.9: Dependence of the difference in tidal velocity amplitude for the different harmonic components at the seaward boundary (in cm/s) with and without accounting for momentum sink on the tidal flats on the ratio of maximum tidal flat area to tidal channel area and tidal flat slope. White lines show the zero-contour. The components are M_0, M_2, M_4 and M_6 in panel (a) through (d), respectively.

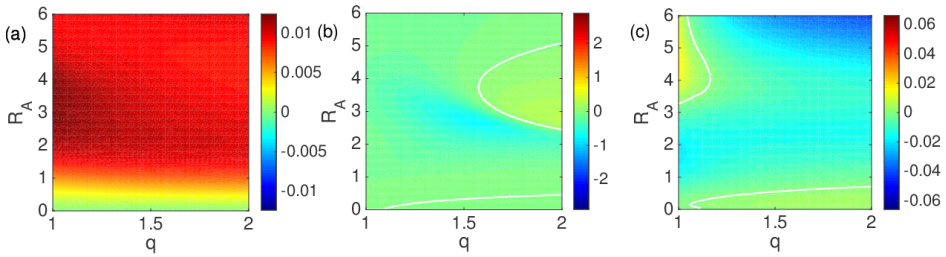

Figure 5.10: As Fig. 5.9, but for the difference in tidal velocity phase. Note that the residual component is omitted, since this component has no phase. Hence, panel (a), (b), and (c) are the M_2, M_4 and M_6 component, respectively.

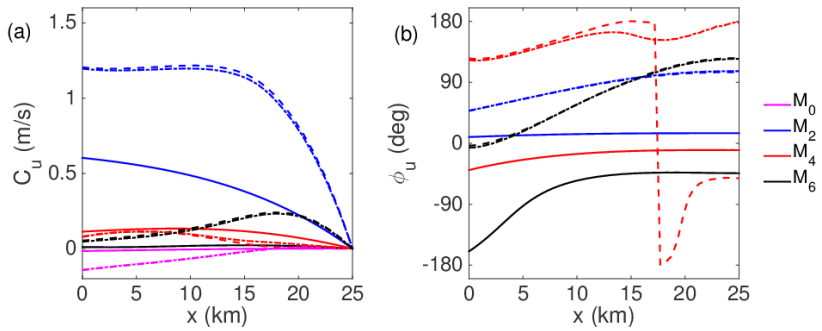

Figure 5.11: As Fig. 5.8, but for a configuration as in Fig. 5.2(b).

allows to translate the implications for changes in net sediment transport (discussed in section 5.4) to changes in sediment import or export from the system, which is important for longterm morphologic stability. The panels (a), (b), (c) and (d) show results for the M_0, M_2, M_4 and M_6 component, respectively. The M_2 and M_6 velocity amplitudes decrease slightly due to the momentum sink. The M_0 and M_4 velocity component show more variability, with a decrease in quarter diurnal velocity amplitude for tidal flats which are close to linear (i.e. $q \approx 1$), while M_4 velocity amplitudes increase for increasing q. Similarly, residual velocities decrease for small tidal flats as a result of momentum sink, while for tidal flats with a large surface area momentum sink increases residual velocities.
Fig. 5.10 shows how the phases of the different harmonic velocity components (M_2, M_4, and M_6) change due to momentum sink for varying tidal flat area and tidal flat slope. Overall, changes are negligibly small.

Constant basin width

In this section, results will be presented for model runs using the model configuration such as depicted in Fig. 5.2(b). Again, first a comparison is made on the along-channel distribution of the velocity amplitude and phase of the M_0, M_2, M_4, and M_6 harmonic components. Results are shown in Fig. 5.11, which is similar to Fig. 5.8, but for the new configuration. The semi-diurnal tidal velocity at the open boundary increases by a smaller amount for the new configuration, compared to the configuration with the exponentially decreasing tidal flat width. However, further landward the velocity amplitude is higher in the new configuration than in the previous one. Additionally, the overtide velocities (M_4 and M_6) are higher in the new configuration compared to the previous configuration.
Fig. 5.12 is again similar to Fig. 5.9, and shows the difference in the amplitudes

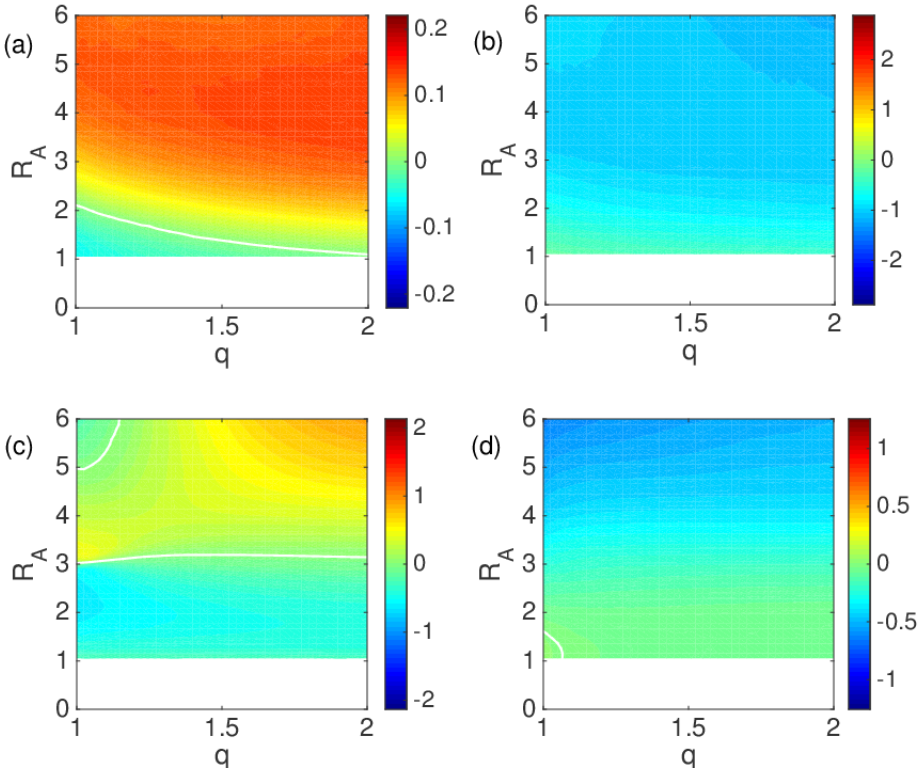

Figure 5.12: As Fig. 5.9, but for a configuration as in Fig. 5.2(b).

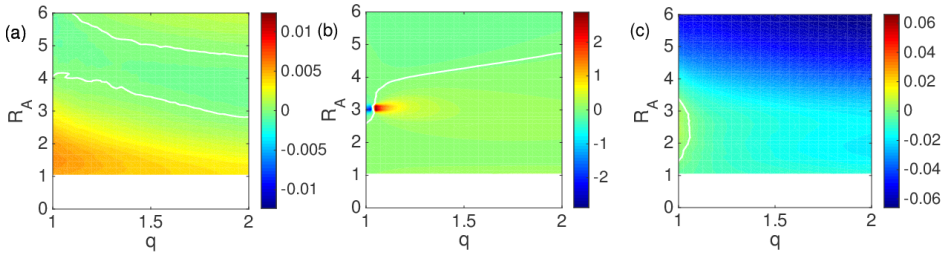

Figure 5.13: As Fig. 5.10, but for a configuration as in Fig. 5.2(b).

of the various harmonic components of the velocity (in cm/s) at the seaward boundary between model runs with and without momentum sink. The velocity differences are displayed in dependence to the tidal flat area and tidal flat slope on the vertical and horizontal axis, respectively. Relative tidal flat area starts at a value near unity, which is the result of the constant total width assumption. Since the channel width has an exponential convergence, tidal flats are present adjacent to the channel towards the landward boundary. Semi-diurnal and residual velocity amplitudes show an overall decrease due to momentum sink, similar to the previous configuration. However, the decrease is less strong. Momentum sink causes a decrease in semi-diurnal velocity amplitudes up to about 1 cm/s, which is only about 1% of the value of the amplitude. For residual velocities, changes are also smaller, but show increases in velocity for a broader range of tidal flat areas and slopes. The overtides behave quite differently. Particularly, changes in M_4 velocity amplitude are more related to the tidal flat area than the tidal flat slope. For small tidal flat areas, the M_4 velocity amplitude decreases due to momentum sink. This decrease is smaller for steeper slopes. For large tidal flat area, the M_4 velocity amplitude increases due to momentum sink (with the exception of linear sloping tidal flats with a large extent). This increase becomes larger for steeper slopes. The effect of momentum sink on the M_6 velocity amplitude in the configuration with a constant total width decreases with tidal flat slope, while it increases in the configuration of a converging total width.

5.3.2 Parallel channels

For the parallel channel configuration, the sensitivity of the velocity characteristics to changes in tidal flat height and channel depth will be investigated. The set-up consists of two channels, one of 60 km long and one of 13 km long, which have a possibility to exchange water over a tidal flat up to 13 km landward from the open boundary. In Fig. 5.14 (a) and (b), the velocity amplitude and phase of the dominant three harmonic components are shown for a configuration with no overtopping, and a channel depth of 8 m in the left channel. The M_2, M_4, and M_6 components are shown in blue, red, and black, respectively. Additionally, the solid lines show results for the left channel, while the dashed lines show results for the short right channel. All harmonic components decrease towards the end of the basins, except for the M_6 component in the left channel, which first experiences an increase. In Fig. 5.14 (c) and (d) the sea surface height amplitude and phase are shown of the various harmonic components. This illustrates for which range of tidal flat heights communication between the two channels is possible. In the right (short) channel, all amplitudes are seen to increase landward. For the overtides similar results are found in the left (long) channel, with amplitudes peaking at the landward end. However, the semi-diurnal component attains a minimum around

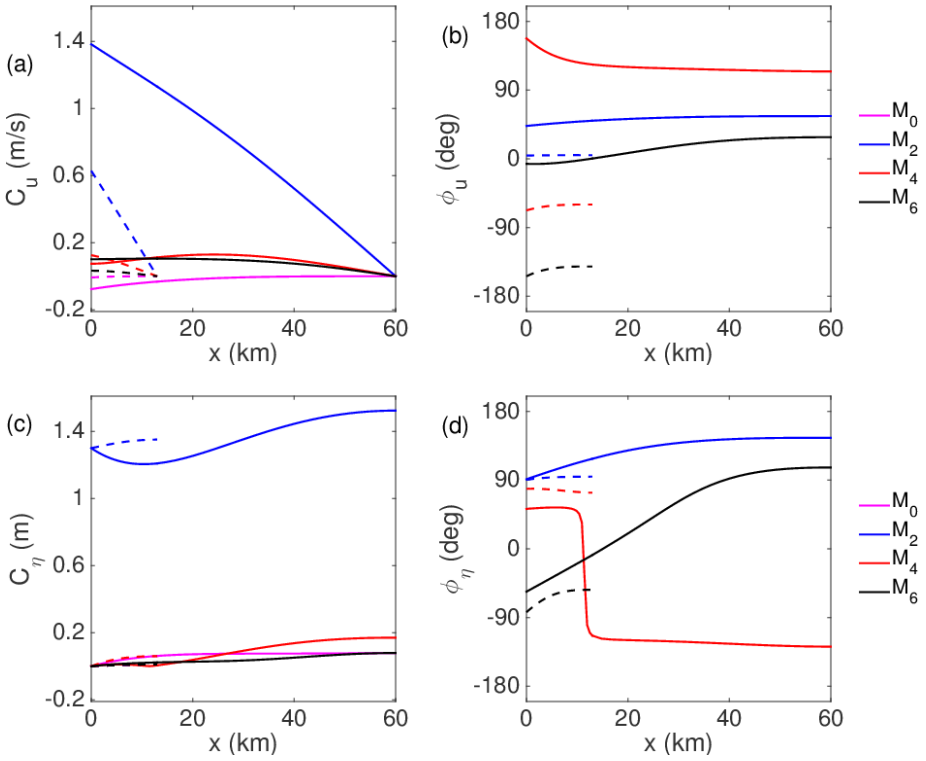

Figure 5.14: Panel (a): Amplitude of the harmonic components of the velocity for the default parallel channel configuration when no overtopping occurs as a function of along-channel coordinate. Panel (b): As panel (a), but for the velocity phase. Panel (c) and (d): As panels (a) and (b) but for sea surface height amplitude and phase, respectively. Magenta, blue, red and black lines denote the M_0, M_2, M_4, and M_6 component, respectively. Solid lines show results of the left channel and dashed lines of the short right channel.

10 km landward from the open boundary.

Figs. 5.15 and 5.16 show the changes in amplitude of the harmonic components of the velocity (in m/s) for the left and right channel, respectively, in dependence of depth in the left channel, and tidal flat height. Depth in the left channel was varied between 4 and 12 m, to cover a range of depths as observed due to past and possible future dredging in the Ems (de Jonge *et al.*, 2014). Tidal flat height ranges from -1.5 m to 1.5 m, which corresponds to continuous and no communication between the channels and everything in between. Panels (a), (b), (c), and (d) show the results for the M_0, M_2, M_4, and M_6 velocity amplitude, respectively.

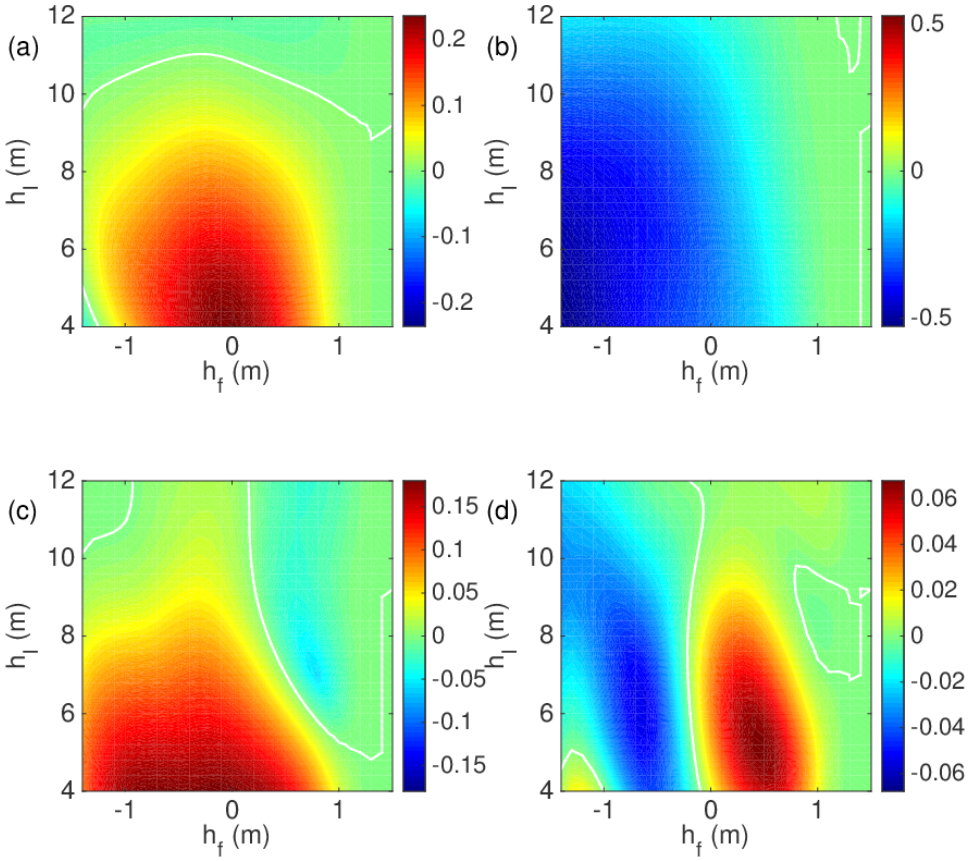

Figure 5.15: Difference of the velocity amplitude of the harmonic components at the seaward boundary with and without tidal flat overtopping (in m/s) in the left channel as a function of depth of the left channel (h_l) and tidal flat height (h_f). White lines show the zero-contour. Panel (a) through (d) show M_0, M_2, M_4, and M_6, respectively.

Due to the larger width of the right channel, velocity changes are less pronounced there. Interestingly, configurations are found where velocity amplitude of a certain harmonic component increases or decreases for both channels. For example, an increase in the M_6 velocity amplitude is observed for tidal flat heights around 0.5 m for all channel depths.

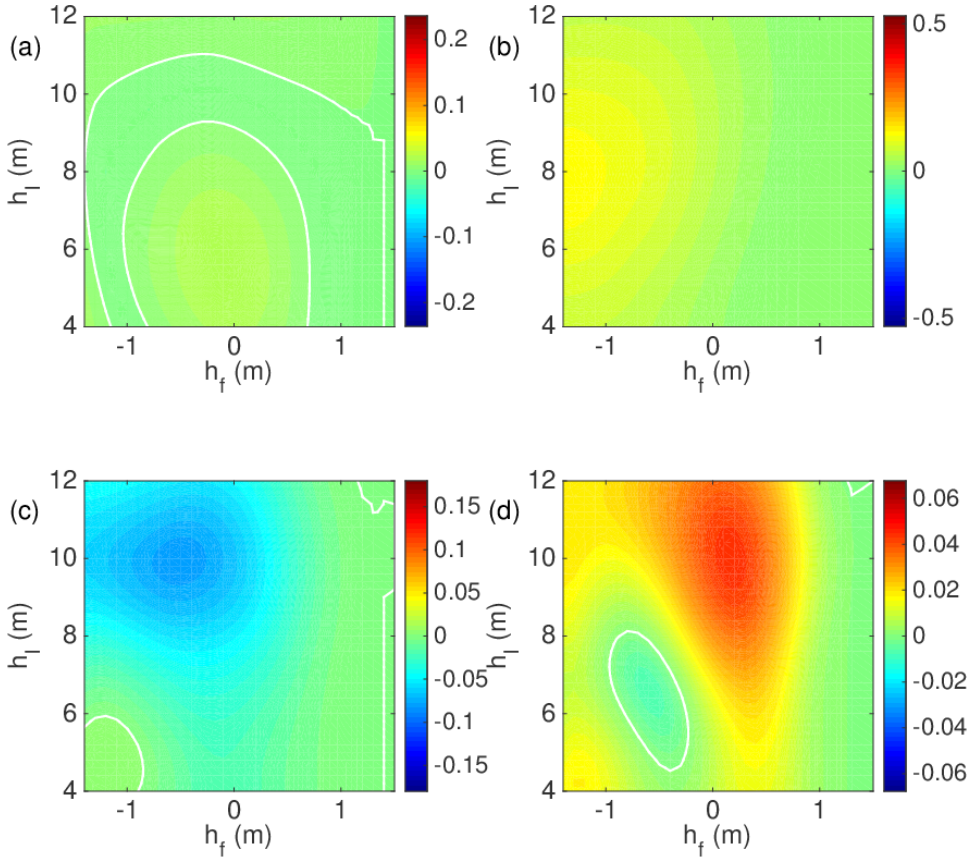

Figure 5.16: As Fig 5.15, but for the right channel.

5.4 Discussion

In this section, firstly the dissipation of momentum on the tidal flats will be investigated analytically, to identify which overtides are produced by what mechanisms. Secondly, model output for the single channel configuration will be qualitatively compared to measurements. Thirdly, the effect of the overtides on the asymmetrical characteristics of the velocity curve, viz. the peak flood to peak ebb velocity ratio and the difference in duration between the transition from peak flood to peak ebb and vice versa, will be discussed. The asymmetrical characteristics of the ve-

locity curve are also investigated for the parallel channel configuration. Based on the asymmetry characteristics of the velocity profile, implications for net sediment transport are discussed.

5.4.1 Single channel: Harmonic decomposition momentum sink

To explain the results in Fig. 5.9, the momentum sink will be analyzed analytically with a harmonic decomposition. The momentum sink term in the single channel configuration, presented in Eq (5.11), reads

$$\mathrm{MS} = \frac{ub_f}{b_c(h+\eta)}\frac{\partial \eta}{\partial t}\mathcal{H}\left(-\frac{\partial \eta}{\partial t}\right) \ . \tag{5.16}$$

The aim is now to determine which harmonic components are generated by the momentum sink. For this purpose, a semi-diurnal tidal signal is substituted into the equation, reading

$$\xi = \mathcal{R}\left(C_\xi e^{-i(\sigma t-\phi_\xi)}\right) = \frac{1}{2}\left(C_\xi e^{-i(\sigma t-\phi_\xi)} + C_\xi e^{i(\sigma t-\phi_\xi)}\right) \ . \tag{5.17}$$

with all variables the same as in Eq. (5.15). This is an approach, which is commonly used in analytical models, where the semi-diurnal tide is assumed to be the dominant tidal constituent as is also the case here. The semi-diurnal tide subsequently forces all non-linear processes, resulting in overtides (see for example Friedrichs & Aubrey, 1988; Ridderinkhof *et al.*, 2014).
First, the Heaviside function is rewritten using a complex Fourier series as

$$\mathcal{H}\Big(-\frac{\partial \eta}{\partial t}\Big) = \sum_{k=-\infty}^{\infty} A_k e^{-ik\sigma t} \ ,$$
$$A_k = \frac{\sigma}{2\pi}e^{-ik\sigma t}\int_{-\pi/\sigma}^{\pi/\sigma}\mathcal{H}\Big(-\frac{\partial \eta}{\partial t}\Big)e^{ik\sigma t}dt \ .$$

Using Eqn. (5.17), it follows

$$-\frac{\partial \eta}{\partial t} = -\frac{1}{2}\frac{\partial}{\partial t}\Big(C_\eta e^{-i(\sigma t-\phi_\eta)} + C_\eta e^{i(\sigma t-\phi_\eta)}\Big) \ ,$$
$$= \sigma C_\eta \sin(\sigma t-\phi_\eta) \ .$$

Then, using $A_{-k} = A_k^*$ with $*$ the complex conjugate, the harmonic series for the Heaviside function becomes

$$\mathcal{H}\left(-\frac{\partial \eta}{\partial t}\right) = \frac{1}{2} + \sum_{k=1}^{\infty}\left[\frac{i}{2\pi k}\Big(1-e^{ik\pi}\Big)e^{-ik(\sigma t-\phi_\eta)} - \frac{i}{2\pi k}\Big(1-e^{-ik\pi}\Big)e^{ik(\sigma t-\phi_\eta)}\right] . \tag{5.18}$$

This expression indicates that the Heaviside function induces residual tides and overtides at only odd frequencies of the principal tide. These become increasingly smaller for higher frequencies, due to the $i/(2\pi k)$ dependence. In Eqn. (5.16), the above expression (Eqn. 5.18) is multiplied by

$$\frac{ub_f}{b_c(h+\eta)}\frac{\partial \eta}{\partial t} \ . \tag{5.19}$$

For simplicity, only the first configuration of the single channel (Fig. 5.2a) is considered here, hence Eq. (5.1) is substituted for the width of the channel, and Eqs. (5.3) and (5.4) for the width of the tidal flats. Moreover, depth variations within the tidal cycle are neglected with respect to the undisturbed depth (i.e. $(h+\eta) \approx h$) and Eqn. (5.17) is used to substitute u and η. Then, Eq. (5.19) evaluates as

$$\frac{b_{f,0}}{b_0 h} C_u C_\eta \left(\underbrace{1 - \frac{1}{2q}}_{\text{A}} + \underbrace{\frac{1}{2q}\mathcal{R}\Big(e^{-i(\sigma t - \phi_\eta)}\Big)}_{\text{B}} \right) \mathcal{R}\Big(e^{-i(\sigma t - \phi_u)}\Big)\mathcal{R}\Big(- i\sigma e^{-i(\sigma t - \phi_\eta)}\Big) \ , \tag{5.20}$$

which contains double and triple products of the principal tide in terms A and B, respectively. The double product of the principal tide produces residual and M_4 tides, while the triple product results in M_2 and M_6 tides. For steep tidal flat slopes, the production of overtides by the triple products decreases due to q being in the denominator. Furthermore, the general effect of the momentum sink increases for increasing tidal flat area due to the $b_{f,0}/b_0$ (the ratio of the maximum tidal flat width to the channel width at the seaward boundary) term.
Multiplying Eq. (5.18) and Eq. (5.20) yields the production of residual, M_2, M_4 and all subsequent odd overtides (M_6, M_{10}, etc.) due to the the product of Eq. (5.18) and term A in Eq. (5.20). The product of Eq. (5.18) and term B in Eq. (5.20) only yields even overtides. This explains the results shown in Fig. 5.9, where the M_2 and M_6 harmonic component become more strongly influenced by the momentum sink for increasing tidal flat width and increasing tidal flat slope. Because all contributions of momentum sink produce M_4 tides, this harmonic component is more strongly influenced. Nevertheless, momentum sink increases M_4 velocity amplitude for mild slopes and decreases M_4 velocity amplitude for steeper slopes, showing the different characters of forcing.

5.4.2 Single channel: Comparison to observations

In Fig. 5.17, model results for the single channel configuration are compared with velocity measurements taken in the Ameland basin from Postma (1961). Results

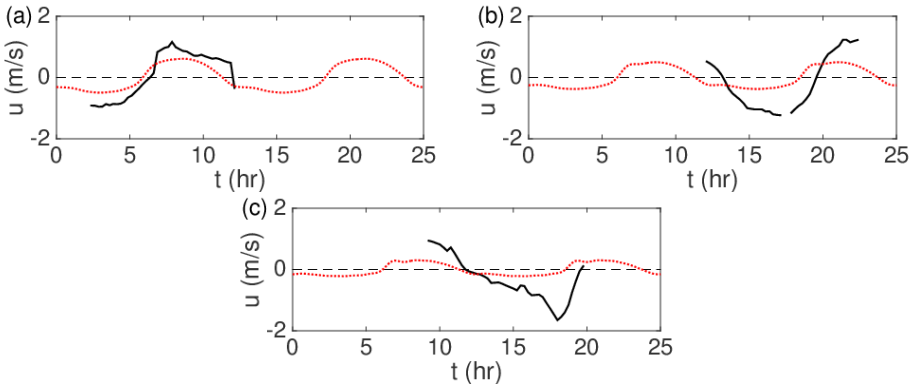

Figure 5.17: Comparison of model results from the single channel configuration with data from Postma (1961). A constant basin width configuration with R_A=2.7 and $q = 1$ was chosen. The data were collected at 6, 12, and 18 km into the basin for panel (a), (b), and (c), respectively.

for a model that is configured with a constant basin width and $R_A = 2.7$, are shown by the red line. Panels (a), (b), and (c) show measurements taken at 6, 12, and 18 km into the basin. The duration of the flood tide is captured quite well by the model. The qualitative behaviour of the velocity at 12 km is also captured fairly well, with first flattening of the ebb velocity and a subsequent further decrease. The velocity changes to flood to early further down the basin, and amplitude values seem to drop off to quickly towards the end of the basin. This is probably caused by the constant depth assumed throughout the channel, instead of a sloping bottom such as observed in nature.

5.4.3 Single channel: Implications for net sediment transport

Implications for net sediment transport are based on the non-linear characteristics of the velocity curve as described in the introduction in section 5.2.4. These were the peak velocity ratio (flood to ebb), and the difference in the duration between peak velocities (the duration between peak flood and peak ebb minus the duration between peak ebb and peak flood). Changes in these parameters are investigated near the seaward boundary. Implications on the net sediment transport are thus equivalent to changes in morphodynamic stability, since the net sediment transport at the seaward boundary gives an indication for the long term importing or exporting character of the basin.
Fig. 5.18(a) and (c) shows the dependence of the peak velocity ratio on the tidal

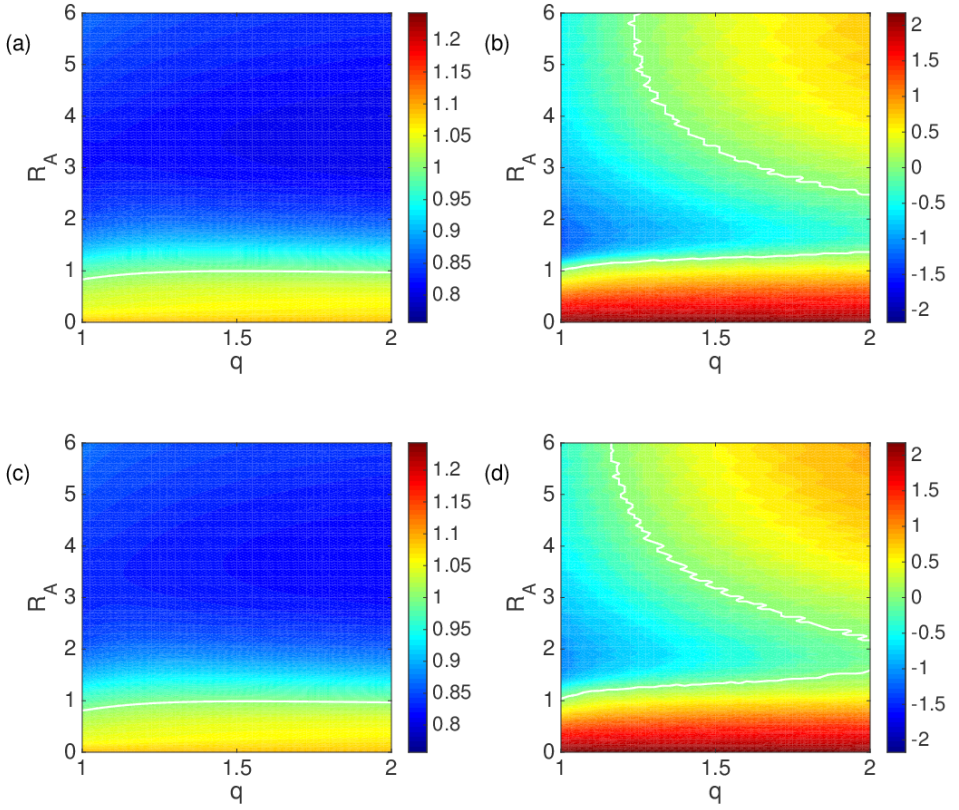

Figure 5.18: Panel (a): Dependence of the peak velocity ratio (flood to ebb) to the tidal flat area ratio (R_A) and the tidal flat slope (q) without accounting for momentum sink in the configuration with an exponentially converging width (Fig. 5.2a). Panel (b): As panel (a), but for the difference between the transition duration from peak flood to peak ebb and vice versa. Panel (c) and (d): As panels (a) and (b), but including the effect of momentum sink

flat area ratio R_A and the tidal flat slope q for the configuration with an exponentially converging total width. In panel (a), model results without momentum sink are shown, while in panel (c) results include momentum sink. There are only quantitative differences between the two, with the minimum in velocity ratio becoming less strong. This shows that for coarse sediment, which is mainly transported as bedload, momentum sink does not qualitatively affect the net transport. Similarly,

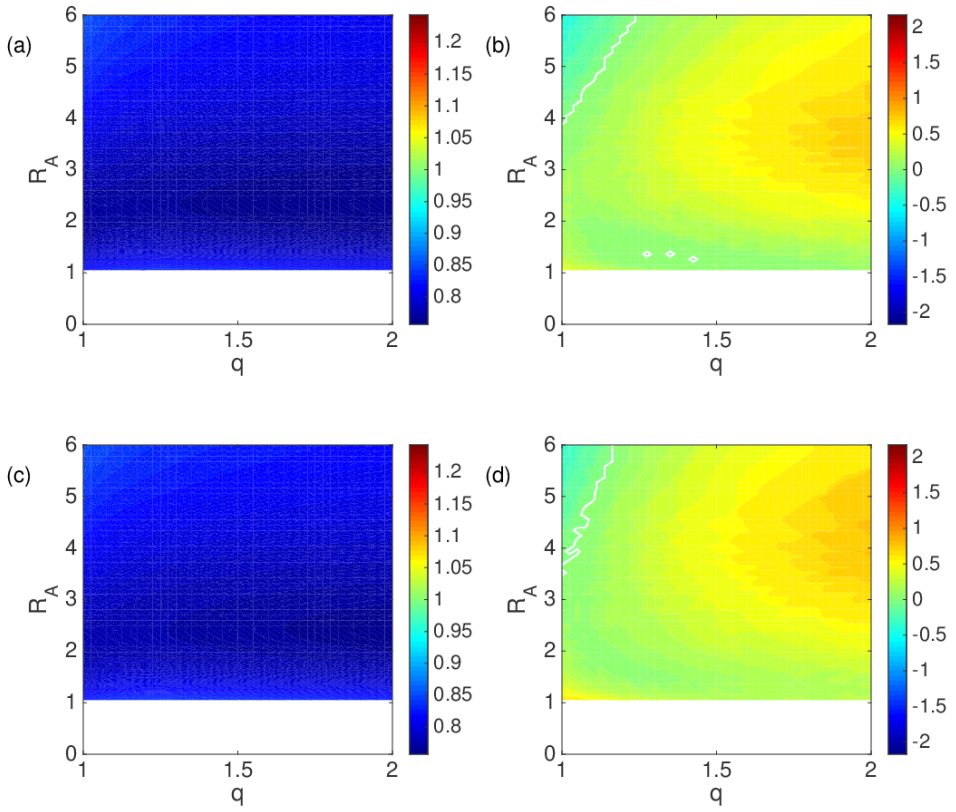

Figure 5.19: As Fig. 5.18, but for the configuration with a constant total width from Fig. 5.2(b).

changes in the difference in the duration between peak velocities, which are shown in Fig. 5.18(b) and (d) for the same basin configuration, are also small. Again, panel (b) shows results without and panel (d) with momentum sink included. Note that values larger (smaller) than zero imply a longer (shorter) transition from peak flood to peak ebb than vice versa. Hence, for a positive difference in the duration between peak velocities the net transport of fine sediment, which is mainly as suspended sediment, is flood dominant, while for negative values the net transport is ebb dominant. The region in parameter space where the net transport of suspended sediment is ebb dominant decreases slightly due to the momentum sink, indicating more flood dominant net sediment transport for fine sediments. For the

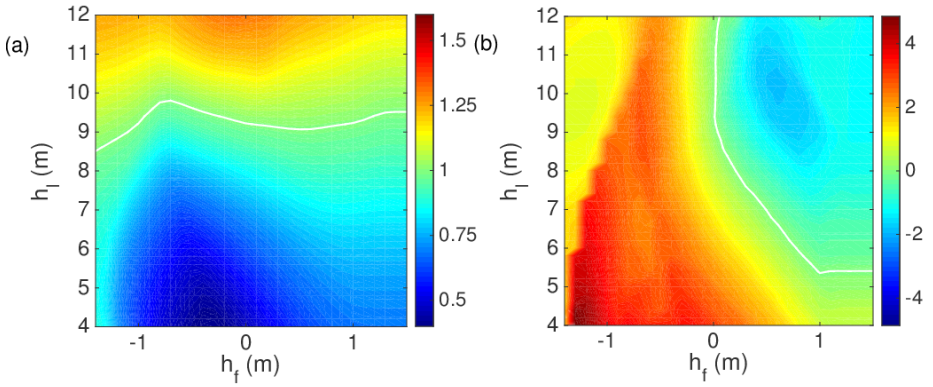

Figure 5.20: Panel (a): Dependence of the peak velocity ratio (flood to ebb) in the left channel to the depth of the left channel (h_l) and the tidal flat height (h_f). Panel (b): As panel (a), but for the difference between the transition duration from peak flood to peak ebb and vice versa in the left channel.

configuration with a constant total width, Fig. 5.19 shows the peak velocity ratio (panel a and c) and the difference in the duration between peak velocities (panel b and d). Panel (a) and (b) show results without the dissipation of along-channel momentum on the tidal flats, while panel (c) and (d) show results with the dissipation of along-channel momentum on the tidal flats. No qualitative changes between the results with and without momentum sink are observed in either of the parameters, hence no qualitative changes in the net sediment transport for either bedload or suspended load occur due to momentum sink.

5.4.4 Parallel channels: Implications for net sediment transport

For the parallel channel configuration, Fig. 5.20 shows the peak velocity ratio in panel (a) and the difference in the difference between the transition duration from peak flood to peak ebb and vice versa in panel (b). The peak velocity ratio, and consequently bedload transport, is mostly affected by the depth of the left channel, with a change from ebb to flood dominance for depths of the left channel of 9 m and deeper. On the other hand, the difference between the transition duration from peak flood to peak ebb and vice versa shows a stronger sensitivity to tidal flat height. For a tidal flat plateau below mean sea level, flood dominance occurs in the duration asymmetry, hence favoring flood directed net transport for suspended

sediment.

5.5 Conclusions

This study aimed to highlight, understand and quantitatively model two processes related to tidal flats which have received little attention in the literature. The first is the dissipation of momentum on tidal flats, which has been identified in early studies by Dronkers (1964) and Speer (1984), but has since never been investigated in depth. The second is the process of tidal flat overtopping, where a tidal flat connects two parallel channels during part of the tidal cycle. Use has been made of a cross-sectionally averaged numerical model, which parametrically accounted for both these processes.

The effect of the dissipation of momentum on the tidal flats on the tidal velocity, was shown to be sensitive to the tidal flat area, lateral tidal flat profile, as well as to the along-channel distribution of the tidal flats. The mechanisms by which the various harmonic components of the tidal velocity field were influenced, have been identified. This was achieved through an analytical representation of the momentum dissipation term, which showed that the M_6 overtide is predominantly affected in the case of wide tidal flats with a strong concave profile, while the effect on M_4 is always present for wide tidal flats, but the sign of the effect depends on the tidal flat slope. The effect of momentum sink on net transport of both coarse and fine sediment was shown to be limited. Only quantitative changes were found for net bedload transport (of coarse sediment) for an exponentially converging basin. Net suspended load transport (of fine sediment) showed more changes, with the transition from ebb dominant net sediment transport to flood dominant net sediment transport occurring for milder tidal flat slopes when considering momentum sink.

The overtopping of the tidal flats was studied for a two channel configuration, with one channel having a larger length than the other. The depth in the long channel was varied, as well as the height of the connecting tidal flat. Results indicate a clear dependence of the tidal velocity on these parameters. The ratio of peak flood to peak ebb was mostly affected by the depth of the long channel, while the difference between the durations of slack after flood and slack after ebb were affected more strongly by the tidal flat height. This suggests a different response for different sediment types to these parameters.

5.A Cross-sectionally averaged continuity and momentum equation accounting for lateral sources

To derive Eqn. (5.8), the 3D shallow water momentum and continuity equation will be integrated over a cross-section.

Continuity equation

Firstly, the cross-sectionally averaged continuity equation is derived. The continuity equation in three dimensions reads

$$\frac{\partial u'}{\partial x} + \frac{\partial v'}{\partial y} + \frac{\partial w'}{\partial z} = 0 \ , \tag{5.21}$$

where u' (v') is the velocity in the along-channel (cross-channel) direction x (y), and w' the velocity in the vertical direction z. This equation is integrated over the cross-section of the main channel, i.e. without considering the tidal flats. Firstly, the integration is done over the depth, viz.

$$0 = \int_{-h}^{\eta} \left(\frac{\partial u'}{\partial x} + \frac{\partial v'}{\partial y} + \frac{\partial w'}{\partial z} \right) dz \ .$$

This expression is expanded with the use of Leipniz' rule of integration as

$$\begin{aligned} 0 = \frac{\partial}{\partial x} \int_{-h}^{\eta} u' \ dz + \frac{\partial}{\partial y} \int_{-h}^{\eta} v' \ dz + \\ - \left(u' \Big|_{-h} \frac{\partial h}{\partial x} + u' \Big|_{\eta} \frac{\partial \eta}{\partial x} + v' \Big|_{-h} \frac{\partial h}{\partial y} + v' \Big|_{\eta} \frac{\partial \eta}{\partial y} \right) + w' \Big|_{-h}^{\eta} \ . \end{aligned}$$

Next, the bottom and surface boundary conditions ($w|_{-h} = dh/dt$ and $w|_{\eta} = d\eta/dt$, respectively) are substituted, resulting in

$$\begin{aligned} 0 &= \frac{\partial}{\partial x} \int_{-h}^{\eta} u' \ dz + \frac{\partial}{\partial y} \int_{-h}^{\eta} v' \ dz + \frac{\partial \eta}{\partial t} \ , \\ 0 &= \frac{\partial \hat{u}}{\partial x} + \frac{\partial \hat{v}}{\partial y} + \frac{\partial \eta}{\partial t} \ . \end{aligned} \tag{5.22}$$

Here, the notation has been introduced that $\int_{-h}^{\eta} \cdot \ dz = \hat{\cdot}$. Eq. (5.22) is integrated over the width of the channel only, i.e. from $-b_c/2$ to $b_c/2$. Thus, for the channel the continuity equation becomes

$$0 = \int_{-b_c/2}^{b_c/2} \left(\frac{\partial \hat{u}}{\partial x} + \frac{\partial \hat{v}}{\partial y} + \frac{\partial \eta}{\partial t} \right) \ dy \ .$$

Again, the equation is expanded using Leipniz' rule of integration as

$$0 = \frac{\partial}{\partial x}\int_{-b_c/2}^{b_c/2} \hat{u} dy + \int_{-b_c/2}^{b_c/2} \frac{\partial \eta}{\partial t} dy + \hat{v}\Big|_{-b_c/2}^{b_c/2} - \frac{1}{2}\left(\hat{u}\Big|_{-b_c/2} + \hat{u}\Big|_{b_c/2}\right)\frac{\partial b_c}{\partial x} \ . \quad (5.23)$$

Now, the second and third term on the right hand side are identified as lateral sources of water and combined in a lateral volume transport per unit of length $V_\perp$. Then the continuity equation reduces to

$$0 = \frac{\partial}{\partial x}\int_{-b_c/2}^{b_c/2} \hat{u} dy + \int_{-b_c/2}^{b_c/2} \frac{\partial \eta}{\partial t} dy + V_\perp \ .$$

Assuming lateral variability of sea surface height is negligible, the general cross-sectionally integrated continuity equation with arbitrary lateral sources and sinks becomes

$$\frac{\partial}{\partial x}\Big[b(h+\eta)u\Big] + b\frac{\partial \eta}{\partial t} + V_\perp = 0 \ , \quad (5.24)$$

with u the cross-sectionally average velocity. Eq. (5.24) is Eq. (5.8a) in the main text.

Momentum equation

The 3D shallow water momentum equation reads

$$\frac{\partial u'}{\partial t} + \frac{\partial u'u'}{\partial x} + \frac{\partial v'u'}{\partial y} + \frac{\partial w'u'}{\partial z} = -\frac{1}{\rho}\frac{\partial p}{\partial x} + \frac{1}{\rho}\frac{\partial \tau}{\partial z} \ , \quad (5.25)$$

where Eq. (5.21) has been used to write the advection terms in conservative form. Furthermore, ρ is the density (assumed constant), p the pressure and τ the shear stress in the along-channel direction. The first step is again a depth integration, which results in

$$\int_{-h}^{\eta}\left(\frac{\partial u'}{\partial t} + \frac{\partial u'u'}{\partial x} + \frac{\partial v'u'}{\partial y} + \frac{\partial w'u'}{\partial z}\right)dz = \int_{-h}^{\eta}\left(-\frac{1}{\rho}\frac{\partial p}{\partial x} + \frac{1}{\rho}\frac{\partial \tau}{\partial z}\right)dz \ . \quad (5.26)$$

This equation is expanded with the use of Leipniz' rule for integration. Additionally, the bottom and surface boundary conditions are applied and pressure is rewritten using the hydrostatic balance. Finally, a stress free surface is assumed, and a bottom shear stress τ_b is introduced. Then, Eq. (5.26) reduces to

$$\frac{\partial \hat{u}}{\partial t} + \frac{\partial \widehat{uu}}{\partial x} + \frac{\partial \widehat{vu}}{\partial y} = -g(h+\eta)\frac{\partial \eta}{\partial x} - \frac{\tau_b}{\rho} \ . \quad (5.27)$$

Now, Eqn. (5.27) is integrated over the width of the channel. This yields

$$\int_{-b_c/2}^{b_c/2}\left(\frac{\partial \hat{u}}{\partial t} + \frac{\partial \widehat{uu}}{\partial x} + \frac{\partial \widehat{vu}}{\partial y}\right)dy = \int_{-b_c/2}^{b_c/2}\left(-g(h+\eta)\frac{\partial \eta}{\partial x} - \frac{\tau_b}{\rho}\right)dy \ . \quad (5.28)$$

Again, Leipniz' rule for integration is applied to expand the integrals, and the equation evaluates as

$$\begin{aligned}\frac{\partial}{\partial t}\int_{-b_c/2}^{b_c/2}\hat{u}\;dy+\frac{\partial}{\partial x}\int_{-b_c/2}^{b_c/2}\widehat{uu}\;dy+\widehat{vu}\Big|_{-b_c/2}^{b_c/2}+\\ -\frac{1}{2}\left(\widehat{uu}\Big|_{-b_c/2}+\widehat{uu}\Big|_{b_c/2}\right)\frac{\partial b_c}{\partial x}=-gb_c(h+\eta)\frac{\partial\eta}{\partial x}-\int_{-b_c/2}^{b_c/2}\frac{\tau_b}{\rho}\;dy\;.\end{aligned}\tag{5.29}$$

Next, it is assumed that deviations of the velocity from the cross-sectional average are small, which allows to rewrite all the integrals as the product of the cross-sectional area and the averaged value. Additionally, terms 3, 4 and 5 on the right hand side in Eq. (5.29) are recognized as the lateral boundary conditions from Eq. (5.23), which are multiplied with the along-channel velocity associated with this water mass. The latter velocity is not necessarily equal to the cross-sectionally averaged velocity in the remainder of the channel. Thus, these terms are written as the product of the lateral transport $V_\perp$ with the associated along-channel velocity $u_\perp$. Finally, the width integrated bottom shear stress is approximated by a quadratic velocity term.

$$\begin{aligned}\frac{\partial}{\partial t}\Big[b_c(h+\eta)u\Big]+\frac{\partial}{\partial x}\Big[b_c(h+\eta)u^2\Big]+u_\perp V_\perp=\\ =-gb_c(h+\eta)\frac{\partial\eta}{\partial x}-bC_d|u|u\;,\end{aligned}\tag{5.30}$$

which is Eq. (5.8b) in the main text. Rewriting Eqn. (5.30) for the along-channel average velocity gives

$$\begin{aligned}b_c(h+\eta)\left(\frac{\partial u}{\partial t}+u\frac{\partial u}{\partial x}\right)+u\left(b_c\frac{\partial\eta}{\partial t}+\frac{\partial}{\partial x}b(h+\eta)u\right)+u_\perp V_\perp=\\ =-gb_c(h+\eta)\frac{\partial\eta}{\partial x}-b_cC_d|u|u\;,\end{aligned}\tag{5.31}$$

which is simplified by using Eq. (5.24) to

$$\frac{\partial u}{\partial t}+u\frac{\partial u}{\partial x}+\frac{(u_\perp-u)}{b_c(h+\eta)}V_\perp=-g\frac{\partial\eta}{\partial x}-\frac{C_d|u|u}{h+\eta}\;.\tag{5.32}$$

Chapter 6

Summary & Outlook

6.1 Main findings

In this chapter the main conclusions of the research that has been presented in this thesis will be summarized. The answers to the research questions, which were formulated in chapter 1, will be given. These questions were the following,

1. Through which mechanism do secondary channels dampen or amplify the tide in a main channel? And how does the damping or amplification quantitatively depend on the characteristics (position, geometry, etc.) of the secondary channel in the main channel?

2. What impact does a secondary channel have on the non-linear characteristics of the tide in the main channel, viz. the tidal range, the duration between high water and low water, the flood-to-ebb ratio and the duration between peak flood and peak ebb currents? How will the changes in tidal currents affect the net transport of coarse and fine sediment?

3. How do river-tide interactions and residual tidal currents quantitatively affect tides, as well as the net water transport in an estuarine network? What changes occur in the tides and in the net water transport for different amounts of river discharge and/or different geometrical configurations?

4. What influence does the dissipation of momentum on tidal flats have on the non-linear characteristics of the tidal velocity (as specified in question 2) in the channel? Similarly, what is the effect of the exchange of mass and momentum through overtopping between two channels that are separated by a tidal flat on non-linear tidal velocity in the channels? What are the implications for the net transport of coarse and fine sediment in these channels due to these processes?

Next, in section 6.2, suggestions for improvements and further research will be given.

6.1.1 Chapter 2: Influence of a secondary channel on tidal range in a main channel

An analytical model of the linear cross-sectionally averaged shallow water equations was developed and studied. The model described tidal motion in a network comprising a main channel and a secondary channel. The results gave a quantitative and qualitative assessment on the influence of the geometry of the secondary channel on the amplitude and phase of the tidal wave in the tidal network. This was done by defining an amplitude ratio, which is the ratio of the local sea surface height amplitude in the network with and without the secondary channel.
Assuming friction to be weak compared to inertia, the length of the main channel to be of the order of the tidal wavelength and the secondary channel to be short compared to the tidal wavelength, damping of the tide occurs if the secondary channel is positioned between a node and the successive landward antinode of the tide. For positions between the node and the next seaward node, amplification of the tide is found. In the former case, flood velocities in the main channel coincide with flood velocities in the secondary channel near the vertex, while in the later case ebb velocities in the main channel coincide with flood velocities in the secondary channel near the vertex. When velocities are in phase, during flood tides part of the water is stored in the secondary channel, while this is released again during ebb. If velocities are out of phase the opposite occurs, meaning additional water gets trapped landward of the vertex point.
When relaxing the assumptions on friction and the length of the main and secondary channel, it was still found that location and dimension of the secondary channel significantly affect the modulation of the tidal range. Increasing friction favours damping of the tide, eventually causing the positions where the secondary channel results in amplification of the tide to vanish. The amplitude ratio is proportional to the width of the secondary channel, meaning that the effect of the secondary channel (damping or amplification) is only enhanced, but not altered by the width of the secondary channel. An increase in friction in the main channel, as well as a reduction in length of the main channel reduces the spatial variation in the amplitude ratio. The results remain qualitatively unchanged when depth varies mildly in the channels, or when the shape of the secondary channel is changed.

6.1.2 Chapter 3: Influence of a secondary channel on non-linear tidal characteristics and net sediment transport in a main channel

This chapter expanded the results from chapter 2, by considering a non-linear model. The equations were solved numerically, using the method of characteristics. A comparison was made of tidal characteristics for a main channel with and

without a secondary channel. In this study, the amplitude and phase of both the sea surface height and velocity of the semi-diurnal tidal component were investigated. However, now for both sea surface height and velocity. Moreover, the M_4 and M_6 harmonic component were studied, as well as the tidal range, the duration of the falling tide, the peak flood to peak ebb velocity ratio, and the difference in the durations between peak velocities. The latter two quantities are important parameters for net bedload and suspended load sediment transport, respectively.
Each of the harmonic components of the sea surface height experiences the same amplification mechanism as that identified in chapter 2. This shows that the secondary channel locally generates a secondary tidal wave and it subsequently propagates away from the secondary channel into the main channel. Differences between the linear model and the non-linear model were also identified. For example, a spatially non-uniform response in the amplitude ratios (i.e. the ratio of the local amplitude of a harmonic component in the presence and absence of the secondary channel) was found with the non-linear model landward of the secondary channel. These ratios were uniform in the linear model. This results from the fact that the velocity field has changed due to the presence of the secondary tidal wave. As a result, friction changes due to the presence of a secondary channel in the non-linear model, but not in the linear model where friction was kept constant. Changes in the tidal range revealed a spatially non-uniform response in the main channel landward of the secondary channel, which was also caused by changes in friction.
The presence of a secondary channel causes only small changes in the non-linear velocity characteristics, viz. the peak flood to peak ebb velocity ratio and the difference in durations between peak velocities, in the main channel. In the investigated set-up, the flood to ebb velocity ratio changed insufficiently to alter the direction of the net bedload transport of sediment. Changes in the difference in duration between peak velocities due to the presence of the secondary channel were stronger. This result suggests that suspended load transport might be more susceptible to the presence of a secondary channel. Particularly at a distance approximately a quarter of the M_4 tidal wavelength seaward of the secondary channel, the difference in duration between peak velocities changes strongly. Moreover, when the secondary channel is positioned near the landward boundary of the main channel, an increase in the duration between maximum flood and maximum ebb is observed in a large area. This might change the direction of the net suspended sediment transport.

6.1.3 Chapter 4: Influence of river discharge and geometry on tides and net water transport in estuarine networks

In this chapter, it was investigated what the influence of changes in river discharge and geometry are on the tidal wave propagation and on the net water transport in complex estuarine networks, using the Yangtze estuary as an example. To this end, a semi-analytical model was developed that solves the non-linear cross-sectionally averaged shallow water equations. Solutions were constructed using a truncated harmonic expansion of the system variables (sea surface height and velocity) and a subsequent perturbation series in a small parameter, viz. the ratio between sea surface height variations and water depth.

The model was used to simulate four scenarios, viz. for conditions in the wet and dry season, after and before construction of the deepwater navigation channel, a large scale human intervention. The setting with a navigation channel during the dry season was used as a default. Modelled sea surface height for this scenario was compared to observed sea surface height at 16 tidal stations, and fair agreement was found. The model showed that increasing river discharge to levels representative for the wet season decreases the semi-diurnal tidal amplitude due to enhanced friction, while quarter diurnal tidal amplitudes increase due to enhanced river-tide interactions. It was further shown that the relative distribution of river induced net water transport, as well as the residual transport induced by nonlinear tidal rectification are only weakly sensitive to changes in river discharge. Nevertheless, the ratio between residual transport induced by nonlinear tidal rectification and the river induced transport is highly dependent on the season. Consequently, there is a strong seasonal cycle in net water transport.

Comparing the model runs from before and after construction of the deepwater navigation channel showed that tidal currents increased due to the human intervention, while tidal sea surface elevation amplitudes decreased. Net water transport through the North Passage became smaller after construction of the deepwater navigation channel. Partly as a direct result of changes in the net water transport division between the North Passage and South Passage, but also in part due to a remote effect of the deepwater navigation channel, resulting in less net water transport through the South Channel.

In single channel estuaries, the return current associated with landward directed Stokes transport by the tidal wave is important in producing cross-sectionally averaged (seaward) velocities. This study showed that in an estuarine network other nonlinear processes, such as horizontal advection of momentum, are equally important in determining the residual transport induced by nonlinear tidal rectification. Two terms were identified that received little attention in earlier literature, viz. the continuity of dynamic pressure at vertex points where channels are connected and the interaction between residual and quarter diurnal currents through the

quadratic bottom stress. Continuity of dynamic pressure is an extension of the general assumption of continuity of sea surface elevation at vertex points. The interaction between residual and quarter diurnal currents was found by linearizing the quadratic bottom stress with the use of Chebyshev polynomical.
A further comparison was made between the semi-analytical model and a numerical model that solves the same equations as the semi-analytical model, but using quadratic friction and without imposing conditions on the number of harmonics and the ratio of tidal amplitude and channel depth. By comparing results from the semi-analytical model including and excluding the coupling between residual and quarter diurnal currents with the numerical model, it was shown that the applied linearization procedure of the quadratic bottom stress provides a significant source of residual and quarter diurnal currents, which strongly control the net water transport and tidal dynamics in the Yangtze estuary.

6.1.4 Chapter 5: Tidal flats: Effect of momentum sink and overtopping on non-linear tidal velocity characteristics and net sediment transport

Chapter 5 highlighted the importance of two processes related to tidal flats, which have not been considered in much detail in literature. These processes are the dissipation of along-channel momentum on the tidal flats and the overtopping of water over intertidal areas. Overtopping occurs in systems with parallel channels, which are only connected during high water, such as in the Ems estuary and the Yangtze estuary.
The effect of these processes on the non-linear velocity characteristics (the flood to ebb ratio and the difference in duration between peak velocities) and the net transport of coarse and fine sediment has been investigated with the use of a numerical model that solves the non-linear cross-sectionally averaged shallow water equations. Both processes were accounted for through parameterizations of lateral transport of mass and momentum from channels to flats and vice versa in the governing equations. Momentum sink was investigated for a single channel configuration reminiscent of the Ameland inlet, with varying tidal flat area and varying lateral profiles of the tidal flats. Moreover, two different distributions of tidal flats along the channel were considered. First, tidal flat width was assumed to converge identical to the tidal channel. Second, the basin width, i.e. the combined width of the channel and tidal flats, was taken constant. As a result, the amount of tidal flats increased towards the closed end of the channel. To study the effect of exchanging mass and momentum through overtopping between channels connected by a tidal flat, a configuration similar to the upstream part of the Ems estuary was constructed, which comprised of a long channel representing the Ems river and a short wide basin, representing the Dollart basin. Here, the depth of the

long channel was varied, as well as the height of the tidal flat, thus determining the duration over which the two channels were connected during a tidal cycle.
Momentum sink was shown to reduce the M_2 tidal velocity more strongly for increasing tidal flat area and more concave shapes of the tidal flat. Similarly, M_6 velocities also decrease more strongly for increasing intertidal area and increasing concavity. For M_4, an increase in velocities occurs for strongly concave tidal flats, which becomes larger for larger intertidal areas. However, for linear tidal flats, the M_4 velocities decrease. The different responses of the harmonic components to momentum sink were explained through an analytical treatment of the momentum sink term in the momentum equation.
The exchange of mass and momentum through overtopping between channels separated by a tidal flat was also shown to influence tidal velocity. Semi-diurnal velocity amplitude in the long channel was shown to decrease due to the overtopping for any depth of this channel, while the quarter diurnal currents in the long channel mostly increased. The M_6 currents in the long channel mostly increased for tidal flat heights above the undisturbed water depth, and mostly decreased for tidal flat heights below the undisturbed water depth. For increasing depth of the long channel, the ratio of peak flood velocity to peak ebb velocity increased, rendering the tidal current flood dominant instead of ebb dominant for increasing depth in the long channel. Net bedload transport is strongly determined by the peak velocity ratio. Hence, net bedload transport also changes from ebb to flood dominant when the channel depth increases. The peak velocity ratio remained relatively unaffected by changes in tidal flat height. Thus, net bedload transport is insensitive to tidal flat height. Contrary to this, the difference in duration between the peak velocities was more sensitive to changes in tidal flat height than to changes in depth of the long channel. The duration difference changes from positive to negative values for higher tidal flat heights, which indicates a change from a longer transition between flood and ebb than the other way around, to a longer transition between ebb and flood. As fine sediment settles down during periods of slow currents, the duration of the transition between peak currents is an important indicator for net suspended sediment transport. Thus, increasing the tidal flat height also results in a change from flood to ebb dominance in the net transport direction of fine sediments.

6.2 Future recommendations

6.2.1 Secondary channels

The models used in chapters 2 and 3 have provided insight into the mechanisms by which the secondary channels influence the tidal wave, and have shown potential

for secondary channels to be implemented in estuaries to reduce tidal range, such as currently being considered in the Ems estuary. To expand the insight, some extensions to the models are worthwhile to be made. For example, considering width convergence and depth variations allows for a more accurate representation of an estuary. Moreover, Roos & Schuttelaars (2015) showed that different boundary conditions on the seaward boundary result in slightly different main channel responses. In the approach of this thesis, the incoming tidal wave was assumed to be unaffected by the changes inside the main channel, which is a valid approach when modelling only an upstream part of a tidal channel. However, when modelling a tidal channel all the way to the open ocean, a fixed sea surface elevation is a more appropriate boundary condition. Additionally, Roos & Schuttelaars (2015) also studied the effect that multiple secondary channels have on the tide in the main channel. Finally, before a secondary channel gets implemented in a system, its effects should be studied in detail using a more sophisticated numerical model. This allows to study the effect of the secondary channel on, e.g., morphodynamics, ecology and salinity intrusion. The results from the idealized models are useful to identify the most feasible scenarios.

6.2.2 Tides and the division of net water transport in estuarine networks

Despite identifying a number of key processes that determine the division of net water transport in an estuarine network, there are several more processes which also influence this distribution. Particularly, Li *et al.* (2010) showed with a complex numerical model that the influence of wind and the spring-neap cycle is important. They also accounted for salinity gradients and density induced currents, but they did not isolate the effect of density induced currents by considering a model run without density gradients. These (and other) processes (spring-neap variations, wind, salinity, and diurnal variability) can also be studied in a more idealized setting as used in chapter 4. It is important to study how these processes compare to the previously identified processes. In particular, this allows to distinguish the separate effect of individual processes. For salt, this includes the directly driven gravitational circulation (Hansen & Rattray, 1965), but also the residual flow that results from asymmetric mixing due to tidal straining (Jay & Musiak, 1996; Burchard & Hetland, 2010; Cheng *et al.*, 2010; Stacey *et al.*, 2010). For computations on salinity intrusion a 2DV approach like that in McCarthy (1993) is recommended. However, expanding the model with a salt transport equation to investigate salinity intrusion poses additional difficulties. For salt (or any other constituent), matching conditions have to be formulated, which govern the distribution of the constituent at a vertex point where channels connect. While these have been investigated for uni-directional (river) flow (cf. Wang *et al.*, 1995; Klein-

hans *et al.*, 2008), they remain unknown for oscillatory currents.
Results from this model suggest measures for persistent problems observed in the Yangtze Estuary, such as the small net water transport through North Branch, and the siltation of the North Passage. The former is caused by a small river induced seaward transport, which is balanced to a great extent by a landward transport due to non-linear tidal rectification. Thus, solutions to this problem consist of changing either one of these transports. The division of river induced transport is strongly determined by the cross-section of the channels at the vertex, hence a solution might be to increase the cross-section of the North Branch at the vertext point with the Yangtze River and South Branch. Similarly, siltation in the North Passage could be reduced by increasing the flushing capacity of the channel by increasing river induced transport in this channel. However, for sediment transport there are many more transport processes, so for a thorough solution studies with complex numerical models are needed. Again, the results of the model discussed here are useful to design the most feasible scenarios.

6.2.3 Tidal flats; momentum sink and overtopping

The model configuration used for studying the effect of momentum sink on the tidal flats was respresentative for the Ameland inlet. As such, only one channel length was considered. Ridderinkhof *et al.* (2014) showed that for the effect of temporary mass storage on the tidal flats, the length of the main channel is of high importance. Thus, performing a sensivity study on the length of the channel would be a valuable extension of the results.
The treatment of the exchange of mass and momentum through overtopping between two channels separated by a tidal flat in chapter 5 studies a particular configuration where two channels are parallel for only a part of their length. It is also of interest to conduct a study on this process considering different configurations. For example, in the Yangtze estuary and Western Scheldt, channels are oriented parallel to each other until they merge and continue as a single channel. This will lead to different dynamics and might result in different effects on the sediment transport for such situations. Additionally, the overtopping between channels was instantaneous, while in nature the water is also temporarily stored on the tidal flat (as in the single channel configuration). More sophisticated parameterizations to incorporate this process provide additional insight in the exchange of mass and momentum. To obtain these parameterizations, studies on the tidal flow over tidal flats has to be carried out. First steps have been made by van Oyen *et al.* (2012), who created an idealized model of a short channel with an adjacent tidal flat.
Furthermore, water that is exchanged between channels in an estuary carries with it the salinity of the channel of origin. This has a strong effect on the salinity intrusion and subsequent mixing, as shown by Hamilton (1990). Additionally, it

also affects the density driven circulation, particularly that associated with an asymmetric mixing between tidal periods, by providing a source or sink of stratification at an arbitrary phase during the tidal cycle (Stacey *et al.*, 2008).
The model was used to investigate the effect of removing or installing a barrier between two channels on the tidal hydrodynamics, e.g., the Geise-Leit dam in the Ems estuary or the deepwater navigation channel in the Yangtze estuary. The results for the Ems estuary, on which the model configuration was inspired, seem to suggest that net suspended transport might become ebb dominant if the barrier between the Ems river and Dollart is made less permiable. Thus increasing the communication between the Ems river and the Dollart basin might be an option to reduce the high sediment concentrations in the Ems estuary.

Bibliography

Alebregtse, N. C. & de Swart, H. E. 2014 Effect of a secondary channel on the non-linear tidal dynamics in a semi-enclosed channel: a simple model. *Ocean Dynamics* **64** (4), 573–585.

Alebregtse, N. C., de Swart, H. E. & Schuttelaars, H. M. 2013 Resonance characteristics of tides in branching channels. *Journal of Fluid Mechanics* **728** (R3).

Aubrey, D. G. 1986 Hydrodynamic controls on sediment transport in well-mixed bays and estuaries. In *Physics of Shallow Estuaries and Bays, Lecture Notes Coastal Estuarine Studies* (ed. J. van de Kreeke), , vol. 16, pp. 245–258. AGU.

Bolla-Pittaluga, M., Repetto, R. & Tubino, M. 2003 Channel bifurcation in braided rivers: Equilibrium configurations and stability. *Water Resources Research* **39** (3), 1046.

Boon, J. D. & Byrne, R. J. 1981 On basin hypsometry and the morphodynamic response of coastal inlet systems. *Marine Geology* **40**, 27–48.

Brown, J. M. & Davies, A. G. 2010 Flood/ebb tidal asymmetry in a shallow sandy estuary and the impact on net sand transport. *Geomorphology* **114**, 431–439.

Buchwald, V. T. 1971 The diffraction of tides by a narrow channel. *Journal of Fluid Mechanics* **46** (3), 501–511.

Burchard, H. 2002 *Applied turbulence modelling in marine waters*. Springer-Verlag.

Burchard, H. & Hetland, R. D. 2010 Quantifying the contributions of tidal straining and gravitational circulation to residual circulation in periodically stratified tidal estuaries. *Journal of Physical Oceanography* **40**, 1243–1262.

Buschman, F. A., Hoitink, A. J. F., van der Vegt, M. & Hoekstra, P. 2009 Subtidal water level variation controlled by river flow and tides. *Water Resources Research* **45** (W10420).

BUSCHMAN, F. A., HOITINK, A. J. F., VAN DER VEGT, M. & HOEKSTRA, P. 2010 Subtidal flow division at a shallow tidal junction. *Water Resources Research* **46**, W12515.

CAI, H., SAVENIJE, H. H. G. & TOFFOLON, M. 2014 Linking the river to the estuary: influence of river discharge on tidal damping. *Hydrology and Earth System Sciences* **18**, 287–304.

CHEN, Z., LI, J., SHEN, H. & ZHANGHUA, W. 2001 Yangtze River of China: historical analysis of discharge variability and sediment flux. *Geomorphology* **41** (2-3), 77–91.

CHENG, P., VALLE-LEVINSON, A. & DE SWART, H. E. 2010 Residual currents induced by asymmetric tidal mixing in weakly stratified narrow estuaries. *Journal of Physical Oceanography* **40**, 2135–2147.

CHERNETSKY, A. S., SCHUTTELAARS, H. M. & TALKE, S. A. 2010 The effect of tidal asymmetry and temporal settling lag on sediment trapping in estuaries. *Ocean Dynamics* **60**, 1219–1241.

DEFANT, A. 1961 *Physical oceanography, vol. 2*. New York: Pergamon Press.

DONNER, M., LADAGE, F., STOSCHEK, O. & NGUYEN, H. 2012 Methods and analysis tools for redevelopments in an estuary with high suspended sediment concentrations. In *Coastal Engineering* (ed. P. Lynett & J. McKee Smith), *Proceedings of the 33rd International Conference*, vol. 1, p. 55. Coastal Engineering Research Council.

DRONKERS, J. 1986 Tidal asymmetry and estuarine morphology. *Netherlands Journal of Sea Research* **20** (2/3), 117–131.

DRONKERS, J. J. 1964 *Tidal computations in rivers and coastal waters*. Amsterdam: North-Holland Publ. Co.

DRONKERS, J. J. 2005 Dynamics of coastal systems. In *Advanced series on ocean engineering*, 1st edn. (ed. T.K. Wei), , vol. 25. World Scientific.

DYER, K. R. 1986 *Coastal and Estuarine Sediment Dynamics*. John Wiley & Sons.

FERREL, W. 1874 *Tidal researches*. Washington: Government printing office.

FLICK, R. E., MURRAY, J. F. & EWING, L. C. 2003 Trends in United States tidal datum statistics and tide range. *Journal of Waterway, Port, Coastal and Ocean Engineering* **129** (4), 155–164.

FRIEDRICHS, C. T. 2010 Barotropic tides in channelized estuaries. In *Contemporary Issues in Estuarine Physics* (ed. A. Valle-Levinson), chap. 3, pp. 27–61. Cambridge University Press Cambridge,.

FRIEDRICHS, C. T. 2011 Tidal flat morphodynamics: A synthesis. In *Treatise on estuarine and coastal science: sedimentology and geology* (ed. B. W. Flemming & J. D. Hansom), , vol. 3, pp. 137–170. Burlington, Mass.: Elsevier Science.

FRIEDRICHS, C. T. & AUBREY, D. G. 1988 Non-linear tidal distortion in shallow well-mixed estuaries: a synthesis. *Estuarine, Coastal and Shelf Science* **27**, 521–545.

FRIEDRICHS, C. T. & AUBREY, D. G. 1994 Tidal propagation in strongly convergent channels. *Journal of Geophysical Research* **99**, 3321–3336.

FRIEDRICHS, C. T. & AUBREY, D. G. 1996 Uniform bottom shear stress and equilibrium hypsometry of intertidal flats. In *Coastal and Estuarine Studies* (ed. C. Pattiaratchi), pp. 405–429. Washington, D.C.: American Geophysical Union.

GAO, M., FAN, Q., TAN, Z. & ZHENG, W. 2009 Research on bifurcation ratio in the North Passage of Yangtze Estuary. *Port & Waterway Engineering* **427**, 82–86, (in Chinese, with English Abstract).

GARRETT, C. 1975 Tides in gulfs. *Deep-Sea Research* **22**, 23–35.

GEYER, W. R. & MACCREADY, P. 2014 The estuarine circulation. *Annual Review of Fluid Mechanics* **46**, 175–197.

GODIN, G. 1991 Compact approximations to the bottom friction term, for the study of tides propagating in channels. *Continental Shelf Research* **11** (7), 579–589.

GODIN, G. 1999 The propagation of tides up rivers with special considerations on the Upper Saint Lawrence River. *Estuarine, Coastal and Shelf Science* **48**, 307–324.

GROEN, P. 1967 On the residual transport of suspended matter by an alternating tidal current. *Netherlands Journal of Sea Research* **3**, 564–574.

GUHA, A. & LAWRENCE, G. A. 2013 Estuary classification revisited. *Journal of Physical Oceanography* **43**, 1566–1571.

GUO, L., VAN DER WEGEN, M., JAY, D. A., MATTE, P., WANG, Z.-B., ROELVINK, J. A. & HE, Q. 2015 River-tide dynamics: exploration of non-stationary and non-linear tidal behavior in the Yangtze River estuary. *Journal of Geophysical Research: Oceans* .

HAMILTON, P. 1990 Modelling salinity and circulation for the Columbia river estuary. *Progress in Oceanography* **25**, 113–156.

HANSEN, D. V. & RATTRAY, M. 1965 Gravitational circulation in straits and estuaries. *Journal of Marine Research* **23** (2), 104–122.

HE, Q., LI, J., LI, Y., JIN, X. & CHE, Y. 2001 Field measurements of bottom boundary layer processes and sediment resuspension in the Changjiang Estuary. *Science in China Series B: Chemistry* **44** (1), 80–86.

HILL, A. E. & SOUZA, A. J. 2006 Tidal dynamics in channels: 2. complex channel networks. *Journal of Geophysical Research* **111** (C11021).

HU, K. & DING, P. 2009 The effect of Deep Waterway Constructions on hydrodynamics and salinities in Yangtze Estuary, China. *Journal of Coastal Research* **2** (SI 56 (Proceedings of the 10th International Coastal Symposium)), 961–965.

IANNIELLO, J. P. 1977 Tidally induced residual currents in estuaries of constant breadth and depth. *Journal of Marine Research* **35**, 755–786.

JAY, D. A. & MUSIAK, J. D. 1996 Internal tidal asymmetry in channel flows: origins and consequences. In *Mixing in Estuaries and Coastal Seas* (ed. C. Pattiaratchi), *Coastal and Estuarine Studies*, vol. 50, chap. 13. American Geophysical Union.

JIANG, C., LI, J. & DE SWART, H. E. 2012 Effects of navigational works on morphological changes in the bar area of the Yangtze Estuary. *Geomorphology* **139-140**, 205–219.

JIANG, C., DE SWART, H. E., LI, J. & LIU, G. 2013 Mechanisms of along-channel sediment transport in the North Passage of the Yangtze Estuary and their response to large-scale interventions. *Ocean Dynamics* **63**, 283–305.

DE JONG, M. P. C. & BATTJES, J. A. 2004 Low-frequency sea waves generated by atmospheric convection cells. *Journal of Geophysical Research* **109** (C01011).

DE JONGE, V. N. 1992 Tidal flow and residual flow in the Ems Estuary. *Estuarine, Coastal and Shelf Science* **34**, 1–22.

DE JONGE, V. N. 2000 Importance of temporal and spatial scales in applying biological and physical process knowledge in coastal management, an example for the Ems estuary. *Continental Shelf Research* **20** (12-13), 1655–1686.

DE JONGE, V. N., SCHUTTELAARS, H. M., BEUSEKOM, J. E. E., TALKE, S. A. & DE SWART, H. E. 2014 The influence of channel deepening on estuarine turbidity levels and dynamics, as exemplified by the Ems estuary. *Estuarine, Coastal and Shelf Science* **139**, 46–59.

KANG, S. K., FOREMAN, M. G. G., LIE, H.-J., LEE, J.-H., CHERNIAWSKY, J. & YUM, K.-D. 2002 Two-layer tidal modeling of the Yellow and East China Seas with application to the seasonal variability of the M_2 tide. *Journal of Geophysical Research* **107** (C3).

KINSLER, L. E., FREY, A. R., COPPENS, A. B. & SANDERS, J. V. 2000 *Fundamentals of acoustics*, 4th edn. John Wiley & Sons.

KLEINHANS, M. G., JAGERS, H. R. A., MOSSELMAN, E. & SLOFF, C. J. 2008 Bifurcation dynamics and avulsion duration in meandering rivers by one-dimensional and three-dimensional models. *Water Resources Research* **44**, W08454.

VAN DE KREEKE, J. 1988 Hydrodynamics of tidal inlets. In *Hydrodynamics and sediment dynamics of tidal inlets* (ed. D.G. Aubrey & L. Weishar), *Lecture Notes on Coastal and Estuarine Studies*, vol. 29, pp. 1–23. Springer New York.

VAN DE KREEKE, J. & ROBACZEWSKA, K. 1993 Tide-induced residual transport of coarse sediment; application to the ems estuary. *Netherlands Journal of Sea Research* **31** (3), 209–220.

LANZONI, S. & SEMINARA, G. 1998 On tide propagation in convergent estuaries. *Journal of Geophysical Research* **103**, 30.793–30.812.

LI, L., ZHU, J. & WU, H. 2012 Impacts of wind stress on saltwater intrusion in the Yangtze Estuary. *Science China Earth Sciences* **55** (7), 1178–1192.

LI, L., ZHU, J., WU, H. & GUO, Z. 2014 Lateral saltwater intrusion in the North Channel of the Changjiang Estuary. *Estuaries and Coasts* **37**, 36–55.

LI, L., ZHU, J., WU, H. & WANG, B. 2010 A numerical study on water diversion ratio of the Changjian (Yangtze) estuary in dry season. *Chinese Journal of Oceanology and Limnology* **28** (3), 700–712.

LIGHTHILL, J. 1978 *Waves in fluids*. Cambridge University Press.

LONGUET-HIGGINS, M. S. 1953 Mass transport in water waves. *Philosophical Transactions of the Royal Society of London. Series A, Mathematical and Physical Sciences* **245** (903), 535–581.

LORENTZ, H. A. 1922 Het in rekening brengen van den weerstand bij schommelende vloeistofbewegingen. *De Ingenieur* **37**, 695.

LORENTZ, H. A. 1926 *Verslag staatscommissie Zuiderzee 1918-1926*. 's Gravenhage: Algemeene Landsdrukkerij, (in Dutch).

MA, G., SHI, F., LIU, S. & QI, D. 2011 Hydrodynamic modeling of Changjiang Estuary: Model skill assessment and large-scale structure impacts. *Applied Ocean Research* **33**, 69–78.

MANOJ, N. T., UNNIKRISHNAN, A. S. & SUNDAR, D. 2009 Tidal asymmetry in the mandovi and zuari estuaries: A case study. *Journal of Coastal Research* **25** (6), 1187–1197.

MCCARTHY, R. K. 1993 Residual currents in tidally dominated, well-mixed estuaries. *Tellus A* **45**, 325–340.

MEI, C. C., STIASSNIE, M. & YUE, D. K. P. 2005 *Theory and Applications of Ocean Surface Waves: Linear aspects*, *Advanced series on ocean engineering*, vol. 23. World Scientific.

MILES, J. W. 1971 Resonant response in harbours: an equivalent-circuit analysis. *Journal of Fluid Mechanics* **26** (2), 241–265.

NATIONAL MARINE DATA AND INFORMATION SERVICE, ed. 2013 *Tide Tables 2014*, , vol. 2 From the Changjiang River Mouth to the Taiwan Straits. China Ocean Press (in Chinese).

VAN OYEN, T., LANZONI, S., D'ALPAO, A., TEMMERMAN, S., TROCH, P. & CARNIELLO, L. 2012 A simplified model for frictionally dominated tidal flows. *Geophysical Research Letters* **39** (L12403).

PARKER, B. B. 1991 The relative importance of the various nonlinear mechanisms in a wide range of tidal interactions (review). In *Tidal Hydrodynamics* (ed. B. B. Parker), pp. 237–268. New York: John Wiley & Sons.

PLATZMAN, G. W. 1971 Ocean tides and related waves. In *Lectures in Applied Mathematics*, , vol. 14. Washington, D.C.: American Mathematical Society.

POSTMA, H. 1961 Transport and accumulation of suspended matter in the Dutch Wadden Sea. *Netherlands Journal of Sea Research* **1**, 148–190.

PRANDLE, D. & RAHMAN, M. 1980 Tidal response in estuaries. *Journal of Physical Oceanography* **10**, 1552–1573.

PRITCHARD, D. W. 1967 What is an estuary: physical viewpoint. In *Estuaries*, *AAAS publication* 83, pp. 3–5. American Association for the Advancement of Science.

VAN PROOIJEN, B. C. & WANG, Z.-B. 2013 A 1D model for tides waves and fine sediment in short tidal basins – Application to the Wadden Sea. *Ocean Dynamics* **63**, 1233–1248.

RAINEY, R. C. T. 2009 The optimum position for a tidal power barrage in Severn estuary. *Journal of Fluid Mechanics* **636**, 497–507.

RIDDERINKHOF, H. 1988 Tidal and residual flows in the western Dutch Wadden Sea II: An analytical model to study the constant flow between connected basins. *Netherlands Journal of Sea Research* **22** (3), 185–198.

RIDDERINKHOF, W., DE SWART, H. E., VAN DER VEGT, M., ALEBREGTSE, N. C. & HOEKSTRA, P. 2014 Geometry of tidal basin systems: A key factor for the net sediment transport in tidal inlets. *Journal of Geophysical Research: Oceans* **119**.

ROOS, P. C. & SCHUTTELAARS, H. M. 2015 Resonance properties of tidal channels with multiple retention basins: role of adjacent sea. *Ocean Dynamics* **65**, 311–324.

SASSI, M. G., HOITINK, A. J. F., DE BRYE, B., VERMEULEN, B. & DELEERSNIJDER, E. 2011 Tidal impact on the division of river discharge over distributary channels in the Mahakam delta. *Ocean Dynamics* **61**, 2211–2228.

SCHUTTELAARS, H. M., DE JONGE, V. N. & CHERNETSKY, A. S. 2013 Improving the predictive power when modelling physical effects of human interventions in estuarine systems. *Ocean & Coastal Management* **79**, 70–82.

SCHUTTELAARS, H. M. & DE SWART, H. E. 2000 Multiple morphodynamic equilibria in tidal embayments. *Journal of Geophysical Research* **105** (C10), 24.105–24.118.

SPEER, P. E. 1984 Tidal distortion in shallow estuaries. PhD thesis, MIT/WHOI, WHOI-84-25.

SPEER, P. E. & AUBREY, D. G. 1985 A study of non-linear tidal propagation in shallow inlet/estuarine systems. Part II: Theory. *Estuarine, Coastal and Shelf Science* **21**, 207–224.

STACEY, M. T., BRENNAN, M. L., BURAU, J. R. & MONISMITH, S. G. 2010 The tidally averaged momentum balance in a partially and periodically stratified estuary. *Journal of Physical Oceanography* **40**, 2418–2434.

STACEY, M. T., FRAM, J. P. & CHOW, F. K. 2008 Role of tidally periodic density stratification in the creation of estuarine subtidal circulation. *Journal of Geophysical Research* **113** (C08016).

VAN STRAATEN, L. M. J. U. & KUENEN, PH. H. 1957 Accumulation of fine grained sediments in the Dutch Wadden Sea. *Geologie en Mijnbouw* **19**, 329–354.

DE SWART, H. E. & ZIMMERMAN, J. T. F. 2009 Morphodynamics of tidal inlet systems. *Annual Review of Fluid Mechanics* **41**, 203–229.

TALKE, S. A., DE SWART, H. E. & DE JONGE, V. N. 2009*a* An idealized model and systematic process study of oxygen depletion in highly turbid estuaries. *Estuaries and Coasts* **32**, 602–620.

TALKE, S. A., DE SWART, H. E. & SCHUTTELAARS, H. M. 2009*b* Feedback between residual circulations and sediment distribution in highly turbid areas: An analytical model. *Continental Shelf Research* **29**, 119–135.

TOFFOLON, M., VIGNOLI, G. & TUBINO, M. 2006 Relevant parameters and finite amplitude effects in estuarine hydrodynamics. *Journal of Geophysical Research* **111** (C10014).

VALLE-LEVINSON, A., ed. 2010 *Contemporary Issues in Estuarine Physics*. Cambridge, UK: Cambridge University Press.

VELLINGA, N. E., HOITINK, A. J. F., VAN DER VEGT, M., ZHANG, W. & HOEKSTRA, P. 2014 Human impacts on tides overwhelm the effect of sea level rise on extreme water levels in the Rhine-Meuse delta. *Coastal Engineering* **90**, 40–50.

WANG, Z.-B., DE VRIES, M., FOKKINK, R. J. & LANGERAK, A. 1995 Stability of river bifurcations in 1D morphodynamic models. *Journal of Hydraulic Research* **33**, 739–750.

WHITHAM, G. B. 1974 *Linear and nonlinear waves*. *Pure and applied mathematics* 42. John Wiley & Sons.

WINTERWERP, J. C. & WANG, Z.-B. 2013 Man-induced regime shifts in small estuaries - I: Theory. *Ocean Dynamics* **63**, 1279–1292.

WINTERWERP, J. C., WANG, Z.-B., VAN BRAECKEL, A., VAN HOLLAND, G. & KÖSTERS 2013 Man-induced regime shifts in small estuaries - II: A comparison of rivers. *Ocean Dynamics* **63**, 1293–1306.

WU, H., ZHU, J., CHEN, B. & CHEN, Y. 2006 Quantitative relationship of runoff and tide to saltwater spilling over from the North Branch in the Changjiang Estuary: A numerical study. *Estuarine, Coastal and Shelf Science* **69** (1-2), 125–132.

YANG, S. L., LI, M., DAI, S. B., LIU, Z., ZHANG, J. & DING, P. X. 2006 Drastic decrease in sediment supply from the Yangtze River and its challenge to coastal wetland management. *Geophysical Research Letters* **33** (L06408).

YOUNG, T. 1813 A theory of tides. *Nicholson Journal* **2**, 262–390.

ZHANG, E. F., SAVENIJE, H. H. G., CHEN, S. L. & MAO, X. H. 2012 An analytical solution for tidal propagation in the Yangtze Estuary, China. *Hydrology and Earth System Sciences* **16**, 3327–3339.

ZHANG, E. F., SAVENIJE, H. H. G., WU, H., KONG, Y. & ZHU, J. 2011 Analytical solution for salt intrusion in the Yangtze Estuary, China. *Estuarine, Coastal and Shelf Science* **91**, 492–501.

ZHONG, L., LI, M. & FOREMAN, M. G. G. 2008 Resonance and sea level variability in Chesapeake Bay. *Continental Shelf Research* **28**, 2565–2573.

ZIMMERMAN, J. T. F. 1982 On the Lorentz linearization of a quadratically damped forced oscillator. *Physics Letters* **89A** (3), 123–124.

ZIMMERMAN, J. T. F. 1992 On the Lorentz linearization of a nonlinearly damped tidal Helmholtz oscillator. *Proceedings of the Royal Dutch Academy of Science* **95** (1), 127–145.

Samenvatting

In dit proefschrift wordt de waterbeweging ten gevolge van getijden en rivierafvoer onderzocht in netwerken van kanalen. Deze zogeheten getijnetwerken zijn veelvuldig te vinden langs kustlijnen waar rivieren uitmonden in de zee; voorbeelden zijn de Rijn-Maas delta in Nederland en de Yangtze delta in China. Getijnetwerken vervullen zowel vele economische functies (zoals het transporteren van goederen en mensen) alsooco-k ecologische functies (bijvoorbeeld als broedgebied voor vogels en vissen). De mate waarin deze functies vervuld worden is aan voortdurende verandering onderhevig. Dit wordt onder andere veroorzaakt door veranderende omstandigheden ten gevolge van natuurlijke variabiliteit (bijvoorbeeld springtij-doodtij cyclus en neerslag intensiteit) en menselijk ingrijpen (bijvoorbeeld baggeren en afdammen). Er is veel maatschappelijke druk om de verschillende functies van getijnetwerken gelijktijdig te onderhouden. Hierbij rijst de uitdaging, dat veel functies conflicterende belangen hebben. Daarom is het belangrijk om de effecten van veranderende omstandigheden op het vervullen van de functies van getijnetwerken te begrijpen en te kwantificeren.

Getijnetwerken worden gekenmerkt door de overheersende rol van getijden in de waterbeweging. Vaak is er ook sprake van een rivier, die zijn water afvoert door een getijnetwerk. Op plaatsen waar een interactie tussen het zoute en zoete water plaatsvindt in een getijnetwerk spreekt men van een estuarien netwerk. Verschillende getijnetwerken hebben grote verschillen in hydrodynamische omstandigheden, zoals in getijforcering en rivierafvoer. Een variabel aspect van getijnetwerken is de aanwezigheid van wadplaten. Dit zijn gebieden die droogvallen tijdens een deel van de getijcyclus. Het oppervlak van deze gebieden verschilt sterk van netwerk tot netwerk en is aan verandering onderhevig bijvoorbeeld door inpoldering en zeespiegelstijging. Tevens is de netwerkgeometrie sterk verschillend tussen systemen, zoals de diepte en breedte van kanalen en het aantal kanalen in het netwerk. In dit proefschrift zijn twee verschillende estuariene netwerken onderzocht, te weten de Eems en de Yangtze. Deze estuariene netwerken zijn erg verschillend qua karakteristieken, maar ondervinden gelijksoortige estuariene problemen. De eigenschappen en recente ontwikkelingen van deze twee netwerken zullen kort uiteen worden gezet.

Het Eems estuarium heeft een lengte van ongeveer 100 km vanaf de eilanden op de Noordzee, tot aan de waterkering bij Herbrum (zie figuur 1.1a). De waterkering weerhoudt het getij ervan verder stroomopwaarts te verplaatsen. Er liggen grote wadplaten nabij de eilanden aan de Noordzee kant van het netwerk, tot aan de Dollard. De Dollard is een ondiep bekken (ongeveer 3 m diep) dat gescheiden is van het hoofdkanaal in de Eems rivier door middel van de Geise-Leite dam. De diepte van de hoofdgeul varieert tussen de 20 en 10 meter tot aan de Dollard. Verder stroomopwaarts is de hoeveelheid wadplaten sterk bedwongen door kanalisering van de vaargeul. De diepte wordt hier onderhouden op een bevaarbare 8 meter diepte. De breedte van het estuarium neemt af van ongeveer 8 km aan de Noordzee kant, tot ongeveer 100 m bij de sluis. Het hoofdzakelijk tweedaagse getij komt binnen vanaf de Noordzee met een typisch getijverschil van 2.3 m bij Borkum. De rivier heeft een gemiddelde afvoer van 100 m^3s^{-1} over het jaar, met fluctuaties in de orde van 50 m^3s^{-1}.
De afgelopen decennia is de vaargeul in het Eems estuarium verschillende keren verdiept om de toegang tot de verschillende havens langs het estuarium te garanderen. Dit heeft tot gevolg gehad dat het getijverschil in het estuarium is toegenomen. Dit heeft het risico op overstromingen en dijkdoorbraken vergroot, wat hoge sociaal-economische risico's met zich meebrengt. Tevens is door het toegenomen getijverschil het waterniveau van de laagste laagwaterstanden gezakt, waardoor de bevaarbaarheid van de vaargeul in het geding komt. Tot slot is de piek sediment concentratie in het estuarium toegenomen en deze bevindt zich verder landwaarts, waardoor zuurstofarme condities ontstaan die een aanslag doen op de ecologie.
Het Yangtze estuarium, welke bestaat uit de Yangtze delta (zie figuur 1.1b) en (een deel van) de Yangtze rivier, heeft een totale lengte van ongeveer 600 km vanaf de zee tot waar het getij nog meetbaar is. Hierna gaat de rivier nog wel verder, maar zonder het effect van het getij nog te ondervinden. Het estuarium is gekarakteriseerd door drie grootschalige splitsingen, waardoor het netwerk uit zeven kanalen bestaat, waarvan er vier verbonden zijn met de zee. De Yangtze delta begint bij de eerste splitsing, waar de rivier zich vertakt in de North en South Branch. De South Branch vertakt zich in de North en South Channel, waarbij de laatste zich nog een keer splitst in de North en South Passage. Wadplaten zijn wijdverspreid door de delta, maar bevinden zich vooral in de monding. De diepte van alle kanalen is rond de 10 m, met uitzondering van de North Branch, die ongeveer 5 m diep is. De totale breedte van de kanalen op de zeewaartse rand is ongeveer 80 km. Deze breedte neemt af tot ongeveer 2 km op het punt waar het getij is verdwenen. Het getij komt binnen vanaf de Oost Chinese Zee en heeft een gemengd ééndaags en tweedaags karakter, met een respectievelijke typische amplitude van 1.2 m en 2.7 m. De Yangtze rivier heeft een jaarlijks gemiddelde afvoer van 28.300 m^3s^{-1}, met piekwaarden van 40.000 m^3s^{-1} in het natte seizoen en dalwaarden van 10.000 m^3s^{-1} in het droge seizoen.

De aanwezigheid van de stad Shanghai en de bijbehorende haven hebben vele aanpassingen aan het Yangtze estuarium tot gevolg gehad. Landaanwinning vindt op veel locaties plaats, met belangrijke projecten in de North Branch en op de noordelijk daarvan gelegen Hengsha wadplaat (zie figuur 1.1b). Tussen 1998 en 2010 zijn er verregaande aanpassingen geweest aan de North Passage, welke bestonden uit het verdiepen van de vaargeul tot 12 m diepte en het aanleggen van twee parallel aan de vaargeul gelegen dijken met vele zeehoofden tot aan de gemiddelde waterdiepte. Dientengevolge zijn de getijstromingen toegenomen, waardoor de troebelheid van het water is toegenomen en vele veranderingen aan de bodem hebben plaatsgevonden (bijvoorbeeld veel afzetting van sediment in de vaargeul). Ook is de relatieve hoeveelheid zeewaarts gericht watertransport afgenomen. Dit wordt gemeten als de ratio van het zeewaarts gerichte watertransport door de North Passage en het zeewaarts gerichte transport door zowel de North als ook de South Passage. Tot slot is het Qingcaosha reservoir aangelegd in de North Channel. Dit zoetwater reservoir was beoogd om te voorzien in 50% van de vraag van de stad Shanghai. De functionering van dit bekken staat echter op het spel door sterke zoutindringing via de North Branch tot in de South Branch door te lage waterafvoer door de North Branch, als ook door zoutindringing via de wadplaten in de North Channel.
De hierboven geschetste recente ontwikkelingen en problemen in de Eems en de Yangtze zijn niet uniek voor deze estuariene netwerken. Een toename in het getijdenverschil wordt in veel netwerken waargenomen (bijvoorbeeld in de Seine, de Humber, de Rijn en de Maas). Ook komen veranderingen in het netto (getijgemiddelde) transport van water door verschillende kanalen in een getijnetwerk, zoals beschreven voor de Yangtze, voor in andere estuariene netwerken (zoals in de Berau, Mahakam en Pearl River delta). Dit is belangrijk voor de zoutindringing en het afvoeren van verontreiniging, wat weer van belang is voor de zoetwatervoorziening en de gezondheid van het ecosysteem.
Om de waargenomen veranderingen in de estuariene netwerken te begrijpen, te kwantificeren en te reduceren is het belangrijk om fundamentele kennis van de waterbeweging in deze gebieden te ontwikkelen. Het is daarom belangrijk om zowel de getijdynamica te bestuderen, als ook de dynamica van de getijgemiddelde stromen en de interactie tussen die twee. Daarom zal kort de huidige staat van kennis beschreven worden van deze onderwerpen en zal worden geïdentificeerd waar deze kennis nog aanvulling behoeft. Deze aanvullingen staan beschreven in de verschillende hoofdstukken van dit proefschrift en zullen worden samengevat.
Het getij wordt hoofdzakelijk opgewekt in getijnetwerken door coöscillatie van het water met de aangrenzende zee. In het netwerk wordt het getij vervormd ten opzichte van het getij in de aangrenzende zee. Het getij kan versterken door breedte convergentie van een kanaal en door resonantie van de getijgolf. De resonantie van het getij is afhankelijk van geometrische eigenschappen van het kanaal,

zoals diepte, lengte, de hoeveelheid wadplaten, etc. Demping van het getij treedt op door bodemwrijving en is onder meer afhankelijk van de bodemruwheid. De bodemwrijving verhoudt zich ongeveer kwadratisch tot de snelheid van het water. Verder zorgen niet-lineaire processen voor het ontstaan van boventonen van het getij.

Er is al veel onderzoek gedaan naar de waterbeweging in getijnetwerken. Belangrijk Nederlands onderzoek was het werk van Lorentz in het begin van de twintigste eeuw, waarin gekeken werd naar de gevolgen van de afsluiting van de Zuiderzee op het getij in de Nederlandse Waddenzee. Op basis van dit baanbrekende werk werd de locatie van de Afsluitdijk aangepast, om de toename in het getijverschil te beperken. Er is nog steeds behoefte aan fundamentele studies van resonantie-eigenschappen van getijnetwerken. Hierover gaan hoofdstuk 2 en 3 van dit proefschrift. In hoofdstuk 2 wordt gekeken naar de resonantie-eigenschappen van een hoofdkanaal met een secundair zijkanaal op een willekeurige positie. Hoofdstuk 3 laat vervolgens zien wat de gevolgen zijn van het zijkanaal op de stroomsnelheid van het water en het netto sediment transport.

Het netto sediment transport wordt sterk beïnvloed door de boventonen van het getij. Deze zorgen voor asymmetriën tussen de eb- en vloedstromen. Omdat grof sediment zich in contact met de bodem verplaatst, reageert dit sediment direct op veranderingen in de stroming. Hierdoor is de verhouding tussen de pieksnelheden erg belangrijk voor de richting van het netto sediment transport. Fijn sediment verplaatst zich in suspensie. Hierdoor is het voor fijn sediment veel belangrijker hoeveel tijd het sediment heeft tussen de pieksnelheden om uit te zakken. Als de overgang van piek eb naar piek vloed kort is, dan is het transport hoofdzakelijk in de vloed richting en vice versa.

Niet-lineaire processen in de waterbeweging spelen ook een belangrijke rol in het netto transport van water in getijnetwerken. Verschillende studies hebben aangetoond dat het getij de asymmetrische verdeling van de rivierafvoer bij een splitsing in een getijde netwerk zowel kan versterken als ook kan verminderen. Uit deze studies is echter niet duidelijk geworden welk niet-lineair proces welk effect heeft. Hiervoor wordt in hoofdstuk 4 een model ontwikkeld dat deze processes kan isoleren. Dit model wordt als voorbeeld toegepast op het Yangtze estuarium. Vervolgens wordt gekeken hoe deze processen variëren onder verschillende rivierafvoer en voor verschillende geometriën van het netwerk.

Tot slot zijn er veel studies geweest over het effect van wadplaten op de waterbeweging. Vele daarvan richtten zich op de tijdelijke opslag van water in deze gebieden. Hierbij wordt echter geen rekening gehouden met het gelijktijdig optredende verlies van de impuls van het water. Daarnaast fungeren veel wadplaten als tijdelijke barrières tussen twee kanalen in getijnetwerken. Hoofdstuk 5 onderzoekt welk effect deze twee eigenschappen van wadplaten hebben op de waterbeweging en het netto sediment transport.

In hoofdstuk 2 is een model gepresenteerd en bestudeerd, dat de waterbeweging ten gevolge van het dubbeldaagse maansgetij (M_2) in een netwerk van kanalen beschrijft. Het netwerk bestaat uit een hoofdkanaal en een secundair kanaal. De resultaten bieden een kwantitatief en een kwalitatief beeld van de invloed van de geometrie van een secundair kanaal op de amplitude en de fase van de getijgolf in het hoofdkanaal.
In een wrijvingsloos hoofdkanaal, veroorzaakt een kort secundaire kanaal een lager getij op het landwaartse uiteinde van het hoofdkanaal als deze tussen het einde van het hoofdkanaal ligt en de eerste knoop van het getij (de positie waar de uitwijking van het getij nul is). Voor posities tussen de knoop en de daaropvolgende zeewaartse buik van het getij (positie van maximale uitwijking) vindt een toename in amplitude plaats. Vervolgens is er weer een gebied van afname tot de volgende zeewaartse knoop, en zo verder.
Ook als het effect van bodemwrijving op het getij wordt meegenomen en als de lengte van het secundaire kanaal niet kort is, heeft de locatie en grootte van het secundaire kanaal nog een belangrijk effect op de amplitude van het getij. Echter, hoe meer de bodemwrijving wordt verhoogd in het hoofdkanaal hoe kleiner het belang van de positie van het secundaire kanaal is. Uiteindelijk treedt altijd demping van het getij op.
In hoofdstuk 3 worden de resultaten van hoofdstuk 2 verder uitgebreid, door meerdere getijdencomponenten te beschouwen, in plaats van alleen het M_2 getij. Stroomsnelheid en netto sediment transport zijn vergeleken voor netwerken bestaande uit een hoofdkanaal met en zonder secundair kanaal.
Alle getijdencomponenten worden op dezelfde wijze beïnvloed als het tweedaagse getij dat is beschreven in hoofdstuk 2. Dit toont aan dat de invloed van het secundaire kanaal plaatselijk wordt opgewekt, waarna het effect zich door het netwerk verspreidt als een modulerende (secundaire) getijde golf. De aanwezigheid van een secundair kanaal veroorzaakt slechts kleine veranderingen in de pieksnelheid van het water. Dit duidt erop dat er weinig veranderingen optreden in het netto transport van grof sediment. Veranderingen in de duur van de overgang tussen pieksnelheden zijn groter, hetgeen suggereert dat het netto transport van fijn sediment wel substantieel kan veranderen door de aanwezigheid van een secundair kanaal.
In hoofdstuk 4 zijn vier scenario's onderzocht, welke representatief zijn voor omstandigheden tijdens het natte en het droge seizoen, voor en na de aanleg van een grootschalige interventie. Bij deze interventie is de North Passage (het belangrijkste aanvoer kanaal van de haven van Shanghai) drastisch verdiept en zijn er dijken aangelegd om de vaargeul te kanaliseren. Het gemodelleerde zeeniveau is vergeleken met waarnemingen in 16 stations. Het model laat zien dat een toename in rivier afvoer een afname ten gevolg heeft van het M_2 getij door toenemende wrijving. Daarentegen neemt het viermaaldaagse getij (de eerste boventoon van

het M_2 getij) toe, door een toename in de wisselwerking tussen de rivier en het getij. Verder is aangetoond dat zowel de relatieve verdeling van rivier water, als ook het netto transport van water ten gevolge van netto getijdenstroming, slechts zwak afhankelijk is van de hoeveelheid rivier water afvoer.
Uit de vergelijking tussen de scenario's voor en na de grootschalige interventie is gebleken dat de interventie verantwoordelijk is voor een toename in de getijsnelheid en een afname in de zeeniveau variaties in een groot deel van het Yangtze Estuarium. Het netto water transport door de North Passage is afgenomen door de interventie. Dit is voor een deel te verklaren door een vernieuwde verdeling van water over de nabijgelegen tak, maar is ook te wijten aan een verminderde afvoer door het bovenstrooms gelegen South Channel als gevolg van de interventie. Hieruit blijkt dat grootschalige interventies ook een effect hebben op de hydrodynamica op verderaf gelegen locaties.
In hoofdstuk 5 zijn de twee processen onderzocht, die gerelateerd zijn aan wadplaten. Het effect van deze beide processen op de niet-lineaire snelheidskarakteristieken (vloed-eb ratio en het verschil tussen de duur van de overgang tussen de piek snelheden) en het netto transport van grof en fijn sediment is hierbij onderzocht.
Het verlies van impuls is onderzocht in een enkel kanaal met naast gelegen wadplaten. De configuratie is gebaseerd op het Amelander zeegat in de Nederlandse Waddenzee. Hierbij is het diepte profiel van de wadplaten en de hoeveelheid wadplaten gevarieerd, als ook de verdeling van de wadplaten langs het kanaal. Het diepte profiel van de wadplaten varieerde van lineair tot sterk concaaf. Twee verschillende verdelingen van wadplaten langs het kanaal zijn onderzocht. In het eerste scenario is aangenomen dat het oppervlak van de wadplaten afneemt naar rato van de landwaarts exponentieel afnemende kanaalbreedte. In het tweede scenario is de totale breedte van kanaal en wadplaten constant gehouden, waardoor aan de zeewaartse rand geen wadplaten aanwezig zijn en de oppervlakte van de wadplaten toeneemt richting het einde van het kanaal.
Impulsverlies heeft een beperkt effect op de watersnelheid en daarmee ook slechts een klein effect op het netto sediment transport. Het effect van impulsverlies op het getij neemt toe voor wadplaten met een groter oppervlak en een sterker concaaf profiel. Hierbij wordt vooral de duur tussen de pieksnelheden beïnvloed, terwijl de piek eb- en vloedsnelheden vrijwel onveranderd blijven. Dit laat zien dat het effect van impulsverlies op het netto sediment transport groter is voor fijn dan voor grof sediment.
De uitwisseling van water tussen twee kanalen is onderzocht voor een model configuratie, die gelijkenissen met de Eems vertoont. Deze configuratie bestaat uit een lang kanaal voor de Eems rivier en een kort breed kanaal voor de Dollard. De diepte van het lange kanaal is gevarieerd, als ook de hoogte van de wadplaat die de twee kanalen van elkaar scheidt. Dit laatste bepaalt daarmee de duur van de

communicatie tussen de twee kanalen.
De uitwisseling van massa en impuls door het uitwisselen van water tussen kanalen heeft een uitgesproken invloed op de getijsnelheid. Voor grotere diepten in het lange kanaal is een toename gevonden van de vloed-eb snelheid ratio. Dit heeft als gevolg dat de vloedsnelheid dominant is over de eb snelheid, waardoor het transport van grof sediment verandert van zeewaarts naar landwaarts voor toenemende diepten van het lange kanaal. De vloed-eb ratio was relatief ongevoelig voor veranderingen in de hoogte van de wadplaat. Daarmee is ook het netto transport van grof sediment ongevoelig voor veranderingen in deze hoogte. Hier staat tegenover dat de asymmetrie in duur tussen de pieksnelheden gevoeliger is voor veranderingen in de hoogte van de wadplaat dan voor veranderingen in de diepte van het lange kanaal. Voor hoger gelegen wadplaten neemt de duur van de overgang van piek eb naar piek vloed toe. Een toename in de hoogte van de wadplaat kan leiden tot een verandering in de netto transport richting van fijn sediment van landwaarts naar zeewaarts.

Dankwoord

Het voor u liggende werk mag volgens de kaft dan wel het resultaat zijn van mijn inspanningen, maar het was niet tot stand gekomen zonder de hulp van heel veel mensen. Allereerst was er een substantiële bijdrage van Huib de Swart. Als mijn enige promotor en dagelijks begeleider heb je veel werk verzet voor dit proefschrift. Je hebt mij aangestoken met je enthousiasme voor de kustoceanografie. Dit begon al tijdens mijn master toen ik je vakken volgde, waarna ik je als begeleider van mijn masterthesis vroeg. Ik was erg blij toen je mij na afloop van mijn masteronderzoek de kans gaf om verder met je te werken. Mijn eerste artikel heb ik geschreven in samenwerking met Henk Schuttelaars. Jij was een onmisbare bron voor ideeën en discussies. Daarnaast ben ik uiteraard dank verschuldigd aan mijn kamergenoten van (een deel van) de afgelopen vier jaar: Wim Ridderinkhof, Abdel Nnafie en Erik Ensing. Wim, ik vind het nog steeds heel gaaf dat je mij hebt gevraagd een bijdrage te leveren voor één van jouw artikelen. Ik vind het ontzettend leuk dat er een 'tastbare' herinnering is aan ons samenwerken. Met jou heb ik veruit het langst onze kamer gedeeld en ik ga je missen als kamergenoot. Abdel, de irreguliere werktijden die jij er op na hield waren een inspiratie voor mij om ook hard te werken. Je bent een gedreven onderzoeker en was vaak een voortrekker in het ondernemen van uitjes bij congressen en sportieve activiteiten. Erik, ik vond het geweldig om met jou de afgelopen jaren de passie voor het analytisch modelleren te mogen delen. Samen hebben we vele vergelijkingen doorgerekend en elkaars berekeningen gecontroleerd.

I would also like to thank my international colleagues at IMAU. From China: Chen Wei, Liu Bo and Yuan Bing. From Catalonia: Carles Panades. Wei, you introduced me to Chinese culture in Shanghai and you were an incredible guide on our various trips to tourist attractions in the city center. Bo and Bing, thank you so much for all the input and feedback on my work as well as the exquisite Chinese dinner parties. Carles, your experience in fundamental fluid mechanics were a great addition to the group. Being part of a Sino-Dutch research program, many thanks also extend to my Chinese counterparts. Particularly, professor Li Jiufa and professor Cheng Heqin, who accommodated me during my visits to Shanghai. Jiang Chenjuan and Yang Zhongyong accompanied me many times during my

stays and made both trips very pleasant. Apart from being great company, you also helped me acquire a lot of data for my research.
De bijeenkomsten van de estuariene leesclub waren tevens een bron van inspiratie. Hierbij kwamen drie onderzoeksgroepen uit Delft, Enschede en Utrecht bij elkaar om artikelen uit de vakliteratuur te bediscussiëren. I would like to thank all participants of the estuarine reading group as a whole, including the occasional participants, for their contributions and clarifications on questions that arose while reading articles. In het bijzonder wil ik Pieter Roos en Ronald Brouwer bedanken. Gezellige gesprekken en diepgaande discussies waren aan jullie altijd wel besteed.
To all people at IMAU: Thank you for providing such a nice atmosphere to work in. The coffee breaks were an ideal opportunity to catch a break from work and have a nice chat about other subjects. The regular work-outs also provided a nice change of pace with regular running and the Christmas IMAU badminton tournament.
Ook familie en vrienden ben ik dank verschuldigd voor het bieden van morele ondersteuning en het proeflezen van delen van dit proefschrift. Allereerst wil ik mijn ouders bedanken. Jullie hebben van mij een doorzetter gemaakt en mij altijd gestimuleerd om het beste uit mezelf te halen. Bedankt dat jullie me hebben aangemoedigd om deze stap te nemen. Tim, je bent bij tijd en wijle weliswaar moeilijk bereikbaar, maar omdat jij ook aan het promoveren bent, zitten we toch in het zelfde schuitje. Ik kan bij jou altijd terecht voor een luisterend oor. Lianne en Ralph, de avondjes en weekenden spelletjes spelen met jullie, hebben geholpen om de broodnodige ontspanning te krijgen in hectische perioden. We konden altijd bij jullie terecht als er iets aan de hand was. Lauren, we met while you were visiting Utrecht for research, and I'm very happy to have stayed in touch afterwards. My holidays to Gainesville are still personal highlights of my time as a PhD.
Traditiegetrouw sluit ik dit dankwoord af met het bedanken van diegenen die mij het meest dierbaar zijn. Lieve Imke, jouw geboorte halverwege mijn promotietraject heeft het proces misschien niet makkelijker gemaakt, maar ons leven zo veel rijker. Lieve Veerle, voor jou heb ik mijn verdediging nog even moeten uitstellen, maar hierdoor sta je wel nog precies in dit boekje. Wat was het genieten om je na een dag hard werken te zien trappelen in mama's buik. En als laatste, Eliane. Aan jou heb ik de afgelopen vier jaar de meeste steun gehad. Ook al had je het zelf niet altijd even makkelijk met de drukte die gepaard ging met mijn promotieonderzoek, je hebt mij alle ruimte gegeven om mijn werk te doen. Jij hebt me door laten zetten op de momenten dat ik het het moeilijkst had en me gebracht waar ik nu ben. Duizendmaal duizendmaal duizendmaal dank. Miljard.

Curriculum Vitae

I was born on May 15, 1988 in Delfzijl next to the Ems estuary. I graduated from the Oranje Nassau College (secondary school) in Zoetermeer in 2006, with a passion for science. At Utrecht University, I obtained a bachelor degree in both Physics and Mathematics. In these years, I developed my enthusiasm for modelling the atmosphere and ocean. I wrote my bachelor thesis on 'The influence of sulphuric acid and ammonia on the aerosol optical thickness' under supervision of dr. Geert-Jan Roelofs. I obtained a master degree in Meteorology, Physical Oceanography and Climate. My masterthesis, written under the supervision of prof. dr. Huib de Swart and prof. dr. Sjef Zimmerman, was on 'Non-linear tides in wadden systems: modelling the effect of mass and momentum transfer between channels and flats'. During the process of writing my master thesis, I was offered the PhD position by prof. de Swart of which this dissertation is the result. This made for a nice circle, since it involved working on the Ems estuary.